MODELING AND BENCHMARKING OF SPINTRONIC DEVICES AND THEIR APPLICATIONS

A Dissertation
Presented to
The Academic Faculty

by

Yu-Ching Liao

In Partial Fulfillment
of the Requirements for the Degree
Doctor of Philosophy in the
School of Electrical and Computer Engineering

Georgia Institute of Technology
August 2021

MODELING AND BENCHMARKING OF SPINTRONIC DEVICES AND THEIR APPLICATIONS

Approved by:

Dr. Azad Naeemi, Advisor
School of Electrical and Computer Engineering
Georgia Institute of Technology

Dr. Asif Khan
School of Electrical and Computer Engineering
Georgia Institute of Technology

Dr. Shimeng Yu
School of Electrical and Computer Engineering
Georgia Institute of Technology

Dr. Dmitri E Nikonov
School of Electrical and Computer Engineering
Purdue University

Dr. Jeffrey A Davis
School of Electrical and Computer Engineering
Georgia Institute of Technology

Date Approved: June 24, 2021

ACKNOWLEDGEMENTS

I would like to thank my advisor Prof. Azad Naeemi for all the guidance and discussions during the research. Prof. Naeemi not only gave me a great degree of freedom to explore interesting research topics but also provided me with opportunities to attend workshops and conferences. I am also thankful for all the team members in our lab including Prof. Chenyun Pan, Dr. Sou-Chi Chang, Dr. Sourav Dutta, Dr. Divya Prasad, Dr. Rouhollah Mousavi, Dr. Ramy Nashed, Dr. Nickvash Kani, Victor Huang, Chia-Sheng Hsu, Mufutau Akuruyejo, Samantha Lubaba Noor, and Piyush Kumar for the fruitful discussions with them. Next, I would like to thank Dr. Ian Young and Dr. Dmitri Nikonov from the Intel's Components Research Lab for all the discussions and their support of my project. Last, I would like to thank all of my family members including my mother Fan-Jung Lin, my elder sister Szu-Min Liao, and my twin sister Yu-Chiao Liao. Thanks for their support I had the opportunity to study in the U.S. and explore the interesting research area of nanoelectronics and condensed matter physics. I also want to thank my boyfriend Chin-Sheng Pang for his continuous encouragement and for being the best partner for both learning and for life. Thanks for all the people I met in my PhD life that made my study interesting and meaningful.

TABLE OF CONTENTS

LIST OF TABLES

LIST OF FIGURES

SUMMARY

In this work, we have explored various spintronic devices based on various magnet write mechanisms such as spin-transfer torque (STT), spin-orbit torque (SOT), magnetoelectric (ME) effect, and voltage-controlled exchange coupling (VCEC), and have benchmarked their array-level performance in the embedded memory applications. In the first part, our goal is to model the transient response or the switching dynamics of a specific magnetoelectric device: $BiFeO_3$/CoFe heterojunction to benchmark its array-level performance. Bismuth ferrite (BFO) is a multiferroic material with prominent ferroelectricity, antiferromagnetism, and weak ferromagnetism at room temperature. By combining BFO with a ferromagnet such as CoFe and forming a BFO/CoFe heterojunction, one can manipulate the magnetic state of CoFe layer by applying an external electric field which is expected to be more energy efficient compared to other current controlled switching mechanisms. We have constructed the physical model of BFO using coupled ferroelectric and micromagnetic models for the first time. Next, the BFO/CoFe heterojunction is modeled using micromagnetic simulations for the coupled BFO and CoFe layers. The interface exchange coupling between BFO and CoFe layers is a major parameter that we extracted from the experimental results. The magnetization switching behavior of the CoFe layer with various energy barriers have also been studied to evaluate the thermal stability and switching success rate. To achieve both, we found that we should choose a BFO/CoFe heterostructure with a high length to width aspect ratio (>5) and use a CoFe layer as thin as 1nm. A thinner CoFe layer ensures a better controllability of the interface exchange coupling effect, and a high aspect ratio device maintains the thermal

stability of the BFO/CoFe heterojunction. Moreover, to evaluate the circuit level performances of the magnetoelectric (ME) magnetorestrictive random-access memory (MRAM), we have built the compact model based on the physical model we set up for the BFO/CoFe heterojunction. The results from our compact model closely match to those from the micromagnetic models when simulating the magnetization dynamics of BFO and CoFe. Using the compact model we developed, the SPICE simulation shows that ME-MRAM can potentially operate with a lower write energy compared to the spin-transfer torque MRAM (STT-MRAM), spin-orbit torque MRAM (SOT-MRAM) or even SRAM when the coercive voltage of the BFO layer is as small as 20mV. In the second part, we have explored various material options for the SOT-MRAM including heavy metals, Semi-metals, alloys, and topological insulators. We build a comprehensive modeling framework for the SOT-MRAM by including some non-ideal factors such as the current shunting effect, current crowding effect, variation of process parameters, and joule heating effect. Our results show that topological insulators such as Bi_xSe_{1-x} with high charge to spin conversion efficiencies are more promising than other materials. Last, we benchmark the array-level performance of various spintronic memory devices such as STT-MRAM, SOT-MRAM, voltage-controlled exchange-coupled MRAM (VCEC-MRAM), and ME-MRAM. Our results show that ME-MRAM is the most promising in terms of write energy and write latency compared to other candidates.

INTRODUCTION

The semiconductor industry has been rapidly advancing in the past 50 years, thanks to the relentless research and process improvements that has enabled denser and faster transistors being fabricated for electronic products. Some revolutionary advances in recent years include the EUV technology that is critical for photolithography in ultra-scaled dimensions, multi-gate structures to improve the electrostatic control in transistors and mitigate short-channel effects, the 3D stacking of the multi-bit NAND cell to realize ever increasing array densities, and the high bandwidth memory (HBM) that largely increases the bandwidth and the array efficiency of the DRAM. Moreover, the recent advances in the area of the artificial intelligence in autonomous vehicles, the medical diagnosis, and image recognition open many opportunities and new markets for the electronics industry. However, the semiconductor industry also faces many challenges these years. First, conventional MOSFET operates based on thermionic emission of carriers and requires ~0.4V supply voltage to maintain an on-off ratio of six orders of magnitude. Hence, to avoid ever increasing static power dissipation, supply voltage cannot be scaled as prescribed by Dennard's scaling law. Therefore, researchers are seeking alternatives to CMOS devices to break the limit of 60 mV/decade subthreshold swing set by the Boltzmann limit [1], [2]. Second, the mismatch between the computing power of microprocessors and the bandwidth of memory modules has been growing over the years and has reached unsustainable levels in recent years [2]. Increasing the memory read/write speed while keeping power dissipation low is critical. In addition, the endurance, reliability, and the scalability of the memory devices are equally important for obvious

commercial reasons. Currently, there are many emerging non-volatile memory device options are being explored [3] including phase change random-access memory (PCRAM), resistive random-access memory (RRAM), and magnetic random-access memory (MRAM)), with their pros and cons depending on different application fields. Third, as scaling of two-dimensional geometry becomes challenging, the monolithic 3D heterogeneous integration of logic, memory, and other capabilities opens a new path to improve the overall system performances. Thus, the process compatibility with the Si technology and the thermal budget becomes crucial for the 3D heterogeneous integration. These challenges entice researchers to explore new devices or materials to overcome these limits.

Spintronic devices that utilize the spin of the electron or the magnetic moment of the material to store and transfer information are inherently non-volatile thus are promising for low power applications such as beyond-CMOS devices [4], non-volatile memory [5], in-memory computing [6] and neuromorphic computing [7]. The traditional CMOS technology uses charge as the computational state variable; therefore, to maintain a high on/off ratio, the minimum supply voltage is typically larger than 0.5V [8] which is not scalable with technology scaling. Moreover, the switching energy of MOSFET requires many time kT (~4000kT= $N_e \cdot 20kT$) since it is proportional to the number of electrons (N_e) involved during switching. Compared to the CMOS technology, spintronic devices using the spin as a computation variable could achieve a smaller switching energy limit (~60kT) since the switching energy is directly determined by the energy barrier of the magnet. Also, since there are no leakage currents related to the energy barrier of the spintronic devices, the write current scales as the size of magnets scales. In terms of memory application,

spintronic memory devices usually have characteristics of near infinite endurance, fast switching speed, non-volatility, and scalability which makes them competitive for applications such as the last levels of cache, embedded memory, and image buffers. Last, the low fabrication process temperature (<400°C) and the low write energy of the spin-transfer torque magnetorestrictive random-access memory (STT-MRAM) are beneficial for the 3D heterogeneous integration since it is backend compatible with the Si technology and with a low thermal budget.

The realization of the spintronic devices got accelerated by the discovery of the giant magnetoresistance [9][10] (GMR) effect and tunneling magnetoresistance [11][12] (TMR) effect since they made it easier to electrically read the information inside the ferromagnet by the change of the resistance state. Giant magnetoresistance exists when a paramagnetic or metallic layer is sandwiched by two ferromagnets and forms a spin-valve structure. The resistance of the spin-valve depends on the orientations of the two ferromagnetic layers since the electron scattering at the interface between the non-ferromagnetic and ferromagnetic layers varies. Compared to the GMR, the TMR happens when two ferromagnetic layers separated by a dielectric layer form a magnetic tunnel junction (MTJ). The resistance of the MTJ also depends on the orientation of the two ferromagnetic layers because of the spin-dependent electron tunneling. Besides, the discovery of the spin-transfer torque [13][14][15][16] and spin-orbit torque [17][18][19][20][21] made the writing of magnetic states more energy efficient compared to the traditional magnetorestrictive random-access memory (MRAM) which used the current-induced magnetic field. Nevertheless, spin-transfer torque MRAM (STT-MRAM) and spin-orbit torque MRAM (SOT-MRAM) are still current-controlled devices and thus dissipate a

significant amount of energy in the form of Joule heating. In addition to the attempts aimed at improving the charge-to-spin conversion efficiency of STT or SOT, researchers are also looking for other physical mechanisms such as voltage-controlled magnetic anisotropy [22] (VCMA) effect, voltage-controlled exchange coupling (VCEC) effect [23], and magnetoelectric [24][25][26] (ME) effect. The main difference between these new mechanisms and STT or SOT is that they are electric field-driven. According to the previous benchmarking results [27][28][29] of beyond-CMOS devices, voltage-controlled devices can potentially dissipate far lower energy compared to the current-controlled devices because of the drastic reduction in Joule heating. Hence, in this work, we will consider modeling and design of both current-controlled and voltage-controlled devices. In Chapter 2, a holistic modeling and benchmarking approach for all magnetic memory devices is presented. In this introductory study, the main physical models for various write operations are presented and the interdependencies between read and write operations are studied. In the following chapters, more detailed and accurate models for each major category of devices are presented and used to design and benchmark them. In Chapter 3, rigorous physical models are presented for magnetoelectric (ME) devices and important material parameters are extracted from experiments. Next, to evaluate the circuit level performances of the ME devices in the memory application, Chapter 4 presents a compact model for the ME device which is useful for circuit simulations of the ME-MRAM. In Chapter 5 we discuss the modeling and the simulation of SOT-MRAM using various SOT materials. Last, in Chapter 6, the challenges and opportunities for future research are discussed.

Before modeling and analyzing various memory devices in the following chapters, in the following sections, the main physical phenomena and concepts used in these devices are briefly reviewed.

1.1 Magnetic materials

1.1.1 Magnetic energy in ferromagnetic materials

The total magnetic energy density of a ferromagnet with normalized magnetization $\boldsymbol{m}$ can be written as:

$$E = A_{ex}(\vec{\nabla}\boldsymbol{m})^2 - K_u(\boldsymbol{m}\cdot\vec{\boldsymbol{u}})^2 - \mu_0 M_s \boldsymbol{H_{ext}} - \frac{1}{2}\mu_0 M_s(\boldsymbol{H_{dem}}\cdot\boldsymbol{m}) \quad (1)$$

which includes the exchange energy, magnetic crystalline anisotropy energy, magnetic energy associated with the external magnetic field, and magnetostatic energy (or demagnetization energy or shape anisotropy energy), respectively. The exchange energy comes from the cell to cell interaction that keeps the magnetization of the neighboring cells aligned to the same direction, thus it is a short-range field. The magnitude of the exchange energy depends on the exchange stiffness constant A_{ex}. The magnetic crystalline anisotropy energy originates from the crystalline structure of the lattice with a preferred easy-axis, easy-plane, or a cubic structure. When the anisotropy constant K_u is positive, spins will align parallel or antiparallel to the easy-axis: $\vec{\boldsymbol{u}}$; but when K_u is negative, spins will prefer to be perpendicular to the hard-axis: $\vec{\boldsymbol{u}}$, i.e. the easy-plane state. The magnetic anisotropy energy may compose of the epitaxial strain, the growth anisotropy that comes during the fabrication process, and the surface anisotropy at the interface. In addition, there may be magnetostriction terms which come from the coupling between strain and the

magnetism in the piezomagnetic material. Next, the external applied magnetic field $\boldsymbol{H_{ext}}$ causes the asymmetric Zeeman energy. Last, the magnetostatic energy is a shape-dependent energy which is analogous to the electrostatic energy in a capacitor. The magnetostatic energy comes from the internal magnetization at different points of the cells which is lowered when the magnetic dipolar field is minimized, therefore, it is a long-range interaction.

1.1.2 The micromagnetic model

The modeling of the magnetism in the ferromagnets range from the atomic scale, micrometer scale to macro-spin scale depending on the required accuracy and the available computation resources and time. The atomic scale simulations that incorporate the quantum-mechanical *ab*-initio calculations using the density functional theory can model the atomistic interaction of magnetic atoms theoretically; however, the calculations are idealized and important features such as the defects, finite temperatures, and real magnetization dynamics may not be captured. In addition, the computation time of the atomic scale calculations drastically increases as the size of the material increases; therefore, micromagnetic simulations which can model the magnetization dynamics of the ferromagnet as the mesoscale fast and accurately are commonly used. The micromagnetic simulation divides a ferromagnet into multiple cells with a given mesh size and consider the long- and short- range interaction within cells. Normally, the maximum mesh size is determined by the exchange length $\lambda_{ex} = \sqrt{A_{ex}/K_u}$. If the magnetization reverses over the exchange length, then the mesh size needs to be within $0.25\lambda_{ex}$. The dynamics of the magnetization in each cell is described by the Landau–Lifshitz–Gilbert (LLG) equation:

$$\dot{\boldsymbol{M}}_i = -\gamma(\boldsymbol{M}_i \times \boldsymbol{H}_i) + \frac{\alpha_G}{M_s}\left(\boldsymbol{M}_i \times \dot{\boldsymbol{M}}_i\right) \quad (2)$$

where $\boldsymbol{M}_i$ is the magnetization in the cell i, γ is the gyromagnetic ratio, $\boldsymbol{H}_i$ is the effective local magnetic field in the cell i, M_s is the saturation magnetization, and α_G is the Gilbert damping factor. The effective local magnetic field can be calculated as the derivative of the total magnetic energy with respect to the magnetization $\boldsymbol{M}_i$. The contribution of the exchange energy, anisotropy energy, and the demagnetization energy can be expressed as $\boldsymbol{H}_i = \frac{2A_{ex}}{\mu_0 M_S^2}\nabla^2\boldsymbol{M}_i + \frac{2K_u}{\mu_0 M_S^2}(\boldsymbol{M}_i \cdot \vec{\boldsymbol{u}})\vec{\boldsymbol{u}} + \frac{\mathbf{1}}{\mathbf{4}\boldsymbol{\pi}}\int d^3r' \frac{\mathbf{3}(\boldsymbol{M}_i(r')\cdot\mathbf{x})\mathbf{x} - \boldsymbol{M}_i(r')|\mathbf{x}|^{\mathbf{2}}}{|\mathbf{x}|^{\mathbf{5}}}$, respectively. Here $\boldsymbol{x} = r - r'$ and r' can be in the *x*, *y*, and *z* directions. For the details of the micromagnetic simulations one can refer to [30].

1.1.2.1 Temperature dependency and the thermal noise effect

The magnetism of the material has the temperature dependency since the thermal energy may randomize the magnetic order as temperature increases. For a ferromagnetic material, if the temperature is higher than the Curie temperature (T_C), then the magnetic order disappears and the ferromagnet becomes paramagnetic. Similarly, for an antiferromagnetic material, if the temperature is higher than the Neel temperature (T_N), the antiferromagnet also becomes paramagnetic. If the temperature is below both T_C and T_N but the thermal energy is comparable to or higher than the energy barrier of the ferromagnet, the magnetic order of the ferromagnetic or antiferromagnetic materials may be randomized and unstable. In other cases, the temperature of the magnetic materials would have time dependency since the applied charge current induced joule heating effect as discussed in [31]. Therefore, the temperature dependency of the magnetic materials and the thermal

noise effect are critical for the magnetic properties and the stability of the spintronic devices.

To incorporate the thermal noise effect of the magnetic material when the temperature is below T_C and T_N, the thermal field in the ferromagnet can be modeled as $\boldsymbol{H_T}(t)dt = \nu d\boldsymbol{W}(\boldsymbol{t})$ where $\nu = \sqrt{\frac{2\alpha K_b T}{\mu_0 M_s^2 V}}$ and $\boldsymbol{W}(\boldsymbol{t})$ is the Wiener process. The thermal field follows the Gaussian distribution, and the statistical properties of the thermal field as discussed by Brown [32] and Kubo [33] are given as

$$\langle H_{T,i}(t)\rangle = 0$$
$$\langle H_{T,i}(t), H_{T,i}(t+\tau)\rangle = \frac{2K_b T\alpha}{\gamma\mu_0^2 M_s V}\delta_{ij}\delta(\tau) \tag{3}$$

where τ is the time interval, T is the temperature, γ is the gyromagnetic ratio of the electrons, K_b is the Boltzmann constant, and δ_{ij} is the Kronecker delta function.

To numerically simulate the thermal field, we can discretize the thermal field as $\boldsymbol{H_T}(t)\Delta t = \nu\Delta\boldsymbol{W}(\boldsymbol{t})$ where $\Delta\boldsymbol{W}(t) = \boldsymbol{W}(t+\Delta t) - \boldsymbol{W}(t)$ and Δt is the time step used in the numerical simulations. The standard deviation of the thermal field is $\sigma = \sqrt{\frac{2K_b T\alpha\Delta t}{\gamma\mu_0^2 M_s V}}$ and $\Delta\boldsymbol{W}(t) \sim N(0,1)$ which is a standard Gaussian vector. Note that the convergence of the stochastic-LLG equation depends on the time step we choose. Normally, a smaller time step ~10 fs is used in the micromagnetic simulation for a better convergence in the numerical simulation. Alternatively, one can adopt the implicit midpoint method as discussed in [34].

1.2 Magnetoresistance

As discussed earlier, the renaissance of the spintronics comes after the discovery of the GMR and the TMR effect since the discovery of the magnetoresistance provides an electrical way to read-out the information of the magnetic materials. In contrast to the anisotropic magnetoresistance (AMR), the value of GMR and TMR ratio are much larger (~100%) thus they are commonly used for the read operation in the MRAM technology. The physical origins of the GMR and TMR are discussed in the following sections.

1.2.1 Giant magnetoresistance

The giant magnetoresistance (GMR) effect refers to the change of the resistance value when the relative orientations of the magnetization in ferromagnetic layers of the spin valve changes. The spin valve structure is composed of two ferromagnetic layers sandwiched by a non-magnetic layer, which is usually metallic. When the current flows through the spin-valve structure in the in-plane (CIP) or the perpendicular (CPP) plane directions, the difference in the scattering rates of electrons in majority or minority bands causes high or low resistance states. The majority spins have higher conductivity than the minority spins. Hence, if the magnetization of the two ferromagnetic layers are parallel, the resistance is low since the scattering rate is low because the currents flowing through both ferromagnetic layers are majority spins, which can be viewed as two low resistances state in series. Similarly, if the magnetization of the two ferromagnetic layers are antiparallel, the resistance is high since it can be viewed as a low resistance in series with a high resistance. The GMR ratio is then defined as

$$GMR = \frac{R_{AP} - R_P}{R_P} \tag{4}$$

where R_{AP} and R_P are the resistances when the two ferromagnetic layers are antiparallel or parallel, respectively.

1.2.2 Tunneling magnetoresistance

The tunneling magnetoresistance (TMR) effect happens in the magnetic tunnel junction (MTJ) in which an insulating layer is sandwiched by two ferromagnetic layers. TMR occurs because of the differences in the tunneling rates of electrons in the majority and minority bands. The majority spins have higher density of states (DOS), while minority spins have lower DOS. When the magnetizations of the two ferromagnetic layers are in parallel, the spin-up states (majority spins with high DOS in the first ferromagnetic layer) have higher probability to tunnel to the spin-up state in the second ferromagnetic layer, (also a majority band with high DOS) as shown in **Figure 1**. Therefore, the resistance is low when the magnetization states in the MTJ is parallel. But if the magnetizations of the two ferromagnetic layers are antiparallel, the resistance is high. This is because the spin-up state, which is majority spin with high DOS in the first ferromagnetic layer, has a lower probability to tunnel to the spin-up state, which is minority spin with low DOS in the second ferromagnetic layer. The TMR ratio is then defined as

$$TMR = \frac{R_{AP} - R_P}{R_P} = \frac{G_P - G_{AP}}{G_{AP}} \tag{5}$$

where R_{AP} (R_P) is the resistance of the MTJ when the magnetizations of the two ferromagnetic layers are antiparallel (parallel). Since the TMR is a tunneling effect, the TMR ratio and the resistance area (RA) product of the MTJ are highly dependent on the thickness of the insulator (oxide). The RA product increases exponentially with the oxide thickness of the MTJ, and the TMR ratio would saturate at thicker oxide thickness as shown in [35].

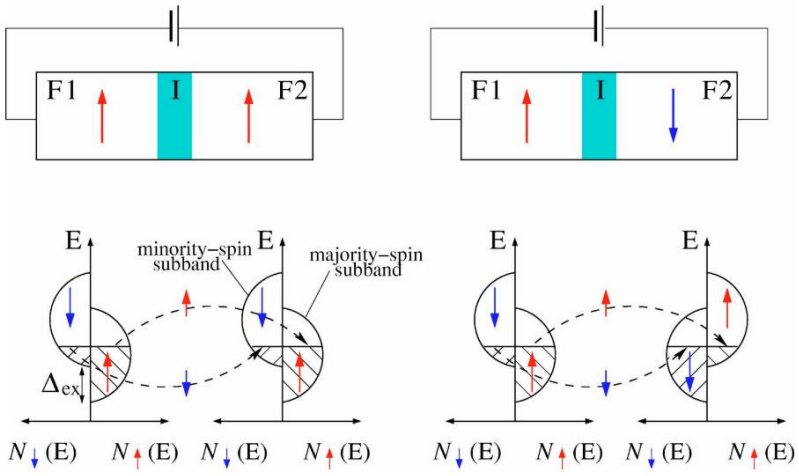

Figure 1 – Schematics of the electrons tunneling in the ferromagnet/insulator/ferromagnet when the two ferromagnetic layers are (a) parallel or (b) anti-parallel. [36] Reprinted from "Spintronics: Fundamentals and applications", Igor Žutić, Jaroslav Fabian, and S. Das Sarma, Rev. Mod. Phys., vol. 76, no. 2, pp. 323–410, Apr. 2004. Copyright 2004 American Physical Society.

1.2.2.1.1 Design of the magnetic tunnel junction (MTJ)

The magnetization of the two ferromagnetic layers in the MTJ can be in the in-plane (i-MTJ) or in the perpendicular (p-MTJ) direction. For high density spintronic devices, p-MTJ is preferred since the area density is higher. In addition, for p-MTJ, both

the thermal barrier and the critical current of magnet switching are governed by the perpendicular anisotropy energy. Whereas for i-MTJ, the thermal barrier is governed by the demagnetization energy but the critical current of magnet switching is determined by the in-plane anisotropy energy. Therefore, p-MTJ is commonly used for advanced STT-MRAM. Normally, CoFe or CoFeB are used for the free layer of the i-MTJ; however, using the double CoFeB/MgO interface or inserting layers of heavy metals such as Ta, Mo, or W can enhance the interfacial anisotropy of the free layer FM thus the magnetic anisotropy of the free layer ferromagnet changes from in-plane to out-of-plane direction [37].

1.3 Write mechanisms of spintronic-based devices

1.3.1 Overview of the current-controlled and voltage-controlled magnetization switching

To manipulate the magnetization state of the spintronic device, there are various physical mechanisms that are under explored. Currently, there are current-controlled mechanisms such as current-induced magnetic field, spin-transfer torque (STT), and spin-orbit-torque (SOT). Also, there are voltage-controlled mechanisms such as voltage-controlled exchange coupling (VCEC), and the magnetoelectric effect (ME). Generally, voltage-controlled mechanisms can provide lower power than the current-controlled mechanisms due to the elimination of the joule heating energy. In the following sections, we would overview the physics of each physical mechanisms.

1.3.1.1 Spin-transfer torque (STT)

Spin-transfer torque (STT) can be exerted on the ferromagnetic layer when the flow of spin-angular momentum through a sample is not a constant. When electrons inject into

a non-magnetic and ferromagnetic layer (FM) bilayer, electrons with a randomized magnetic moment will have finite probability to transmit through the FM or reflect at the interface. If the magnetic moment of the electron is parallel to the FM, electrons are transmitted to the FM due to the spin filtering effect. The filtered charge current creates spin current. If the magnetic moment of the electrons is antiparallel to the FM, the reflection happens for electrons. Now if the current flowing through a MTJ as shown in **Figure 2**, there are spin momentum transfers between electrons filtered in the pinned layer FM and the electrons in the free layer FM. If the spin current generated by the pinned layer FM is not colinear with the free layer FM, spin-transfer torque (STT) arises, and the STT would then flip the magnetization of the free layer FM such that the magnetization of the pinned layer FM and free layer FM become parallel. Similarly, if a current is applied in the opposite direction, the reflected electrons at the interface of the pinned layer FM would also exerts a STT on the free layer FM and flip the magnetization state from spin-up to spin-down. Therefore, by controlling the direction of current flowing through the MTJ, one can switch the magnetization of the free layer FM.

To numerically simulate the STT effect, the LLG equation can be expressed as

$$\frac{\partial \boldsymbol{M}}{\partial t} = -\gamma\mu_0\left(\boldsymbol{M}\times\boldsymbol{H}_{eff}\right) + \frac{\alpha_G}{M_s}\left(\boldsymbol{M}\times\frac{\partial \boldsymbol{M}}{\partial t}\right) - \frac{\boldsymbol{M}\times(\boldsymbol{M}\times\boldsymbol{I}_s)}{qN_sM_s} - \beta\frac{\boldsymbol{M}\times\boldsymbol{I}_s}{qN_s} \qquad (6)$$

where the third term refers to the anti-damping-like torque due to spin-transfer torque and the fourth term refers to the field-like torque. Here, $\boldsymbol{I}_s$ is the magnitude of the applied spin current, β is the field-like torque factor, and $N_s = \frac{2M_sV}{\gamma\hbar}$ is the number of spins. As the magnitude of $\boldsymbol{I}_s$ increases, the magnitude of the STT increases. Therefore, the STT can be

used to switch the magnetization of the free layer ferromagnet by applying charge current that is higher than the critical current of magnet switching (I_C). When the applied current is smaller than I_C, magnetization precession happens but the anti-damping-like torque will drag the magnetization to the initial position and no switching happens as shown in **Figure 3**(b). If the applied current is higher than I_C, then the precession angles become large when time increase as shown in **Figure 3**(c), eventually the magnetization switching happens as shown in **Figure 3**(d). In the monodomain mode, the critical current of magnet switching (I_c) of an in-plane ferromagnet can be calculated as [38], [39]

$$I_c = \frac{2e}{\hbar}\frac{\alpha}{\eta(0)}V\mu_0 M_s(H + H_k + \frac{M_s}{2}) \tag{7}$$

where α is the Gilbert damping coefficient, H is the applied magnetic field, H_k is the strength of the in-plane magnetic anisotropy, M_s is the saturation magnetization, V is the volume of the ferromagnet, and $\eta(\theta) = q/(A + Bcos\theta)$. Here q, A and B are constants that depends on the structure of the FM. Note that for an in-plane ferromagnet, the critical current in eq. (7) is dominated by the shape anisotropy field $\frac{M_s}{2}$, however, this field would not contribute to the thermal stability of the ferromagnet which is proportional to H_k. To lower the critical current of magnet switching in the in-plane ferromagnet, one can add materials with the perpendicular magnetic anisotropy (PMA) at the interface. If the perpendicular magnetic anisotropy energy ($H_{k,\perp}$) of the ferromagnet is smaller than M_s, then the magnetization of the ferromagnet is still in the in-plane direction, but the last term in eq. (7) is replaced by $H + H_k + \frac{M_s}{2} - \frac{H_{k,\perp}}{2}$. If the PMA energy ($H_{k,\perp}$) of the ferromagnet

is larger than M_s, then the magnetization of the ferromagnet will be in the out-of-plane direction, and the critical current of magnet switching is expressed as [40], [41]

$$I_c = \frac{2e}{\hbar}\frac{\alpha}{\eta(0)}V\mu_0 M_s(H + H_{k,\perp} + H_{dip} - M_s) \approx \frac{2e}{\hbar}\frac{2\alpha}{\eta(0)}U_k \text{ when } H = H_{dip} = 0 \quad (8)$$

where H_{dip} is the dipolar field from the reference layer ferromagnet, M_s in the last term of eq. (8) is the demagnetization field arises from the thin film geometry, $U_k = \mu_0 M_s V(H_{k,\perp} - M_s)/2$ is the height of the energy barrier between the two stable magnetization states. To lower the critical current of the PMA-FM, one can lower the magnitude of $H_{k,\perp}$ by tuning the anisotropy of the materials but keeping $H_{k,\perp}$>M_s.

Currently, spin-transfer torque has been utilized or studied for various applications such as the last level of cache, image buffer, microwave oscillators, memristor, wave emitters, and microwave detectors [42]. For example, STT-MRAMd is considered more promising than the conventional MRAM which uses current-induced magnetic fields for magnet switching due to the lower write current and the scalability of the MTJ.

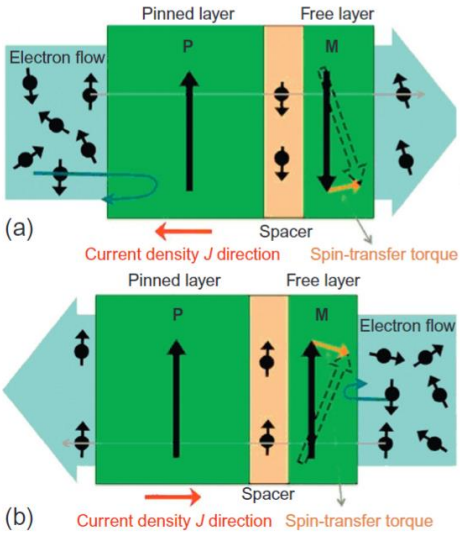

Figure 2 – Schematics of the spin-transfer torque in the magnetic tunnel junction [43]. Reprinted from "Chapter 7 - Spintronic Oscillators Based on Spin-Transfer Torque and Spin-Orbit Torque," R. E. Camley, Z. Celinski, and R. L. Stamps, Eds. North-Holland, Handbook of Surface Science, vol. 5, , 2015, pp. 297–334. Copyright 2015 Elsevier.

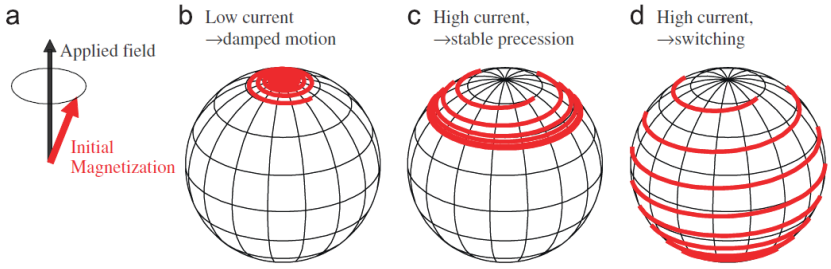

Figure 3 – Trajectories of the magnetization vector driven by the spin-transfer torque [38]. (a) Schematics showing the vectors of the initial magnetization and the applied field. The trajectories of the magnetization when (b) the applied current is below the critical current or (c) above the critical current and (d) the magnetization switching

happens. Reprinted from "Spin transfer torques," D. C. Ralph and M. D. Stiles, J. Magn. Magn. Mater., vol. 320, no. 7, pp. 1190–1216, Apr. 2008. Copyright 2008 Elsevier.

1.3.1.2 Spin-orbit torque

Spin-orbit torque (SOT) comes from the coupling between spin angular momentum and orbital angular momentum of electrons at the ferromagnet/non-ferromagnet interface. Different from the STT, the spin orbit coupling causes electrons moved by the electric field to experience a magnetic field that couples to the magnetic moment of the electrons. For example, when the charge current flows from -*x* to +*x*, this charge current will generate spin current in the perpendicular direction(*z*). The spin current with different spin polarity (+/- *y*) will flow to the opposite direction because the SO coupling bends the trajectory of electrons with a different spin state. SOT includes bulk spin Hall effect and the interface Rashba-Edelstein effect as described in the following two subsections.

1.3.1.2.1 Spin Hall effect

The bulk spin Hall effect (SHE) arises due to the distortion of the energy bands from spin orbit coupling (intrinsic) or the Mott scattering that comes from the extrinsic impurities. Both intrinsic and extrinsic SHE would lead to the spin-dependent asymmetric scattering of the conduction electrons. The asymmetric scattering causes the deflection of spin-up and spin-down electrons in the opposite directions which is transverse to the charge current. The spin current generated by the SHE can be expressed as

$$\boldsymbol{J_s} = \frac{\hbar}{2e}\theta_{SH}(\boldsymbol{J_c} \times \boldsymbol{\sigma}), \tag{9}$$

where $\boldsymbol{J_s}$ is the spin current generated from the SHE, $\boldsymbol{J_c}$ is the charge current flowing through the SOT material, θ_{SH} is the spin Hall angle which determines the efficiency of charge to spin current conversion, and $\boldsymbol{\sigma}$ is the polarization of the accumulated spins. While SHE generates spin current from the charge current flowing through the SOT material, there is also a reverse effect called inverse spin Hall effect (ISHE) which generates charge current from the spin current. It is suggested that ISHE may be a possible way for the read operation of the spintronic devices such as MESO [44]. Currently, there are various materials that have been explored such as heavy metals, semi-metals, topological insulators which show different values of θ_{SH} and conductivity. The exploration of the performance of SOT-MRAM using various SOT materials are discussed in Chapter 5.

1.3.1.2.2 Interface Rashba-Edelstein Effect

The interface Rashba-Edelstein effect (inverse spin galvanic effect) arises when there is broken inversion symmetry in the system such as the non-ferromagnet/ferromagnet interface and the two-dimensional electron gases (2DEGs). The spin-orbit coupling at the interface generates an internal electric field $\boldsymbol{E}$, and the electrons with momentum $\boldsymbol{p}$ would experience an effective magnetic field. The Hamiltonian of this interfacial SOC field is expressed as

$$H_R = \frac{\alpha_R}{\hbar}(\boldsymbol{E} \times \boldsymbol{p}) \cdot \boldsymbol{\sigma}, \tag{10}$$

where α_R is the Rashba parameter and $\boldsymbol{\sigma}$ is the vector of the Pauli spin matrices. There is also an inverse Rashba-Edelstein effect (spin galvanic effect) that generates charge current from the non-equilibrium spin accumulation.

Overall, the charge to spin conversion efficiency of SOT can be much larger than the STT. For STT, the maximum efficiency of STT is 1 with unit of $\hbar/2$ per charge in the current, while for SOT, the charge to spin conversion efficiency can be further enhanced by designing the geometric parameters like the width of FM, the thickness of SOT or SOT material with larger θ_{SH}.

1.3.1.3 Voltage-controlled exchange coupling

The voltage-controlled exchange coupling (VCEC) refers to the modulation of the polarity of the interlayer exchange coupling in a synthetic antiferromagnet. The interlayer exchange coupling (IEC) refers to the ferromagnetic or antiferromagnetic exchange coupling between two ferromagnetic layers through a non-magnetic spacer such as Ru or Ta. The magnitude and the polarity of the interlayer exchange coupling would oscillate when the thickness of the spacer or the ferromagnetic layers change [45]–[47]. The exchange energy of the bilinear IEC can be expressed as

$$\frac{E}{A} = -J\boldsymbol{m_1} \cdot \boldsymbol{m_2}, \tag{11}$$

where J is the coupling constant which may favor parallel ($J > 0$) or antiparallel ($J < 0$) alignments between $\boldsymbol{m_1}$ and $\boldsymbol{m_2}$. It is called bilinear IEC because the energy per unit area is linear in the directions of both $\boldsymbol{m_1}$ and $\boldsymbol{m_2}$. Similarly, the biquadratic IEC is expressed as

$$\frac{E}{A} = -J_2(\boldsymbol{m_1} \cdot \boldsymbol{m_2})^2, \tag{12}$$

where $J_2 < 0$ is the coupling coefficient between $\boldsymbol{m_1}$ and $\boldsymbol{m_2}$ which would favor perpendicular orientations of $\boldsymbol{m_1}$ and $\boldsymbol{m_2}$.

Different from the interlayer exchange coupling which is controlled by the structural parameters, the voltage-controlled exchange coupling happens when different polarity of the electric field is applied to the MTJ. Microscopically, when the electric field is applied to the p-MTJ, the voltage drop across the MgO and the synthetic antiferromagnet (SAF) layer would change, and this voltage drop changes the reflection coefficient of the electron wave functions at the interface; therefore, the polarity of IEC would change as calculated by the ab initio calculations [48]. The Experiment depicted in **Figure 4** also demonstrated the switching of the p-MTJ from antiparallel (AP) to parallel (P) states under positive biases voltages. The VCEC effect is a novel way to use voltage to control the magnetization of the free layer FM and is promising for the application of low power memory devices.

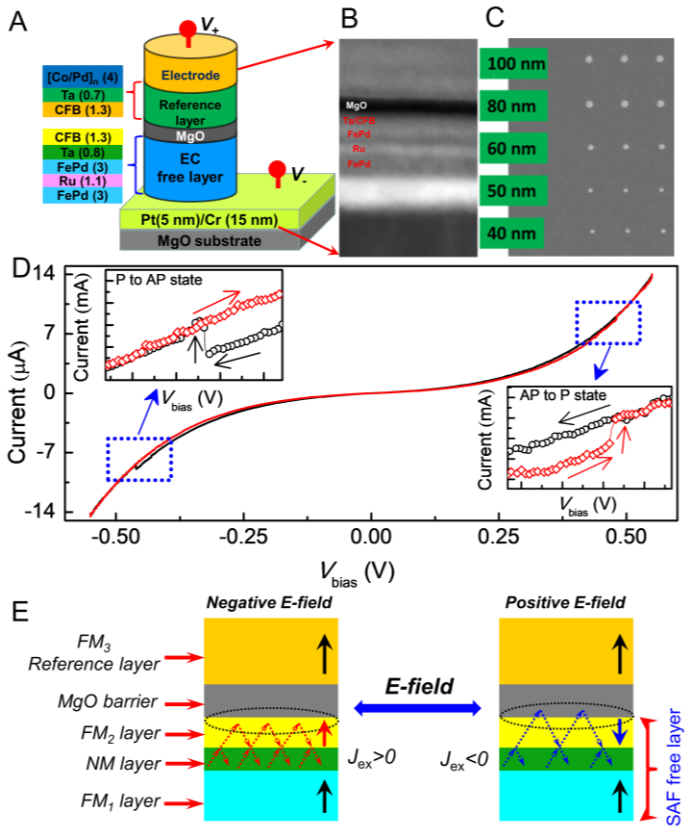

Figure 4 – Bipolar electric field switching in the p-MTJ. (a) Schematic of the FePd synthetic antiferromagnet (SAF) p-MTJ. The free layer of the p-MTJ is composed of two SAF layers: CoFeB (CFB)/Ta/FePd and the FePd/Ru/FePd layers. (b) Cross-section STEM and (c) the SEM images of the FePd SAF p-MTJ. (d) The I-V characteristics of the p-MTJ. (d) Schematics of the bipolar electric field switching in the p-MTJ. The polarity of the interlayer exchange coupling coefficient (J_{ex}) between CFB/Ta/FePd changes as the polarity of the applied electric field changes. [48]

1.3.1.4 Magnetoelectric effect and the magnetoelectric materials

The magnetoelectric (ME) effect refers to the induction of magnetization by an electric field or induction of polarization by a magnetic field. The origin of the ME effect

comes from the coupling between polarization and the magnetic field or the coupling between magnetization and the electric field. Generally, the free energy of the ME materials is expressed as [24]:

$$F(E,H) = F_0 - P_i^S E_i - M_i^S H_i - \frac{1}{2}\epsilon_0\epsilon_{ij}E_iE_j - \frac{1}{2}\mu_0\mu_{ij}H_iH_j - \alpha_{ij}E_iH_j - \frac{1}{2}\beta_{ijk}E_iH_jH_k - \frac{1}{2}\gamma_{ijk}H_iE_jE_k - \cdots \quad (13)$$

By differentiating the free energy with respect to the electric field or the magnetic field, we can obtain the polarization and the magnetization as [24]:

$$P_i(E,H) = -\frac{\partial F}{\partial E_i} = P_i^S + \epsilon_0\epsilon_{ij}E_j + \alpha_{ij}H_j + \frac{1}{2}\beta_{ijk}H_jH_k + \gamma_{ijk}H_iE_j - \cdots \quad (14)$$

$$M_i(E,H) = -\frac{\partial F}{\partial H_i} = M_i^S + \mu_0\mu_{ij}H_j + \alpha_{ij}E_i + \beta_{ijk}E_iH_j + \frac{1}{2}\gamma_{ijk}E_jE_k - \cdots \quad (15)$$

where P_i^S and M_i^S are the spontaneous polarization and magnetization, respectively, ϵ_{ij} and μ_{ij} are the electric and magnetic susceptibilities, and α_{ij} is the linear ME coefficient. The strength of the ME effect is then evaluated by the magnitude of α_{ij}. There are also higher order ME coefficient terms such as β_{ijk} and γ_{ijk}.

Currently, there are two major source of ME effect: 1) the magnetostrictive effect in a composite of a magnetostrictive and a piezoelectric compound, 2) and the intrinsic ME effect in the multiferroic materials. In the magnetostrictive compound, the ME effect happens because of the transfer of strains from the piezoelectric material to the magnetostrictive material when applying an external electric field. When the external electric field is applied, the strain generated by the piezoelectric material changes because of the piezoelectric effect, and then the strain transferred to the magnetostrictive material

causes the magnetic easy-axis to rotate 90°. The magnetostrictive effect can be used in applications such as the voltage-controlled magnetic anisotropy MRAM (VCMA-MRAM). For multiferroic materials, the ME effect originates from the intrinsic coupling between magnetization and polarization inside the material. Multiferroics are materials which show at least two of the following characteristics−ferroelectricity, ferromagnetism, antiferromagnetism, or ferroelasticity [49]. There are four major crystallographic types of multiferroics including 1) compounds with perovskite structure with ABO_3 or $A_2B'B''O_6$ as the general chemical formula, 2) compounds with hexagonal structure with the same general chemical formula but crystallized in a hexagonal structure, 3) boracites with a general formula $M_3B_7O_{13}X$, and 4) $BaMF_4$ where M = Mg, Mn, Fe, Co, Ni, Zn. However, most of these multiferroics have low Curie temperatures or low Neel temperatures.

Bismuth ferrite ($BiFeO_3$) possessing ferroelectricity, G-type antiferromagnetism, and weak magnetization, is the only single-phase multiferroic material known so far, that has both the Curie temperature (T_c~1103K) and the Neel temperature (T_N~643K) well above room temperature. Hence, $BiFeO_3$ is a promising candidate for applications in room-temperature low power devices. To evaluate the potential of the magnetoelectric (ME) devices made up of the $BiFeO_3$/CoFe heterojunction, we will discuss the physical properties of $BiFeO_3$ in the following section, and then we will present the physical model in Chapter 3 and the circuit level performances in Chapter 4.

1.3.1.5 Physical properties of $BiFeO_3$

$BiFeO_3$ (BFO) has a rhombohedrally distorted perovskite structure and belongs to the space symmetry group *R3c* in the thin film structure. Depending on a compressive or

tensile strain, the crystal structure and the space group in a thin film $BiFeO_3$ may vary from tetragonal to orthorhombic as discussed in [50]. The ferroelectricity of $BiFeO_3$ mostly originates from the displacement of Bi^{3+} ions relative to the rest of the lattice under an applied electric field. Thus, the application of a sufficiently strong applied electric field that is larger than the coercive voltage (V_C) of BFO will reverse the polarization [51],[52]. Interestingly, during the polarization reversal, the iron ions and oxygen octahedra also rotate, which cause the weak magnetization to rotate [53]. The weak magnetization in BFO originates from the Dzyaloshinskii-Moriya interaction (DMI) [54],[55], which is due to the tilting of oxygen octahedra from the ideal ABO_3 perovskite structure combined with the spin-orbit coupling effect. The energy of DMI is expressed as

$$F_{DMI} = \sum_{i=1}^{N} \sum_{j \neq i}^{nn} \boldsymbol{D}_{i,j} \cdot \left(\boldsymbol{M}_i \times \boldsymbol{M}_j \right) \tag{16}$$

where $\boldsymbol{D}_{i,j}$ is the DM vector between cells i and j, and $\boldsymbol{M}_i$ and $\boldsymbol{M}_j$ are the magnetic moments of the cells i and j, respectively. The direction of the DM vector is determined by the cross product of the displacement of the oxygen ion from the midpoint between Fe ions ($\boldsymbol{x}$) and the distances between two Fe ions ($\boldsymbol{r}_{ij}$) so that $\boldsymbol{D}_{i,j} = V_0(\boldsymbol{r}_{ij} \times \boldsymbol{x})$ where V_0 is the microscopic constant. From a crystallographic point of view, the rotation of the oxygen octahedra is anti-phase when viewed from the rotation axis, which is also called anti-ferrodistortive axis $\boldsymbol{\theta}$, of BFO [56]. Hence, the displacement of the oxygen ion, $\boldsymbol{x}$, and the DM vector $\boldsymbol{D}_{i,j}$ are both staggered vectors or quasi-axial vectors, and the direction of $\boldsymbol{D}_{i,j}$ is determined by $\boldsymbol{\theta}$ [56]. Ab initio calculations [53] have shown that $\boldsymbol{D}_{i,j}$ is nearly parallel to the polarization during polarization rotation so that this ME coupling determines the switching dynamics of BFO. One can also re-write the energy of DMI as

$$F_{DMI} \approx \sum_{i=1}^{N} \boldsymbol{D}_{i,j} \cdot (\boldsymbol{N} \times \boldsymbol{M_c}) = \boldsymbol{H}_{DMI} \cdot \sum \boldsymbol{M}_i^{AFM} \quad (17)$$

considering there are two sublattices 1 and 2 where $\boldsymbol{N} = (\boldsymbol{M}_1 - \boldsymbol{M}_2) \,/\, (|\boldsymbol{M}_1| + |\boldsymbol{M}_2|)$ is the Neel vector, $\boldsymbol{M_c} = (\boldsymbol{M}_1 + \boldsymbol{M}_2) \,/\, (|\boldsymbol{M}_1| + |\boldsymbol{M}_2|)$ is the weak magnetization, and $\boldsymbol{H}_{DMI} = (\boldsymbol{D}_{i,j} \times \boldsymbol{N})/M_s$ is the effective magnetic field of DMI since the direction of $\boldsymbol{M}_i \times \boldsymbol{M}_j$ is equal to $\boldsymbol{N} \times \boldsymbol{M_c}$. Note that because of the cross-product relation between $\boldsymbol{D}_{i,j}$, $\boldsymbol{N}$, and $\boldsymbol{M_c}$, these three vectors always form a right-handed system [57].

A UNIFIED BENCHMARKING FOR VARIOUS SPINTRONIC MEMORY DEVICES

1.4 Overview of spintronic memory devices

Spintronic devices are promising candidates for embedded memory due to their nonvolatility and small footprint compared with static random access memory (SRAM) [58]. They also offer high endurance and faster write operations compared with resistive random-access memory (RRAM) and embedded NAND flash and better scalability of their write currents compared with phase-change memory (PCRAM) [59]. Spin-transfer-torque magnetorestrictive random-access memory (STT-MRAM), which is gradually moving into production, uses a two-terminal MTJ. When large currents pass through the device, spin-polarized electrons are injected from a fixed ferromagnet to a free ferromagnet. The switching of the free ferromagnet depends on the direction of the current and the magnetic order of the fixed ferromagnet. Recently, perpendicular MTJs with diameters as small as 16 nm and write currents as low as ~40–90 μA [60] have been reported. However, several major challenges remain for the creation of scalable and reliable STT-MRAM. It is generally not energy efficient to switch a magnet using spin-transfer torque because large write currents for several nanoseconds are required. Hence, relatively large access transistors must be used, and reliability issues may arise when large currents pass through the oxide layers in MTJs [61]. Finally, the fact that the write and read currents pass through the same path does not allow for the independent optimization of the read and write operations. To address these challenges, other MRAM device options have been proposed based on various write mechanisms, such as spin-orbit torque (SOT-MRAM), voltage-

controlled magnetic anisotropy (VCMA-MRAM) [62], voltage-controlled exchange coupling (VCEC-MRAM) [48], and magnetoelectric effect (ME-MRAM) [63]. In all these devices, the read operation is based on the tunnel magnetoresistance (TMR) effect [11], [64].

SOT-MRAM utilizes an inherently more energy-efficient mechanism compared with STT-MRAM; hence, it may permit faster and more energy-efficient operations. Theoretically, when a charge current I_C passes through an SOT channel, the generated spin current I_S is written as

$$I_S = \frac{\hbar}{2e}\frac{W_{FM}}{t_{SO}}\theta_{SH} I_C, \tag{18}$$

where e is the electron charge, $\hbar$ is the reduced Planck's constant, W_{FM} is the width of the ferromagnet, t_{SO} is the thickness of the SOT material, θ_{SH} is the spin Hall angle of the SOT material, and the length of the free layer ferromagnet is equal to the width of the SOT material. With the right geometrical and material parameters, this spin current can be several times larger than the spin-polarized current in STT-MRAM whose upper limit is[65]

$$I_S = \frac{\hbar}{2e} I_C. \tag{19}$$

In addition to the current-controlled devices, researchers are pursuing voltage-controlled devices that are potentially more energy efficient because of the much lower write currents involved. VCEC-MRAM is a bidirectional voltage-controlled device in which the polarity of the applied voltage across the MTJ determines the magnetization direction of the free ferromagnet. The ab initio calculations show that the applied voltage close to the oxide

interface can modulate the interlayer exchange coupling in the synthetic antiferromagnet, thus changing the magnetization direction of the free ferromagnet [48]. Another candidate is ME-MRAM that uses multiferroic materials, such as $BiFeO_3$ [53], [44] or Cr_2O_3 [66], in contact with a free ferromagnet of an MTJ. Once the applied voltage across the ME layer is larger than its coercive voltage, its ferroelectric polarization and the antiferromagnetic order will switch. If the interface exchange coupling or the exchange bias effect is large enough, the magnetic order of the adjacent ferromagnet will also switch. To understand the limits and opportunities offered by these novel write mechanisms, various materials, technology, and design parameters must be optimized, and various tradeoffs must be evaluated. Prior publications have compared the potential performance of SOT-MRAM versus STT-MRAM [67], [65]. In addition, researchers have studied several spintronic device candidates and have quantified their array level performances [68]–[70]. However, many new SOT and ME materials have been reported since then, and several important factors, such as current splitting between the SOT and ferromagnet layers, domain nucleation/propagation and thermal noise during the switching process, and the impact of field-like torque, have not been considered in these studies. The array-level potential performances of VCEC-MRAM and ME-MRAM have not been quantified. Finally, a comprehensive cross-layer optimization and benchmarking of all MRAM technology options are lacking. Each spintronic memory option offers vastly different tradeoffs at the material, device, and circuit levels, and a fair comparison requires comprehensive modeling and optimization at all levels. To fill these gaps, this chapter presents a uniform crosslayer optimization and benchmarking of various spintronic memory devices in a 256 × 128 bits array. The simulation framework uses SPICE simulations, analytical equations,

a macrospin model, and micromagnetic simulations. We also explore various material candidates for SOT-MRAM, such as heavy metals, alloys, semimetals, and topological insulators. Note that VCMA-MRAM has not been considered in this work since it requires precise pulse width control [71], [72] or it needs to be combined with STT [72], [73] or SOT for a deterministic magnetization switching. The parameters for each type of MRAM are chosen from the recent state-of-the art experiments, as will be discussed in **Table 2**.

1.5 Schematics and layout of various spintronic devices

The two key factors needed for the array-level modeling of MRAM options are the cell area and the number of transistors per cell as they determine the interconnect lengths and parasitic capacitances. The schematics and the layout designs of the spintronic memory cells are shown in **Figure 5**. We define F = 30 nm as the half-metal pitch in the 16-nm CMOS technology which is consistent with the beyond-CMOS benchmarking presented in [28]. We also consider various numbers of write transistors with a fixed current flowing per transistor to evaluate the write speed.

For the STT-MRAM and the VCEC-MRAM, the layout area can be as small as 12 F^2 if only one-access transistor is used since the read and write operations share the same path. Layout designs of STT-MRAM with one to four access transistors are shown in **Figure 6**. For the SOT-MRAM, since the read and the write operations are separated, two transistors are needed to avoid sneak currents. The layout area unavoidably increases to 20 F^2 in the case of one write access transistor.

For the ME-MRAM, the read and write operations are separated by two access transistors to prevent read disturb, as shown in **Figure 7**(a). The cell area is 20 F^2, which

is similar to the SOT-MRAM using one write and one read access transistor, as shown in the right-hand side of **Figure 5**(c). Interestingly, when the write voltage (V_{write}) of the ME material is as large as 0.4–0.5V, which is higher than the typical read voltage of an MTJ (~0.1–0.15 V), a single access transistor can be used for both read and write operations, as shown in **Figure 5**(b). In this one-access transistor scheme, a leakage current passes through the MTJ during the write operation and the read voltage is applied to the ME stack. As will be discussed later, the leakage current during the write operation can be kept small by a proper choice of MTJ oxide thickness, and a write voltage larger than 0.4 V would ensure no read disturbs. The benefit of using a one-access transistor comes with a smaller layout area of the ME-MRAM down to 12 F^2, as shown in the left-hand side of **Figure 5**(c).

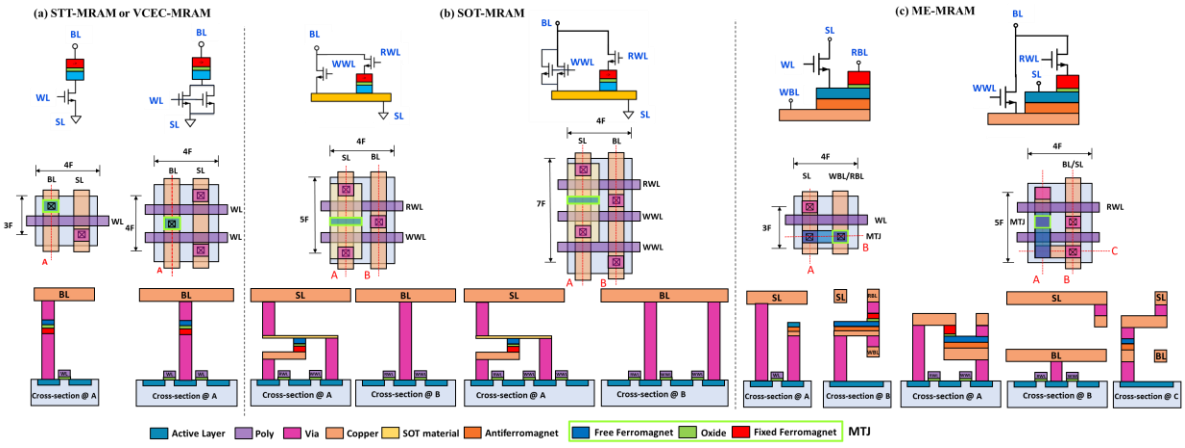

Figure 5 – Schematics and layouts of various spintronic memory cells.

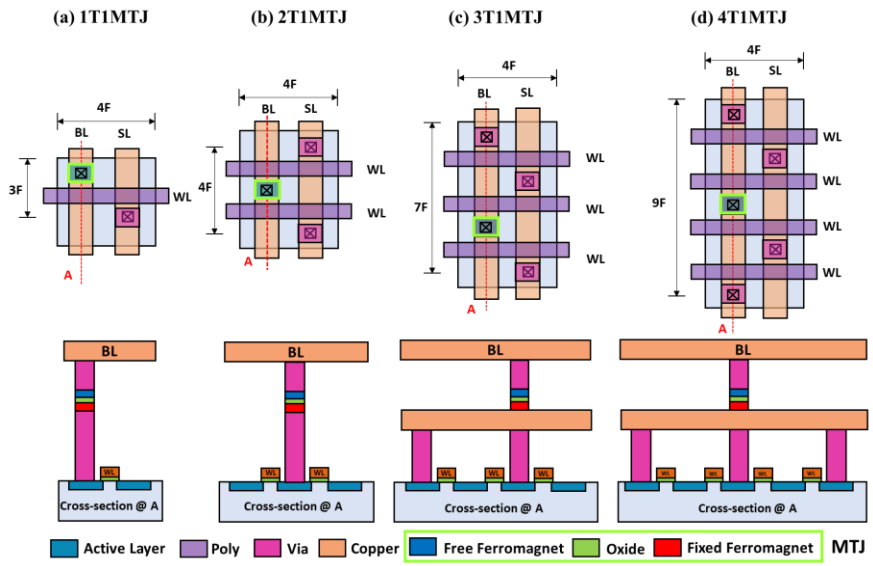

Figure 6 – Layout of STT-MRAM with (a) one, (b) two, (c) three, and (d) four access transistors, and their cross-section areas at line A.

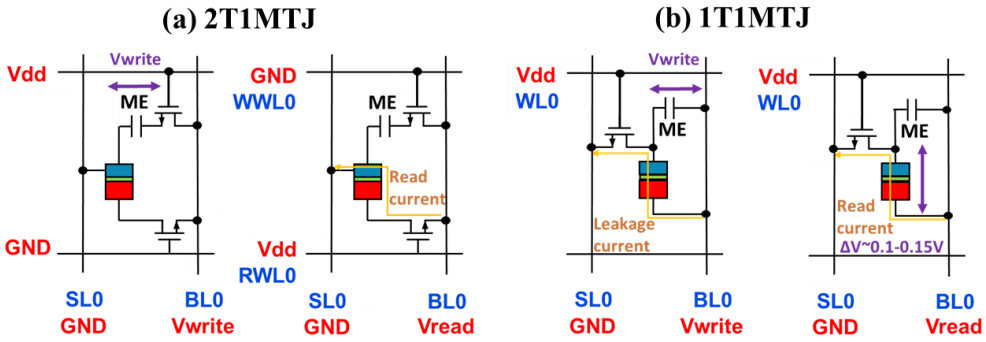

Figure 7 – Schematic of the ME-MRAM in an array-level with (a) one access transistor or (b) separated access transistors for read and write operations.

1.6 Modeling approaches

We consider a 256 × 128 bits array memory, including the memory cells, sense amplifiers, and parasitics, such as wire resistances and wire capacitances in our simulations. The simulation parameters are listed in **Table 1**. To compare various

spintronic memory cells using different write mechanisms, the oxide thickness must be optimized since it affects the read performances of all the options and the write performances of STT-MRAM and VCEC-MRAM.

We will later show that the oxide thickness of SOT-MRAM and ME-MRAM can be optimized especially for the read operation to take advantage of the separated read and write paths. As we vary the MTJ oxide thickness, we use the measured resistance–area (RA) product reported in [35]. In addition, to compare the performances of spintronic memory devices in the embedded memory application, we simulate the read and write performances of SRAM considering that the fin ratio of the pull-down, pass gate, and the pull-up transistors is 1:1:1 using a 16-nm predictive technology model (PTM) established by Arizona State University [74]. The current latch-based sense amplifier is used to simulate the read performance of SRAM.

Table 1 – Modeling parameters used in read and write operations

Parameters	Value
Half metal pitch (F)	30 nm
CMOS driving voltage	1V
Transistor resistance@ W=60 nm	5kΩ
Transistor capacitance@ W=60 nm	60 aF
Interconnect capacitance	0.15 fF/um
BL resistance	20.5 Ω/um
WL resistance	53 Ω/um
Magnet damping coefficient α	0.01
Spin injection coefficient β	0.5
Conductivity of the CoFeB	$7.4\times10^5\ \Omega^{-1}\cdot m^{-1}$
Conductivity of the Co	$1.54\times10^6\ \Omega^{-1}\cdot m^{-1}$
Conductivity of the MnGa	$5\times10^5\ \Omega^{-1}\cdot m^{-1}$

Table 2 – Model dimensions and parameters of various spintronic memory cells

Memory Types	Size of FM (nm^3)	Thermal Barrier E_b (kT)	Thickness (nm)	M_S (A/m)	K_u (J/m^3)	Critical Current/Field	t_{mag}	Reference
STT	30×30×4.6 (PMA)	60	N/A	3×10^5	6×10^4	$I_C = \frac{2e\alpha K_u V}{\hbar}$	[39]	[60]
VCEC	30×30×4.6 (PMA)	60	N/A	3×10^5	6×10^4	$E_c = 425MV/m$	5, 10, 20 ns	[48]
SOT (W)	15×60×2 (IMA)	40	4	1.2×10^6	0	OOMMF	OOMMF	[67]
SOT ($Au_{0.25}Pt_{0.75}$)	15×60×2 (IMA)	40	4	1.2×10^6	0	OOMMF	OOMMF	[75]
SOT (WTe_2)	15×60×2 (IMA)	40	4	1.2×10^6	0	OOMMF	OOMMF	[76]
SOT ($Bi_{0.9}Sb_{0.1}$)	15×60×2 (IMA)	40	10	10^6	0	OOMMF	OOMMF	[77]
SOT (Bi_xSe_{1-x})	15×60×2 (IMA)	40	4, 8, 16	1.2×10^6	0	OOMMF	OOMMF	[78]
ME	90×50×2(IMA)	-	10-50	-	-	$V_{write} = 0.1\sim0.5V$	1, 2, 5 ns	[44], [53]

1.6.1 Read operation

Following prior work [68], [69], we use HSPICE to simulate the read delay and energy with the read circuit adapted from [79], and the offset voltages of the sense amplifier are chosen to be 50 mV. The read delay time is estimated as as $t_{read} = t_{WL} + t_{sense}$, where $t_{WL} = 0.7\ R_{drive}\ C_{WL} + 0.4\ R_{WL}\ C_{WL}$ is the delay time of the word line (WL) and the write driver, and t_{sense} is the delay time of the sense amplifier. Here, R_{drive} is the resistance of the driver which is a 5× minimum-sized inverter, R_{WL} is the interconnect resistance, and C_{WL} is the interconnect capacitance.

The read energy is estimated as

$$E_{read} = 2V_{read}I_{bias}t_{read} + E_{WL} + E_{SA}, \tag{20}$$

where the first term is the Joule heating associated with the currents passing through the controlled and the reference MTJs, $E_{WL} = (C_{WL}/N_{bit} + C_{tran}) V_{read}^2$ is the energy dissipation to charge the WL and the associated gate capacitance per cell, and $E_{SA} = P_{SA} t_{read}$ is the energy dissipation of the output latch of the sense amplifier. P_{SA} is the sense amplifier power, which is estimated to be 0.3 μW based on the previous SPICE simulation results [68]. Note that the read energy is calculated for a single cell in a row by averaging the read energy of the selected row per column.

1.6.2 Write operation

The write delay and energy of a single bit in an array are calculated specifically for each type of memory cells as explained in the following subsections. We assume bits in each row are written simultaneously and calculate the write energy per bit by dividing the write energy of an entire row by the number of cells per row. The parameters that we used and the corresponding references are listed in **Table 2**.

1.6.2.1 STT-MRAM and VCEC-MRAM

For both the STT-MRAM and the VCEC-MRAM, the write current passes through the MTJ, and the set and reset are determined by the applied voltage on the BL and the SL. For the set operation, BL is biased to V_{write} while SL is connected to ground, and the reset operation is done the other way around. The write access time is estimated as $t_{write} = t_{WL} + t_{BL} + t_{mag}$ where t_{WL} is the delay time to charge WL, t_{BL} is the delay time to charge or discharge BL, and t_{mag} is the magnet switching time which is calculated by a macrospin model [39]. We have validated the models with the experimental results from [60]. Note

that since there are no experimental data available on the magnet switching time of the VCEC-MRAM, three hypothetical values of 5, 10, and 20 ns are considered.

The write access energy is calculated as

$$E_{read} = 2V_{read}I_{bias}t_{read} + E_{WL} + E_{SA}, \quad (21)$$

The first term is the Joule heating energy associated with the write current (I_{write}) flowing through the corresponding BL, SL, select transistor, and MTJ. The second term is the energy dissipation to charge the WL capacitance and the associated gate capacitance (C_{tran}) to V_{dd}. The last term is the energy dissipation to charge the capacitance associated with the BL and the total capacitance associated with the source/drain of transistors connected to the BL, which is approximately $C_{tran}/3$ per transistor.

1.6.2.2 SOT-MRAM

We consider four types of SOT materials: 1) heavy metals such as W [80], [81], 2) alloys such as $Au_{0.25}Pt_{0.75}$ [75], 3) semimetals such as WTe_2 [76], and 4) topological insulators such as $Bi_{0.9}Sb_{0.1}$ [77], and Bi_xSe_{1-x} [78]. To perform the write operation, the write access transistor is turned on, and a charge current flows through the SOT channel, which generates a transverse spin current into the MTJ. The ferromagnet shunts a fraction of the current flowing in the SOT channel. This shunt current needs to be accounted for when the conductivity of the magnet is comparable to or smaller than that of the channel. Another factor that affects the current efficiency is the spin transparency at the interface effects, such as spin-scattering and spin mixing, which become prominent when the thickness of the SOT material is too thin [82]–[85]. To switch a ferromagnet with

perpendicular magnetic anisotropy (PMA) using spin-orbit torque, an external magnetic field is needed to break the symmetry. Other approaches such as using antiferromagnet/ferromagnet heterostructures [86], wedging the interface [87], or utilizing interlayer exchange coupling [88] have also been proposed. These approaches were studied in Chapter 5 and 6 and are not discussed here.

The write access time is estimated as $t_{write} = t_{WL} + t_{BL} + t_{mag}$, where t_{mag} is calculated by micromagnetic simulations using the Object Oriented MicroMagnetic Framework (OOMMF) [89]. This is because macrospin models tend to overestimate the required currents for spin-orbit switching of ferromagnets since they neglect the domain nucleation and propagation during switching [90]. We also validate our micromagnetic model by comparing with the magnet switching times reported in the experiments in [80]. The write access energy is then calculated as

$$E_{write} = I_{write}^2(R_{BL} + R_{SL} + R_{tran} + R_{SOT}) \cdot t_{mag} + (C_{WL}/N_{bit} + C_{tran})V_{dd}^2 + (C_{BL} + C_{tran}/3)V_{write}^2, \quad (22)$$

where R_{SOT} is the resistance of the SOT material, and the effective spin-polarized current is $I_S = \frac{\hbar}{2e}\frac{W_{FM}}{t_{SO}}\theta_{SH}I_C$ and $I_C = I_{C,tot} \times \frac{1}{1+s}$. Here, $I_{C,tot}$ is the total charge current flowing through the write access transistor, I_C is the effective charge current flowing through the SOT channel, and the ratio of the shunting current (I_{shunt}) to I_C can be written as

$$s = \frac{I_{shunt}}{I_C} = \frac{\rho_{SO}}{t_{SO}}\frac{t_{FM}}{\rho_{FM}}, \quad (23)$$

where ρ_{SO} is the resistivity of the SOT material, ρ_{FM} is the resistivity of the ferromagnet, t_{FM} is the thickness of the ferromagnet, and t_{SO} is the thickness of the SOT material. To

reduce the current shunting effect, the thickness of the ferromagnet is chosen to be 2 nm except for the case of $Bi_{0.9}Sb_{0.1}$, a 4 nm thick MnGa is used. The ratio between the length and the width of the ferromagnet must be increased to four in order to maintain a sufficient energy barrier of E_b~40 k_BT.

1.6.2.3 ME-MRAM

Although current experiments on multiferroic materials have been on micrometer samples, here we assume that the device lateral dimensions can be scaled down to below 100 nm to fit in our compact layout designs. We also assume the ME material to be intrinsically an ideal insulator (such as $BiFeO_3$ or Cr_2O_3) without leakage current.

The total write access time is estimated as

$$t_{write} = t_{WL} + t_{BL} + 0.7(R_{BL} + R_{tran})C_{AFM} + t_{mag}, \quad (24)$$

where C_{AFM} is the capacitance of the antiferromagnet. In this study, C_{AFM} is calculated as $\kappa_{AFM} \cdot A/d$ where κ_{AFM} = 40 is the dielectric constant of $BiFeO_3$ [91], A is the area of $BiFeO_3$, and d = 30 nm is the thickness of $BiFeO_3$ thin film. Since there is no experimental report about the switching time of the ferromagnet using the magnetoelectric effect, we consider three hypothetical t_{mag} values of 1, 2, and 5 ns, which covers a range from slightly smaller than the predicted switching time in Chapter 3 (1.4nm) to some large values in cases the ferroelectric response is not as fast.

The total write access energy of ME-MRAM depends on the write voltage of the magnetoelectric material as discussed previously. The write voltage depends on the coercive field and the thickness of the magnetoelectric material. Ideally, one can make the

multiferroic material very thin to achieve low write voltages. However, thin ME layers may suffer from large leakage currents or they may lose their multiferroic properties. Here, we assume the ME layer is insulating and we consider write voltages ranging from 0.1V to 0.5V. For the case in which V_{write} = 0.1~0.3V, the write access energy is calculated as

$$E_{write} = \frac{V_{write}^2}{R_{BL} + R_{SL} + R_{tran} + R_{MTJ}} \cdot t_{mag} + \left(\frac{C_{WL}}{N_{bit}} + C_{tran}\right) V_{dd}^2 + \left(C_{BL} + \frac{C_{tran}}{3}\right) V_{write}^2 + C_{AFM} V_{write}^2. \quad (25)$$

For the other case of V_{write} = 0.4~0.5V, the write energy is the same as the case of V_{write} = 0.1~0.3V except we need to exclude the first term since there is no leakage current from the MTJ during the write operation.

1.7 Benchmarking of various spintronic devices

To compare the read and write performances of various MRAM options, we first quantify the impact of the MTJ oxide thickness on the read delay and energy. Next, we calculate the write delay and energy based on the physical models described in the previous section and the reported experimental parameters. Afterwards, we study various trade-offs to select the optimal oxide thickness and discuss the read disturb issue for each memory type. Finally, we compare various spintronic memory cells and summarize the pros and cons of each cell in terms of density, read and write delay, and read and write energies. Note that while the write mechanism is different for each cell, the read operation is the same for all options even though the parasitic resistance and capacitance values may vary depending on the layout area and cell design.

1.7.1 STT-MRAM

To improve the write speed of STT-MRAM, the number of access transistors is varied from 1 to 4 and the corresponding layouts are shown in **Figure 6**. The write current per transistor is kept constant as the MTJ oxide thickness varies such that the magnet switching time remains constant as shown in **Figure 8**(a) (by increasing the write voltage linearly as the MTJ resistance increases). **Figure 8**(a) also shows that four access transistors (4T1MTJ) offer the fastest write operation since the magnet switching time is inversely proportional to the overdrive spin-polarized current passing through the free layer. Next, for the write performance, **Figure 8**(c) presents that the write energy increases exponentially with increasing oxide thicknesses because of the exponential increase in the resistance. In addition, as the number of the access transistors increases, the layout area increases, leading to larger parasitic resistances and capacitances and higher write energy. Similarly, **Figure 8**(b) shows that the read delay also increases with the increase of oxide thickness and number of access transistors. However, as shown in **Figure 8**(d), the read energy initially decreases with the increase in the oxide thickness because of a smaller read current, and then increases as the MTJ resistance and the read time become too large.

A previous study [68] has demonstrated that using an oxide thickness below 1.3 nm may lead to read disturb issues. To achieve the best trade-off among fast read access time and low read/write access energies, we choose an oxide thickness of 1.3nm for STT-MRAM. It should be noted that for very large oxide thicknesses (>1.7nm), the read current is too low for typical sense amplifiers. Also, the write voltage becomes prohibitively large. Hence, there are practical reasons to avoid such large oxide thicknesses in addition to the very large write/read energies and delays.

To summarize, using 2T1MTJ for the STT-MRAM provides a minimum write energy-delay product (EDP) at the cost of a small increase in read and write energies. Note that this 2T1MTJ scheme of STT-MRAM had also been proved to increase write speed in [92].

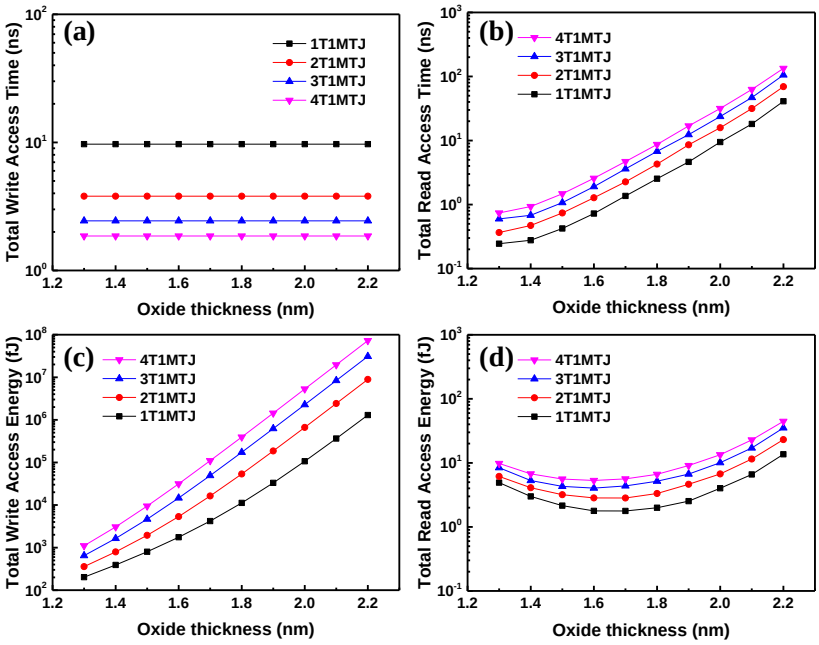

Figure 8 – Write (a), (c) and read (b), (d) performance of STT-MRAM with varying number of access transistors.

1.7.2 VCEC-MRAM

VCEC-MRAM has the same read performance as the STT-MRAM for any given oxide thicknesses since they use the same layout designs. For the write operation, we consider three hypothetical magnet switching times (t_{mag}) of 5, 10, and 20 ns due to the lack of physical models or experimental data at this point. The electric field is kept fixed as we increase the oxide thickness such that the magnet switching time is not affected as

shown in **Figure 9**(a). **Figure 9**(b) reveals that the write energy increases with the oxide thickness when the oxide is thicker than 2 nm. This is due to the increase in the write voltage. However, when the oxide thickness is thinner than 2 nm, the write energy again increases because the Joule heating term described as

$$E_J = V_{write}^2/\left(R_{BL} + R_{SL} + R_{tran} + R_{MTJ}\right) \cdot t_{mag} \tag{26}$$

becomes dominant compared to the dynamic energy which is equal to $(C_{BL} + C_{tran})V_{write}^2$. We choose an oxide thickness of 1.6nm to achieve both low write and read EDP since the read delay time increases when the oxide thickness is too thick as shown in **Figure 8**(b).

Next, we compare the write energy of VCEC-MRAM and STT-MRAM in **Figure 9**(b). A large reduction in the write energy is evident even for a large t_{mag} of 20 ns. This is because VCEC-MRAM is a voltage-controlled device and its write voltage increases linearly with the oxide thickness, whereas STT-MRAM is a current-controlled device, and the write voltage increases exponentially with resistance at a constant overdrive current. Note that since VCEC-MRAM is a voltage-controlled device, it only needs one access transistor during the write operation, leading to a high cell density. Overall, VCEC-MRAM offers lower write energy, small layout area, and better read disturb margin compared to STT-MRAM. However, its read access time is 2-3 times larger because of the larger MTJ resistance.

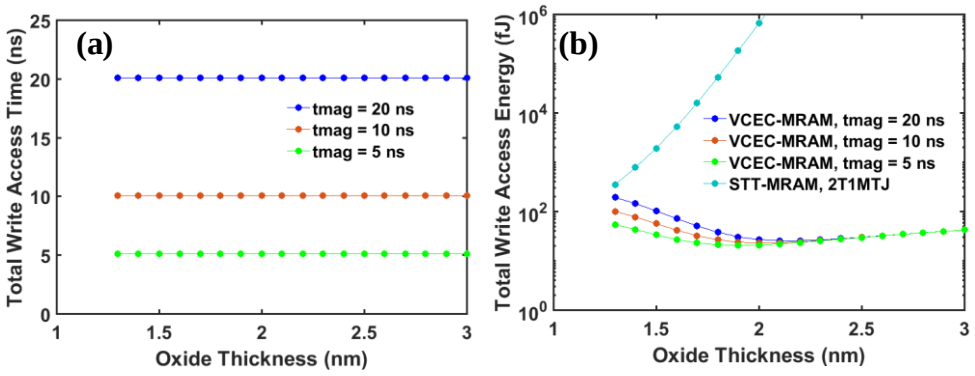

Figure 9 – (a) The write access time with varying oxide thickness of VCEC-MRAM. (b)The comparison of the write access energy with varying oxide thickness for VCEC-MRAM and the STT-MRAM.

1.7.3 SOT-MRAM

Figure 10 (a) presents the read performance of the SOT-MRAM considering one or two write access transistors. The results show that the read access time increases exponentially with the oxide thickness. The cell with two write access transistors (3T1MTJ) has a higher read delay time and read energy compared to the cell with one write access transistor (2T1MTJ) because of the larger footprint area and the larger gate capacitance which results in a higher RC delay.

To study the write operation, we consider four categories of SOT materials: heavy metals, alloys, semi-metals and topological insulators. Heavy metals, semi-metals, and alloys usually have higher conductivities but lower spin Hall angles, whereas topological insulators are quite resistive but have larger spin Hall angles. **Figure 10** summarizes important parameters for various SOT materials studied in this work.

From **Table 3**, Au_xPt_{1-x} has the smallest $s = 0.64$ because it has the lowest resistivity among all the candidates, whereas topological insulators such as Bi_xSe_{1-x} have the largest s of 47.34, when the thickness is 4 nm. This is because the thinner Bi_xSe_{1-x} suffers from a more severe current shunting problem. Note that $Bi_{0.9}Sb_{0.1}$ has an exceptionally high bulk conductivity $\sigma = 2.5\times10^5\ \Omega^{-1}m^{-1}$ which is comparable to the conductivity of the ferromagnet MnGa $\sigma = 5\times10^5\ \Omega^{-1}m^{-1}$; hence, a small shunting factor $s = 0.8$ is obtained.

Next, to evaluate the charge to spin conversion efficiency without considering the current shunting problem, the spin conductivity σ_s is used, which is expressed as the product of conductivity and θ_{SH}. Our calculations show that $Bi_{0.9}Sb_{0.1}$ with a high σ and θ_{SH} has the highest σ_s. Moreover, we incorporate the current shunting effect as illustrated in **Table 3** by considering the normalized write current flowing through the SOT channel, which is defined as $I_{write,nor} = (s+1)\ t_{SO}/(\theta_{SH}W_{FM})$. It is noticed that $Bi_{0.9}Sb_{0.1}$ still shows the lowest $I_{write,nor}$, and a 4nm thick Bi_xSe_{1-x} shows the second lowest $I_{write,nor}$. However, if we compare the ratio of the read current I_{read} to the write current I_{write}, we find that I_{read} is 4× larger than I_{write} for the case of $Bi_{0.9}Sb_{0.1}$. Generally, I_{read}/I_{write} should be lower than 0.1 such that there is enough margin to separate the read and write operations. The read current is typically on the order of a few μA. In the case of $Bi_{0.9}Sb_{0.1}$, the read current flowing through the MTJ and the topological insulator may generate a spin current as large as 100 μA which could flip the free layer ferromagnet. Therefore, $Bi_{0.9}Sb_{0.1}$ may not be a suitable candidate for real applications. Last, to compare the total write energy of these SOT materials, we calculate the normalized $RI_{write,nor}^2$ where R includes the resistance of ferromagnet and SOT channel following the layout design in **Figure 5**(b). **Table 3** indicates that Au_xPt_{1-x} has the second lowest normalized write energy and the smallest

I_{read}/I_{write} of 0.06. Note that even though 4nm thick Bi_xSe_{1-x} has the second lowest $I_{write,nor}$, it has a higher SOT channel resistivity compared to Au_xPt_{1-x}, thus it generally has larger write energy. Also, while 4nm thick Bi_xSe_{1-x} channel offers a higher spin conductivity compared to 8nm thick Bi_xSe_{1-x} channel, it suffers from very poor resistivity which results in a higher energy dissipation due to the large voltage drop across the channel.

To further evaluate the total write performance of various SOT candidates in an array, the optimal write voltages or write currents are calculated to achieve the minimum write EDP for each option. The magnet switching time of a 60 nm long, 15 nm wide, and 2 nm thick ferromagnet with varying spin currents after 100 tests are simulated in OOMMF marked as black squares in **Figure 10**(b). Next, we fit the sample data at each write voltage under thermal noise (T=300K) and extract the switching time based on three times standard deviation above the median value. With varying applied write voltages, the corresponding magnetization switching time is fitted to calculate the total write access energy. **Figure 10**(c) shows that Au_xPt_{1-x} and 8 nm thick Bi_xSe_{1-x} have a lower write energy compared to W and WTe_2 when I_S varies from 25 μA to 75 μA. We then use the optimal write voltages to calculate the total write access time versus the total write energy as shown in **Figure 10**(d). Similar to the calculation we discuss in **Table 3**, $Bi_{0.9}Sb_{0.1}$ has the lowest write energy and write delay time, but it suffers from the read disturb issue. It is interesting to note that while Au_xPt_{1-x} offers a spin conductivity almost 3 times larger than 8 nm thick Bi_xSe_{1-x}, the two channels offer almost similar write energies at the array-level. This is because of the smaller current needed in the case of Bi_xSe_{1-x} which results in smaller voltage drop and energy dissipation in the select transistor and the BL. This fact highlights the need for array-level evaluations of various materials.

We then quantify the write performances of SOT-MRAM when the number of write access transistors increases from one to two such that the total spin current is doubled. It can be seen in **Figure 10**(d) that the write delay time goes down when the number of write access transistors increases, but the write energy increase by 2× because of the larger layout area, larger gate capacitances, and longer interconnects. Overall, the write EDP of the two write access transistor case is larger than the one access transistor case. Therefore, using one write access transistor (2T1MTJ) is better for SOT-MRAM in terms of area and write energy efficiency.

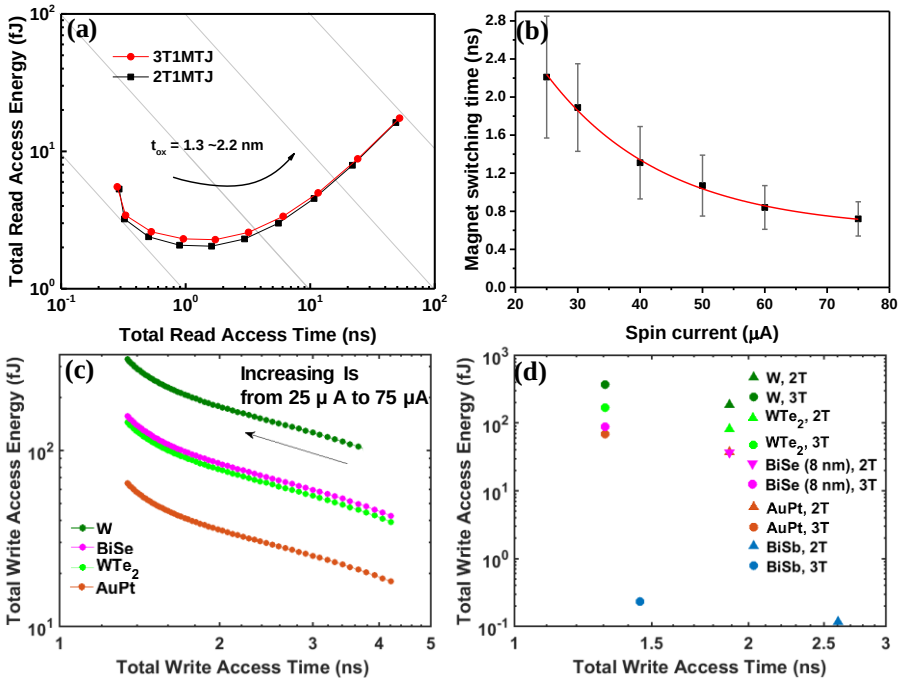

Figure 10 – (a). The read access energy versus the read access time of the SOT-MRAM. (b) The switching time of a 60 nm long, 15 nm wide, and 2 nm thick ferromagnet with varying spin current after 100 tests. (c) The write access energy versus write access

time when spin current increases from 25 to 75 µA. (d) The comparison of the write energy and delay time of various SOT materials using optimum write voltages.

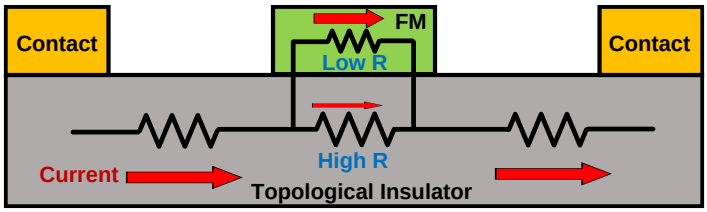

Figure 11 – Schematic of the current shunting problem in SOT-MRAM using a topological insulator.

Table 3 – Comparison of various materials for SOT-MRAM

Class of Materials	Materials	σ ($\Omega^{-1}\cdot m^{-1}$)	s	θ_{SH}	$\sigma_s = \theta_{SH}\cdot\sigma$ ($\Omega^{-1}\cdot m^{-1}$)	Normalized I_{write} ($I_{write,nor}$)	Normalized $RI_{write,nor}^2$	I_{read}/I_{write}
Heavy Metal	β-W (4 nm)	3.85×10^5	0.96	0.2	7.7×10^4	19.6	3.43×10^5	0.35
Alloy	Au_xPt_{1-x} (4 nm)	1.2×10^6	0.64	0.35	4.22×10^5	9.37	2.55×10^4	0.06
Weyl Semimetal	WTe_2 (4 nm)	2.5×10^5	1.48	0.4	10^5	12.4	2.07×10^5	0.07
Topological Insulator	Bi_xSe_{1-x} (4 nm)	7.8×10^3	47.34	18.62	1.45×10^5	5.19	1.08×10^6	6.43
	Bi_xSe_{1-x} (8 nm)	4.65×10^4	3.97	2.88	1.34×10^5	6.91	1.67×10^5	0.26
	Bi_xSe_{1-x} (16 nm)	6.13×10^4	1.51	1.56	9.56×10^4	12.9	2.27×10^5	0.07
	$Bi_{0.9}Sb_{0.1}$ (4 nm)	2.5×10^5	0.8	52	1.3×10^7	0.09	4.16	4.49

1.7.4 ME-MRAM

For the ME-MRAM, we consider the read delay and energy with two different numbers of access transistors as shown in **Figure 12**(a). The results show that both the read delay and energy increase as the number of access transistors increase because of the larger layout area and the associated higher RC delay. To reduce the read EDP, we choose the

oxide thickness to be 1.4 nm. For the write operation, we consider hypothetical magnet switching delay values of 1, 2, and 5 ns. Similarly, the write voltage of the magnetoelectric material is assumed to vary from 0.1 to 0.5 V. **Figure 12**(b) illustrates that the write access energy is dominated by the write voltage that charges or discharges BL and SL since there is no charge current flowing through the MTJ. For V_{write} = 0.4~0.5V, the write access time is smaller than the case of V_{write} = 0.1~0.3V because of the smaller layout area. Overall, the write access energy of the ME-MRAM can be reduced to a few femtojoules if the write voltage is as small as 0.1 to 0.2 V.

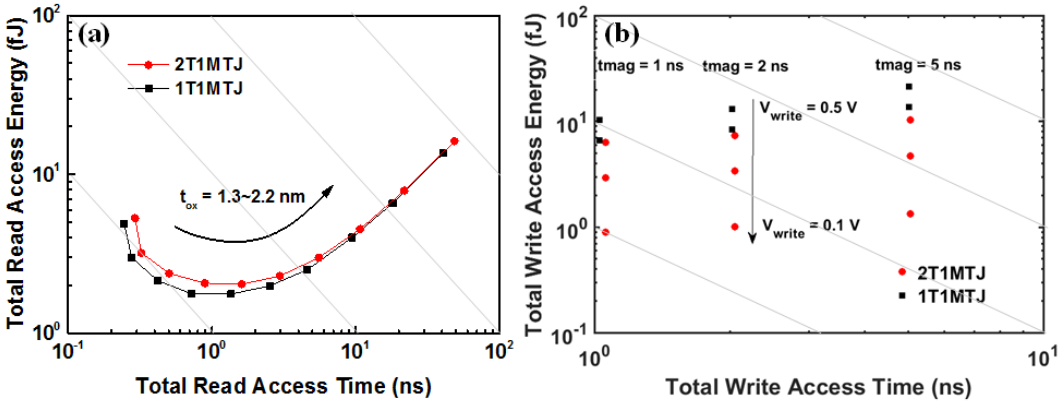

Figure 12 – The write access time (a) and write access energy (b) with varying oxide thickness of ME-MRAM.

1.7.5 Comparison of the read and write performance of spintronic memory cells

Using the optimal oxide thickness and write voltage for each type of memory cell, we compare the read and write performances of various devices. **Figure 13**(a) shows that STT-MRAM has higher write access energy compared to other spintronic memory cells. Although the read access energy of the STT-MRAM is small in the 1T1MTJ case, its write delay is large, and 2T1MTJ is a better option when write speed is a primary concern as

seen by literature [92]. The VCEC-MRAM shows much lower write access energy as compared to STT-MRAM, especially when the magnet switching time is fast. The read access energy of VCEC-MRAM is also small because of its small footprint area, but the read delay time is larger because of a thicker oxide. SOT-MRAM can offer smaller write delay and energy values than those of STT-MRAM as also seen in [65], [67]–[70]; however, the read delay time is longer, and the layout area is larger than STT-MRAM since SOT-MRAM is a three-terminal device. Furthermore, SOT-MRAM using alloy SOT channels presents the lowest write energy among all the SOT materials since it has a larger spin Hall angle compared to heavy metals and semimetals and higher conductivity compared to topological insulators, leading to a weaker current shunting effect. ME-MRAM has a potentially small write access energy and higher cell density compared to other candidates. Because of the small footprint area, the read access energy of ME-MRAM can be as low as that of the VCEC-MRAM when the same oxide thickness is used. Overall, voltage-controlled devices such as VCEC-MRAM and ME-MRAM have lower write access energy and also lower read access energy because of their thicker oxide thicknesses and small footprints compared to other devices.

Finally, we perform a comprehensive benchmarking for all spintronic devices investigated in this work and CMOS SRAM in terms of the read and write performances. **Figure 13**(b) shows that SRAM still offers the fastest write and read delay because it is a charge-based device with positive feedback, whereas spintronic memory devices have slow write and read operations because of the precessional switching behaviour of ferromagnets and their inherently low TMR ratio. Nevertheless, SRAM consumes more energy and area compared to the spintronic memory devices including STT-MRAM with 2T1MTJ, VCEC-

MRAM, SOT-MRAM using $Au_{0.25}Pt_{0.75}$, and ME-MRAM with V_{write} =0.5V as shown in **Table 4**. Our results exhibit that spintronic memory devices using novel physical mechanisms such as VCEC-MRAM, SOT-MRAM, and ME-MRAM are promising options to be used in the last level of cache because of the non-volatility, low write and read energies, and smaller layout area.

It is important to note that the studied MRAM technology options are at different levels of maturity. SOT-MRAM using β-W as the SOT channel has been successfully fabricated in 55 nm CMOS technology with a thermal budget of 400°C [93]. Therefore, SOT-MRAM is a promising candidate that may be adopted in the near future. On the other hand, VCEC-MRAM and ME-MRAM that offer the largest benefits in terms of density and possibly energy are still at the early stages of research and may be considered as long term potential candidates.

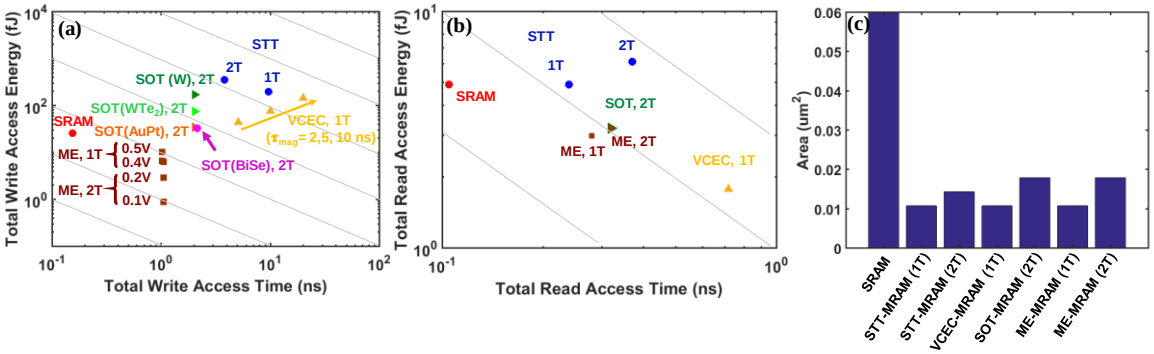

Figure 13 – The total write (a), read (b) performance and layout area (c) of various spintronic memory cells.

Table 4 – Comparison of various spintronic memory cells and SRAM.

Memory Types	SRAM	STT	VCEC	SOT	ME
Area (F^2)	120	16	12	20	12
E_{write} (fJ)	26.36	357.22	43.95	15.13	10.38
t_{write} (ns)	0.15	3.80	5.13	1.39	1.03
E_{read} (fJ)	4.93	6.15	1.78	3.22	2.99
t_{read} (ns)	0.11	0.37	0.72	0.32	0.28

1.7.6 Conclusion

In this work, a comprehensive modelling and optimization framework for various current- and voltage-controlled magnetic memory devices is presented based on experimentally validated physical models considering a range of recently reported materials and devices. For material choices of SOT-MRAM, our cross-layer optimization and benchmarking highlights that common metrics such as spin Hall conductivity (σ_s) and normalized write current ($I_{write,nor}$) may not be sufficient. For instance, Au_xPt_{1-x} offers a spin conductivity more than 3 times larger than 8 nm thick Bi_xSe_{1-x}. However, the two channel materials offer almost similar write energies at the array-level. This is because of the smaller current needed in the case of Bi_xSe_{1-x} which results in smaller voltage drop and energy dissipation in the select transistor and the bit line. The extraordinarily high spin hall efficiency reported for $Bi_{0.9}Sb_{0.1}$ and its high electrical conductivity result in a very high spin conductivity. However, the very low write current can cause in high read disturb rates. A 4nm thick Bi_xSe_{1-x} layer offers a very large spin Hall angle but suffers from large current shunting effects because of its high resistivity and is not a promising option. In general, our benchmarking results considering a simple lump model for the current shunting effect shows that alloys with large spin Hall angles and high conductivity are promising SOT channel materials. A more rigorous analysis for SOT-MRAM including the current

shunting effect, read disturb effect, and variability of devices and process are discussed in Chapter 5.

The design of ME-MRAM cell can be simplified from 2T1MTJ to 1T1MTJ if the write voltage of the ME layer is adequately larger than the read voltage which is typically around 0.1 to 0.2V. Hence, there is a trade-off between memory density and write energy. The benchmarking results show that SOT-MRAM can be fast and low energy but would suffer from 25% larger cell area compared to STT-MRAM. VCEC-MRAM can be denser than STT-RMAM (2T1MTJ) and dissipate less energy but would suffer from slower read operations because of its large oxide thickness. ME-MRAM can be fast, low energy, and dense compared to all other options. Although spintronic memory devices have slower write and read operations compared to SRAM, the characteristics of non-volatility and smaller layout area make them promising options for memory applications.

SIMULATION OF THE SWITCHING DYNAMICS OF MAGNETOELECTRIC DEVICES

1.8 Overview of magnetoelectric device using the BFO/CoFe heterojunction

Magnetoelectric devices [25] are voltage-controlled, which can alleviate the problem of a high threshold current and the accompanying joule-heating effect during and even after magnet switching compared to the current-controlled devices. Current magnetoelectric devices utilize effects such as the voltage-controlled magnetic anisotropy (VCMA) effect in a composite material or the intrinsic magnetoelectric coupling in a single-phase multiferroic material. However, the VCMA effect that comes from the interface charge occupation levels can only rotate the magnetic easy-axis of the ferromagnet by 90º by enhancing or reducing the perpendicular magnetic anisotropy energy. To flip the magnetic moment of a ferromagnet by 180º, which is needed for a magnetic tunnel junction, one has to apply either an extra spin current or a careful control of the applied voltage pulse width [22] for a deterministic magnet switching. Multiferroic materials that have at least two of the ferroic properties, including ferroelectricity, ferromagnetism and ferroelasticity, can successfully switch the magnetic moment of the adjacent ferromagnet by 180º when a reverse electric field is applied, as demonstrated in the case of BFO [53], [94].

To evaluate the potential performance of this voltage-controlled BFO/CoFe heterojunction device in memory or logic devices, it is crucial to model the transient response, switching time, and the switching probability of the magnetic order in the CoFe layer. Nevertheless, previous studies have mainly focused on the domain patterns after switching [95], the shape anisotropy [96], the strain effect [97], and the strength of the

interface exchange coupling field [95], [98], [99] in the multi-domain BFO/CoFe heterojunction. In this work, we first build a physical model of a single-domain BFO thin film. We analyze the switching dynamics and the switching time of the magnetic order in a single-domain BFO thin film with homogeneous weak magnetization after applying the electric field. The dynamics of the magnetic order in BFO is solved by using the Landau-Ginzburg phenomenological theory and LLG equations to verify the consistency of the results. Next, we develop a unified micromagnetic/ferroelectric simulation framework to model the switching dynamics and thermal stability of the single-domain BFO/CoFe heterojunction for the first time. In addition, other models [96], [98], [99]often consider the interface exchange field as an effective Zeeman field such that the mutual coupling of the magnetic orders in BFO and CoFe layers is neglected. In contrast, the interface exchange coupling field in our work is microscopically determined by Heisenberg exchange coupling and the weak exchange bias [100]. Our model is then calibrated with the experimental results as discussed in Chapter 3.2.

1.9 Simulation of the switching dynamics of a single-domain BFO thin film

We choose our BFO sample to be 32 nm thick and 20 nm wide and long, which is a single magnetic or ferroelectric domain in a stripe-domain sample. The nanoscale dimensions are chosen to simplify the domain switching modeling and avoid the complex domain interaction from domain walls, and to consider the potential application of this material in ultra-scaled beyond-CMOS computational and memory devices [4], [44]. Previous studies [53] have shown that the Bi^{3+} ion displacement, Fe^{3+} ion displacement, and the tilting angles of the oxygen octahedra have similar switching paths, which indicates that the ferroelectricity and weak ferromagnetism are coupled during polarization switching, and the switching of the magnetization in BFO can be determined by combining

the ferroelectric and micromagnetic models. In other words, the axial vector $\boldsymbol{D}_{i,j}$ in the micromagnetic simulation can be modified by the polarization in each time step in the ferroelectric dynamics. Therefore, in this work, we simulate the dynamics of $\boldsymbol{P}, \boldsymbol{N}$, and $\boldsymbol{M}_c$ in a BFO thin film following the rotation of polarization and $\boldsymbol{D}_{i,j}$.

1.9.1 Modelling approach of a G-type antiferromagnet

The total energy (F_{tot}) of BFO includes the ferroelectric energy (F_{el}), the magnetic energy (F_m), and the magnetoelectric energy (F_{me}) such that $F_{tot}(\boldsymbol{P}, \boldsymbol{M_i}) = F_{el}(\boldsymbol{P}) + F_m(\boldsymbol{M_i}) + F_{me}(\boldsymbol{P}, \boldsymbol{M_i})$. The ferroelectric energy (F_{el}) is composed of the bulk energy of the polarization $F_{bulk}(\boldsymbol{P})$, the elastic energy of the polarization $F_{elas}(\boldsymbol{P})$, and the electrical energy $F_{elec}(\boldsymbol{P})$ such that $F_{el}(\boldsymbol{P}) = F_{bulk}(\boldsymbol{P}) + F_{elas}(\boldsymbol{P}) + F_{elec}(\boldsymbol{P})$. The magnetic energy ($F_m$) of BFO includes the exchange energy $F_{exch}(\boldsymbol{M_i})$, the anisotropy energy $F_{ani}(\boldsymbol{M_i})$, and the demagnetization energy $F_{dem}(\boldsymbol{M_i})$ such that $F_m(\boldsymbol{M_i}) = F_{exch}(\boldsymbol{M_i}) + F_{ani}(\boldsymbol{M_i}) + F_{dem}(\boldsymbol{M_i})$. The last term is the magnetoelectric energy $F_{me}(\boldsymbol{P}, \boldsymbol{M_i})$ that represents the coupling energy between polarization and magnetization because of the DMI. For the ferroelectric energy $F_{el}(\boldsymbol{P})$, the energy density of each term can be expressed as [101],:

$$F_{bulk}(\boldsymbol{P}) = \alpha_1(\boldsymbol{P}_1^2 + \boldsymbol{P}_2^2 + \boldsymbol{P}_3^2) + \alpha_{11}(\boldsymbol{P}_1^4 + \boldsymbol{P}_2^4 + \boldsymbol{P}_3^4) + \alpha_{12}(\boldsymbol{P}_1^2\boldsymbol{P}_2^2 + \boldsymbol{P}_1^2\boldsymbol{P}_3^2 + \boldsymbol{P}_2^2\boldsymbol{P}_3^2) \tag{27}$$

$$F_{elas}(\boldsymbol{P}) = K_{Strain}(\boldsymbol{P} \cdot \boldsymbol{u})^2 \tag{28}$$

$$F_{elec}(\boldsymbol{P}) = -(c\frac{(\boldsymbol{P}_{dw} - \boldsymbol{P}) \cdot \boldsymbol{P}}{\epsilon_r \epsilon_0} + \boldsymbol{P} \cdot \boldsymbol{E}_{ext}) \tag{29}$$

where $\alpha_1, \alpha_{11}, \alpha_{12}$ are the phenomenological Landau expansion coefficients, $\boldsymbol{u}$ is the axis of strain, K_{Strain} is the strain energy, c is the geometry factor of the averaged domain wall,

$\boldsymbol{P}_1, \boldsymbol{P}_2$, and $\boldsymbol{P}_3$ are the polarization components in *x*, *y*, and *z*- directions, and $\boldsymbol{E}_{ext}$ is the external electric field. We consider the case that the intrinsic strain results in an easy-plane state of polarization normal to the [0 1 1] [53] . The first term in (29) represents the depolarization energy where $\boldsymbol{P}_{dw}$ is the polarization in an adjacent domain, and the second term in (29) represents the external field energy. The depolarization energy is calculated by approximating the depolarization field due to bound charges as the difference between polarizations on the sides of the domain wall. The ferroelectric domain wall here is considered as the depolarization field from the neighboring unswitched domains.

For the magnetic energy $F_m(\boldsymbol{M_i})$, the energy density of each term is expressed as:

$$F_{exchange}(\boldsymbol{M_i}) = A(\vec{\nabla}\boldsymbol{m_i})^2 \tag{30}$$

$$F_{ani}(\boldsymbol{M_i}) = K_{AFM}(\boldsymbol{m_i} \cdot \vec{\boldsymbol{P}})^2 + K_{epi}\boldsymbol{m_z}^2 \tag{31}$$

$$F_{dem}(\boldsymbol{M_i}) = -\frac{1}{2}\mu_0 M_s(\boldsymbol{H_{dem,i}} \cdot \boldsymbol{m_i}) \tag{32}$$

where A is the exchange constant, $\boldsymbol{m_i}$ is the unit magnetization vector which is defined as $\boldsymbol{m_i} = \boldsymbol{M_i}/M_s$, M_s is the saturation magnetization of the sublattice in BFO, K_{AFM} is the bulk anisotropy energy that comes from DM interaction, $\widehat{\boldsymbol{P}}$ is the hard axis of the antiferromagnet, K_{epi} is the anisotropy energy originated from the compressive epitaxial constraint which is along [0 0 1] [102], [103], and $\boldsymbol{H_{dem,i}}$ is the demagnetization field of cell *i*.

The magnetoelectric energy $F_{me}\ (\boldsymbol{P}, \boldsymbol{M_i})$ is expressed as:

$$F_{me}\ (\boldsymbol{P}, \boldsymbol{M_i}) = F_{DMI} = \sum_{i=1}^{N} \boldsymbol{D}_{i,j} \cdot (\boldsymbol{N} \times \boldsymbol{M_c}) \tag{33}$$

where $\boldsymbol{D}_{i,j} = V_0(\boldsymbol{r}_{ij} \times \boldsymbol{x}) \approx V_0\widehat{\boldsymbol{P}}$ is the DM vector with the direction parallel to the polarization energy of the BFO and V_0 is the magnitude of the DMI energy, $\boldsymbol{N}$ is the Neel vector, and $\boldsymbol{M_c}$ is the weak magnetization. We neglect the inhomogeneous magnetoelectric energy since we are considering a single- antiferromagnetic domain BFO.

We then calculate the polarization ($\boldsymbol{P}$) dynamics of BFO by using the LK equation:

$$\gamma_{FE}\frac{\partial \boldsymbol{P}}{\partial t} = -\frac{\partial F_{tot}}{\partial \boldsymbol{P}} = -\frac{\partial (F_{el}+F_{me})}{\partial \boldsymbol{P}}, \tag{34}$$

where γ_{FE} is the 'viscosity coefficient'. Note that $F_{me}(\boldsymbol{P}, \boldsymbol{M_i})$ is neglected in our calculations because it is orders of magnitude smaller compared to other energy terms. We consider an input pulse of the electric field with the duration of 80 ps and a rise time of 5 ps. With these assumptions, the trajectory of the polarization switching, i.e. the two-step polarization switching, calculated by the LK equation is in agreement with the ab initio calculations [53] as will be shown later. The parameters of the ferroelectric model are listed in **Table 5**.

Table 5 – Simulation parameter in the ferroelectric dynamics model [101].

Variable	Value	Units (SI)
$\boldsymbol{P_s}$	0.8	Cm^{-2}
$\boldsymbol{\alpha_1}$	4.9(T-1103) $\times 10^5$	$C^{-2}m^2N$
$\boldsymbol{\alpha_{11}}$	6×10^8	$C^{-4}m^6N$
$\boldsymbol{\alpha_{12}}$	-1×10^6	$C^{-4}m^6N$
$\boldsymbol{\gamma_{FE}}$	5×10^{-3}	*msec/F*
$\boldsymbol{K_{Strain}}$	6×10^8	N/m^2
$\boldsymbol{\epsilon_r}$	54	–
$\boldsymbol{E_{ext}}$	3×10^8	V/m
$\boldsymbol{c}$	0.1	–
$\boldsymbol{D}$	10^4	J/m^3

For the spin dynamics, we are using two methods: 1) the Landau-Ginzburg (LG) theory, and 2). the LLG equation to calculate the dynamics of the magnetization in BFO. The purpose of using these two methods is to compare the consistency of simulation results.

Landau-Ginzburg theory [104], [102], [103] usually describes the dynamics of an antiferromagnet by the Neel vector $\boldsymbol{n}$. Similar to the spin Hamiltonian discussed previously, $\boldsymbol{n}$ is defined as the vector of the difference between magnetic moment densities of two sublattices in an antiferromagnet. The total magnetic energy density of a BFO thin film is similar to (30)-(32) but with $\boldsymbol{n}$ as the order parameter. However, there is no exchange energy associated with the Neel vector since we consider a single-domain BFO thin film with a homogeneous weak magnetization. The DMI energy is approximated as $F_{DMI} = X_{\perp}{\boldsymbol{H}_{DMI}}^2(\widehat{\boldsymbol{P}} \cdot \boldsymbol{n})^2/2$ [104] where $X_{\perp}$ is the magnetic susceptibility that is perpendicular to $\boldsymbol{n}$, and $\boldsymbol{H}_{DMI}$ is the DM field. By taking the derivative of magnetic free energy with respect to $\boldsymbol{n}$, we get the Neel field as:

$$\boldsymbol{f}_n \equiv -\delta_n F = -X_{\perp}{\boldsymbol{H}_{DMI}}^2\big(\widehat{\boldsymbol{P}} \cdot \boldsymbol{n}\big)e_p - 2K_{AFM}\big(\widehat{\boldsymbol{P}} \cdot \boldsymbol{n}\big)\boldsymbol{e}_p - 2K_{epi}\,\boldsymbol{n}_{\boldsymbol{z}} \tag{35}$$

The dynamics of $\boldsymbol{n}$ is then solved by the effective equation of motion for the Neel field [105]

$$\ddot{\boldsymbol{n}}/\tilde{\gamma} = G_1\dot{\boldsymbol{f}}_n + a[\gamma \boldsymbol{f}_n - G_2\dot{\boldsymbol{n}}], \tag{36}$$

where $\tilde{\gamma}$ is the effective gyromagnetic ratio, and G_1 and G_2 are the phenomenological Gilbert damping parameters.

To model both $\boldsymbol{N}$ and $\boldsymbol{M_c}$ of the antiferromagnet more accurately and to easily incorporate the ferromagnet in Section 3.2, we also use the LLG equation in our micromagnetic simulations. Previous studies already demonstrated that the dynamics of an antiferromagnet using the Neel vector is the same as the dynamics of a micromagnet with two sublattices [106] where they both conclude the same equation of motion for the Neel vector. Therefore, we further describe a G-type antiferromagnet with two sublattices *1* and *2*, where the magnetization of one sublattice is antiparallel to another sublattice, and the

dynamics are solved separately for each cell. We will later calculate the time evolution of the order parameter $\boldsymbol{n}$ used in the LG theory to compare with the results solved by a micromagnet with two sublattices. The dynamics of a micromagnet is solved by the LLG equation in each cell, and the time-varying polarization is assumed homogeneously distributed in the sample. We use both OOMMF [89] and our own numerical micromagnetic model based on the finite difference method to compare the results of the two different expressions of DMI. The dynamics of an antiferromagnet is obtained by calculating the LLG equation. In our model, $\boldsymbol{H}_i = \boldsymbol{H}_{ex,ij} + \boldsymbol{H}_{ani} + \boldsymbol{H}_{dem,i} + \boldsymbol{H}_{DMI}$ where $\boldsymbol{H}_{ex,ij}$ is the exchange coupling field from the cell i to its six nearest neighboring cells j, $\boldsymbol{H}_{ani}$ is the anisotropy field composed of bulk anisotropy field from DMI and the anisotropy field that comes from compressive epitaxial constraint, $\boldsymbol{H}_{dem,i}$ is the demagnetization field in the cell i, and $\boldsymbol{H}_{DMI}$ is a magnetic field arising from DM interaction in our OOMMF model whereas in our own micromagnetic solver, the DM Hamiltonian is used. We will compare the differences in the later discussion. The numerical micromagnetic model considers the discretization of the field with each term in the effective field expressed as:

$$\boldsymbol{H}_{ex,ij} = \frac{2A_{AFM}}{\mu_0 M_s} \sum \frac{\boldsymbol{m}(r_i - \Delta_j) - 2\boldsymbol{m}(r_i) + \boldsymbol{m}(r_i + \Delta_j)}{|\Delta_j^2|}, \tag{37}$$

$$\boldsymbol{H}_{ani} = \boldsymbol{H}_{ani,bulk} + \boldsymbol{H}_{ani,epi} = \frac{2K_{AFM}}{\mu_0 M_s}\left(\boldsymbol{m} \cdot \widehat{\boldsymbol{P}}\right) \cdot \widehat{\boldsymbol{P}} + \frac{2K_{EPI}}{\mu_0 M_s}\boldsymbol{m}_z, \tag{38}$$

$$\boldsymbol{H}_{DMI} = -\frac{1}{\mu_0 M_s}\frac{\partial E_{DMI}}{\partial \boldsymbol{m}_i} = -\frac{1}{\mu_0 M_s}\boldsymbol{M}_j \times \boldsymbol{D}_{i,j}, \tag{39}$$

$$\boldsymbol{H}_{dem,i} = \frac{-1}{4\pi}\int \frac{n \cdot \boldsymbol{M}(r')(r - r')}{|r - r'|^3} d^2 r', \tag{40}$$

integrating all the other cells besides the cell i. The details of the calculation of $\boldsymbol{H}_{dem,i}$ are explained in [30]. Note that the polarization direction determines the hard axis of the bulk

anisotropy field because $\boldsymbol{D}_{i,j}$ is a uniaxial vector that is parallel to polarization ($\boldsymbol{P}$) [107]. The schematic of the rotation of easy-plane state during polarization reversal is shown in the experiment [107].

The simulation parameters in the micromagnetic model are listed in **Table 6** [95]. The negative sign of K_{AFM} and K_{EPI} refers to the magnetic easy-plane state.

Table 6 – Simulation parameters in the magnetic dynamics model

Variable	Value	Units (SI)
$\boldsymbol{M_s}$	4.26×10^5	*A/m*
$\boldsymbol{K_{AFM}}$	-1.75×10^4	J/m^3
$\boldsymbol{K_{EPI}}$	-1.75×10^4	J/m^3
$\boldsymbol{A_{AFM}}$	-2.6×10^{-12}	*J/m*
$\boldsymbol{H_{DMI}}$	1000	*Oe*
$\boldsymbol{\alpha}$	0.01	-
$\boldsymbol{\gamma}$	2.21×10^5	$(A/m)^{-1}s^{-1}$
Variable	Value	Units (SI)
$\boldsymbol{M_s}$	4.26×10^5	*A/m*
$\boldsymbol{K_{AFM}}$	-1.75×10^4	J/m^3

1.9.2 Dynamics of the coupled polarization, antiferromagnetic order, and oxygen octahedra of BFO

We analyze the switching dynamics of BFO by using two unitless vector variables $\boldsymbol{N} = (\boldsymbol{M_1} - \boldsymbol{M_2})/(|\boldsymbol{M_1}| + |\boldsymbol{M_2}|)$ and $\boldsymbol{M_c} = (\boldsymbol{M_1} + \boldsymbol{M_2})/(|\boldsymbol{M_1}| + |\boldsymbol{M_2}|)$, which refer to the Neel vector and the weak magnetization of the antiferromagnet, respectively. At the initial stage before the switching starts, **Figure 14**(a) shows that $\boldsymbol{M_c}$, which is calculated by averaging the magnetization in every 1 nm of the thickness, is staggered in the *x*, *y*, and *z* directions and the magnitude is stronger particularly in a thin region (~2 to 3 nm) close to the surface. To understand the staggering behavior and the stronger amplitude of $\boldsymbol{M_c}$ close to the surface, it should be noted that the antiferromagnetic exchange coupling field is stronger than the anisotropy and DM fields. The exchange coupling field of the surface

cells is weaker than the bulk cells because of fewer neighboring cells. Because of the weaker exchange coupling field, the spin vectors on the surface tilt more by the DM field compared to the cells in the bulk region as shown in **Figure 14**(b), which cause a stronger weak magnetization on the surface cells. However, since the exchange coupling field is a short-range field on the order of a few angstroms that becomes negligible to the second nearest neighbors, the staggered $\boldsymbol{M_c}$ only occurs at the surface of BFO where the breaking of magnetization symmetry happens and the magnitude of $\boldsymbol{M_c}$ decreases rapidly from the surface to the bulk region. Note that this staggered $\boldsymbol{M_c}$ is enhanced by a stronger DM field because of larger asymmetry field for the magnetization. Conversely, $\boldsymbol{M_c}$ shows a net magnetization in the bulk region because the spin vectors are almost anti-parallel to each other and the DM field creates a weak, unidirectional magnetization. The magnitude of the DM field is calculated by comparing the value of $\boldsymbol{M_c}$ to the saturation magnetization in the hysteresis loop of the BFO thin film in experiments [108]. The peak value of $\boldsymbol{M_c}$ is approximately 1.8×10^3 A/m, which corresponds to about 1000 Oe $\boldsymbol{H_{DMI}}$ in our model.

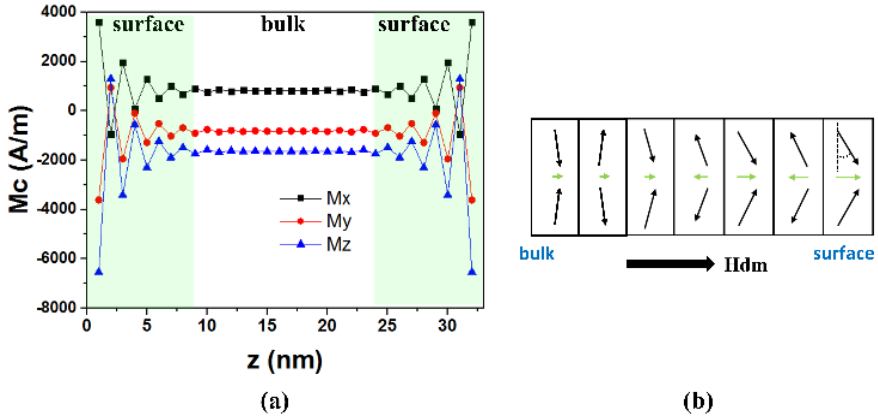

Figure 14 – (a) M_c in 32 nm AFM with H_{DMI}=1000 Oe. (b) Schematic of magnetic moments inside a 1D antiferromagnet array under weak DM field. The black arrows represent the spin vectors and the green arrows represent the direction of M_c.

Next, to understand the energy barrier and the preferred-axis during polarization reversal, we plot the energy landscape in **Figure 15** considering the bulk anisotropy energy and the anisotropy energy that comes from the epitaxial constraint. We define the polar angle between the magnetization and *x*-axis as θ, and the azimuthal angle between the magnetization and the *y*-axis on the *yz* plane as φ. The results show that when $\boldsymbol{H}_{ani,epi}$ is larger than $\boldsymbol{H}_{ani,bulk}$, the lowest energy of magnetization lies in the *xy* plane, and the maximum energy barrier happens at [0 0 1] and [0 0 -1]. However, when $\boldsymbol{H}_{ani,bulk}$ is larger than $\boldsymbol{H}_{ani,epi}$, the preferred easy-plane changes to [1 -1 1], where the hard-axis is parallel to the polarization direction. Considering the superposition of $\boldsymbol{H}_{ani,bulk}$ and $\boldsymbol{H}_{ani,epi}$, the preferred easy-axis becomes along [1 1 0], which is consistent with the experimental results [107]. This is because the epitaxial constraint lifts the preferred easy-plane state and results in a unique easy-axis state. Because of the rotation of the $\boldsymbol{H}_{ani,bulk}$ along with the polarization, the easy-axis of BFO rotates during polarization switching. The energy map in **Figure 15** suggests that the energy barrier of the magnetization switching in BFO is small because the single-ion anisotropy energy from Fe is small when its *d* orbitals are half-filled [109].

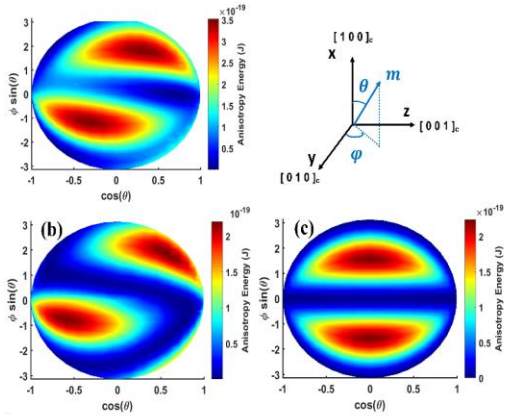

Figure 15 – Energy landscape of BFO thin film when (a). K_{AFM} = K_{EPI} = -1.75×10^4 J/m^3 (b). $K_{AFM} = -1.75 \times 10^4$ J/m^3 and (c). $K_{EPI} = -1.75 \times 10^4$ J/m^3

We now study the dynamics of $\boldsymbol{P}$, $\boldsymbol{N}$ and $\boldsymbol{M_c}$ in BFO by applying a negative electric field $\boldsymbol{E}_{ext} = 3 \times 10^8\ A/m$. **Figure 16** demonstrates that the switching curve of $\boldsymbol{P}$ qualitatively matches the ab initio calculation results in [53], and $\boldsymbol{N}$ switches 180^0 while $\boldsymbol{M_c}$ remains in the same direction after the polarization switching. The switching curves of $\boldsymbol{N}$ also show that $\boldsymbol{N}$ would first rotate 90^0 to [-1 1 0] and then rotate to [1 1 0], which is consistent with the ab initio calculation results in [53]. Next, we find that both the LG theory, which solved the order parameter $\boldsymbol{n}$, and the OOMMF model, which solved for both $\boldsymbol{N}$ and $\boldsymbol{M_c}$, show the same results that $\boldsymbol{N}$ switches 180^0 during polarization reversal in **Figure 16**(b). This demonstrates that our micromagnetic model is consistent with the previous approaches that used the LG theory [104], [102]. However, unlike the LG theory, our micromagnetic model can describe weak magnetization ($\boldsymbol{M_c}$). Note that the final $\boldsymbol{N}$ is not precisely along [1 1 0] because in a BFO thin film, the polarization will deviate from [1 -1 1] in the tetragonal lattice. Hence, $\boldsymbol{N}$, which is perpendicular to $\boldsymbol{P}$, deviates from [1 1 0]. **Figure 16**(c) shows that the *x* and *y* components of $\boldsymbol{M_c}$, are oscillating to -*x* and +*y* directions initially; however, $\boldsymbol{M_c}$ rotates back to the initial direction because of the right-

handed relation governing $\boldsymbol{D}$, $\boldsymbol{N}$, and $\boldsymbol{M_c}$. Therefore, both $\boldsymbol{D}$ and $\boldsymbol{N}$ switch 180^0 after polarization reversal while $\boldsymbol{M_c}$ remains non-switched. The driving force for magnetic switching during the polarization reversal comes from the magnetoelectric coupling including the rotation of bulk anisotropy energy and the $\boldsymbol{H_{DMI}}$. Our findings contradict the results from the first principle calculations in [57], which indicate that $\boldsymbol{M_c}$ switches but $\boldsymbol{N}$ does not after polarization reversal; however, our results are consistent with literature [53] in BFO/CoFe heterojunction which only track the easy-axis of BFO and it remains unchanged after the polarization switching. In fact, we also see cases in which $\boldsymbol{M_c}$ switches and $\boldsymbol{N}$ does not in our simulations if the polarization switches very fast as will be shown in the later discussion. Besides, since BFO is a G-type antiferromagnet with weak magnetization, the demagnetization energy is negligible compared to that of a ferromagnet. Hence, the damping precession is suppressed, and the switching speed becomes faster. The trajectories of $\boldsymbol{N}$ switching also shows that $\boldsymbol{N}$ only lies in the *xy* plane and thus, $\boldsymbol{N}$ switches much faster with less precession or oscillation compared to the magnetic moment of a ferromagnet.

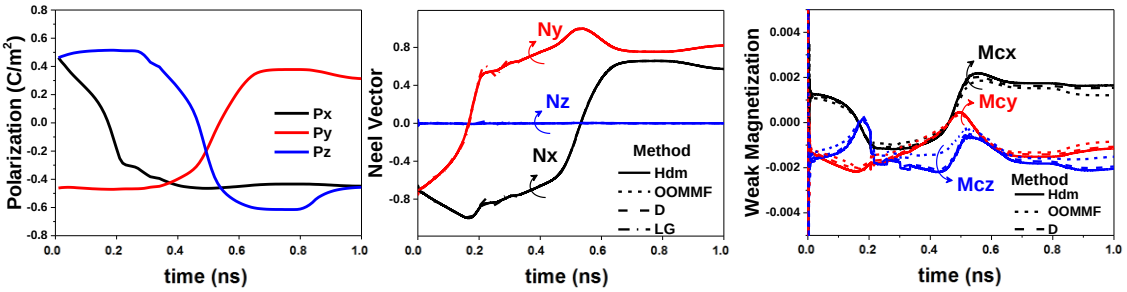

Figure 16 – The switching dynamics of (a) polarization, (b) Neel vector, and (c) weak magnetization in 10 nm thick BFO thin film with $K_{AFM} = K_{EPI} = -1 \times 10^6$ J/m^3 and

$H_{DMI} = 1000\ Oe$ simulated by OOMMF, MATLAB where DMI is an effective magnetic field (*Hdm*) or from spin Hamiltonian (*D*), and LG theory.

Next, we look at the simulation results when the DM interaction is calculated using a spin Hamiltonian instead of a magnetic field. **Figure 16** illustrates that the switching curves obtained from the numerical micromagnetic model, which uses a spin Hamiltonian to represent DMI, and OOMMF, which uses a magnetic field to represent the DM field, match well. This validates the equivalence of the two expressions of the DMI. From our numerical micromagnetic model, we can obtain the spatial distribution of the effective magnetic field of each sublattice. One can see from **Figure 17** that $\boldsymbol{H}_{ex,ij}$, $\boldsymbol{H}_{ani,bulk}$, and $\boldsymbol{H}_{dem,i}$ are staggered fields, while $\boldsymbol{H}_{DMI}$ is a uniform field. The reason for a uniform DM field is because the magnetization and $\boldsymbol{D}_{i,j}$ are both staggered vectors. Hence, we believe that the cross product of them can be approximated as a magnetic field as we have done in our OOMMF model. For an antiferromagnet, a staggered field creates a precessing torque on the Neel vector, while a homogeneous field cants the magnetic moment without reorienting the Neel vector if the magnetic field does not reach the spin-flop transition field [110], which is consistent with our results.

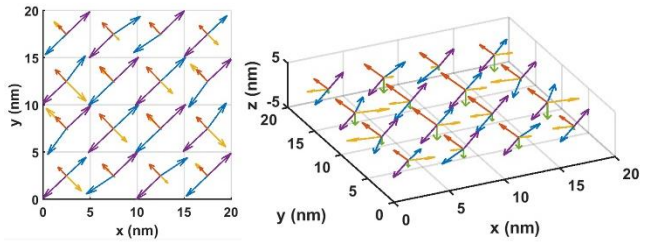

Figure 17 – Spatial distribution of the effective magnetic field including $H_{ex}(violet)$, $H_{ani,bulk}(yellow)$, $H_{ani,epi}(green)$, $H_{dem}(blue)$, and $H_{DMI}(red)$ in AFM with z = 1 nm.

We then evaluate the theoretical antiferromagnetic switching time of a single-domain BFO thin film for various hypothetical polarization switching times by varying the viscosity coefficient γ_{FE}. In previous experiments, it has been reported that increasing the magnitude of the electric field in (100) BFO thin film improved the polarization switching time from seconds to microseconds [111]. However, those experiments involved very large samples sizes (~area of $750\ \mu m^2$ and thickness of 300 *nm*) and the parasitics of the sensing circuits were quite dominant [112]. We analyze the switching time of $\boldsymbol{N}$ as we hypothetically vary the polarization switching time T_{FE} from 10 *ps* to 1 *ns* in **Figure 18**. The results show that the switching time of $\boldsymbol{N}$ is proportional to $T_{FE,}$ and in general, is longer than T_{FE}. In addition, when the polarization switching time is as fast as 10 to 20 *ps*, the spin vectors in the antiferromagnet cannot respond and $\boldsymbol{N}$ remains non-switched whereas $\boldsymbol{M_c}$ switches, which corresponds to a switching failure of $\boldsymbol{N}$. For T_{FE} values larger than 30 *ps*, $\boldsymbol{N}$ switches but $\boldsymbol{M_c}$ does not switch. Therefore, one can consider 30 *ps* as a theoretically calculated lower limit of the antiferromagnetic switching time of a BFO thin film device when K_{AFM} is $-1.75 \times 10^4\ J/m^3$. We can also roughly calculate this minimum time of magnetization reorientation, or called magnetic relaxation time, using $\frac{1}{f} = \frac{2\pi}{\gamma}\frac{1}{H_{eff}} \approx 36\ ps$ where f is the ferromagnetic resonance frequency, and H_{eff} is the effective applied magnetic field, which is $H_{ani,bulk}$ in the case of BFO. When T_{FE} is shorter than the magnetic relaxation time, $\boldsymbol{N}$ cannot switch but the coupling between $\boldsymbol{P}$, $\boldsymbol{N}$, and $\boldsymbol{M_c}$ then forces $\boldsymbol{M_c}$ to switch 180^0 after the polarization reversal.

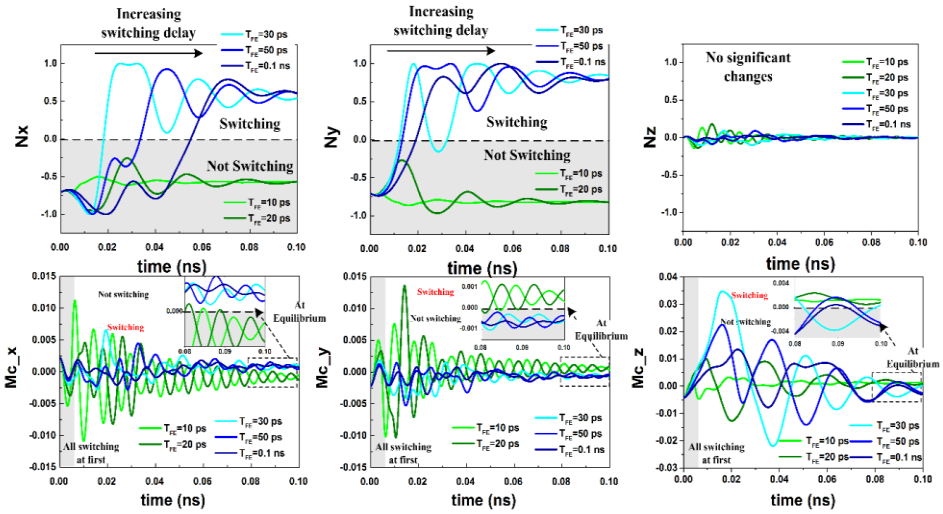

Figure 18 – Switching curves of BFO thin film with varying T_{FE}

To check the sensitivity and the critical parameters that affect the switching dynamics of BFO, the magnitudes of various parameters such as J_{AFM}, K_{AFM}, and K_{EPI} are varied. We find that when the exchange coupling field becomes smaller than $-2.6 \times 10^{-13}\, J/m$, the switching trajectories of $\boldsymbol{M_c}$ becomes highly oscillatory as shown in **Figure 19**. This is because the deviation of spin vectors from their preferred-axis increases under a weak exchange coupling field. In contrast to the case when the exchange coupling field is strong, the switching of $\boldsymbol{N}$ fails and the switching time of $\boldsymbol{M_c}$ increases because of the characteristics of oscillatory switching. Regarding K_{AFM} and K_{EPI}, they both affect the magnitude of the energy barrier. However, K_{AFM} also affects the driving force for magnetization switching because K_{AFM} originates from the DMI and is proportional to the polarization and the electric field. Thus, increasing K_{AFM} increases the effective field and the energy barrier of the AFM thus implies a higher switching success rate under thermal noise, a shorter minimum input pulse width, and a shorter switching time because of a

shorter period of oscillation. For the compressive constraint, increasing K_{EPI} affects the crystal structure of BFO to be more tetragonal-like thus magnetic moments would further lie in the in-plane direction. To have a successful and faster Neel vector switching, the magnitude of K_{AFM} and K_{EPI} need to increase for a sufficient energy barrier to alleviate the thermal noise effect and also to reduce the relaxation time of BFO.

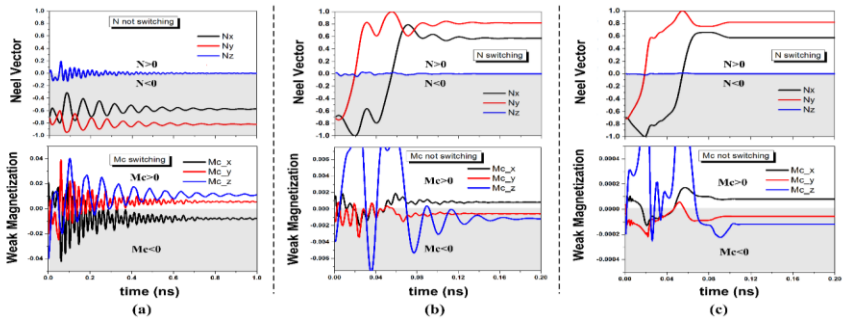

Figure 19 – The switching dynamics of Neel vector and M_c of the BFO thin film with (a) J_{AFM} = -0.26 pJ/m, (b) -2.6 pJ/m, and (c) -26 pJ/m.

We have analyzed the switching dynamics of a single-domain BFO thin film by solving LK and LLG equations, simultaneously. In comparison to the previous model of LG theory using the Neel vector as the order parameter, our model uses the magnetization as the order parameter and solves the LLG equations in two sublattices thus can model both the Neel vector and the weak magnetization accurately. Our results present that BFO as a G-type antiferromagnet has staggered spin vectors thus staggered DM vectors, which create a weak magnetization by tilting spin vectors unidirectionally. We also show the weak magnetism is strongly enhanced in a thin layer (2-3nm) near the surface of BFO because of the broken inversion symmetry. From the analysis of the energy landscape, we demonstrate that the preferred-axis of the magnetic moment in BFO is determined by both the bulk DMI energy

that couples to polarization, and the epitaxial strain that comes from the substrate. We then show for the first time that $\boldsymbol{N}$ rotates 180^0 while $\boldsymbol{M}_c$ remains unchanged by rotating polarization 180^0. This result is further verified by solving the effective equation of motion for the Neel vector in the LG theory. The driving force of the magnetic switching is due to the magnetoelectric coupling such that the easy-plane state and $\boldsymbol{H}_{DMI}$ rotate along with the polarization. By checking the sensitivity of parameters, we find that the probability of switching of $\boldsymbol{N}$ depends not only on the anisotropy energy barrier but also on the exchange coupling field in BFO. We further calculate the lower limit of the switching time of BFO to be around 30 ps assuming the polarization can be switched as fast. $\boldsymbol{N}$ cannot be switched if the polarization switches faster than 30 ps.

1.10 Simulation of the switching dynamics of a BFO /CoFe bilayer thin film

In this section, we consider a thin film (100)-oriented BFO grown on $DyScO_3$ substrate and layered by a CoFe thin film on top. We use the methodology in the previous section to calculate the polarization and the spin dynamics of the BFO. Next, we first extract the magnitude of the interface exchange coupling coefficient J_{int} from the experimental data in giant magnetoresistance measurement (GMR) curve and magnetic hysteresis (M-H) loop measurement. We then calculate the polarization and the spin dynamics of BFO by solving the electric polarization in each time step after applying an electric field and substituting the value of $\boldsymbol{P}$ in the micromagnetic model. The rotation of $\boldsymbol{P}$ during the electric field reversal would first rotate the antiferromagnetic order in the BFO layer which is followed by the switching of the magnetization of the CoFe layer because of the interface exchange coupling. We then calculate the switching time limits of CoFe in

a BFO/CoFe by the interface exchange coupling and show that it is highly dependent on the polarization switching time (T_{FE}) of BFO. In the final part, we discuss the thermal stability of this BFO/CoFe heterojunction by analyzing the switching success rate and the energy barrier of the device. Our modeling approach in unifying the simulations for ferroelectric, antiferromagnetic and ferromagnetic orders is illustrated in **Figure 20**.

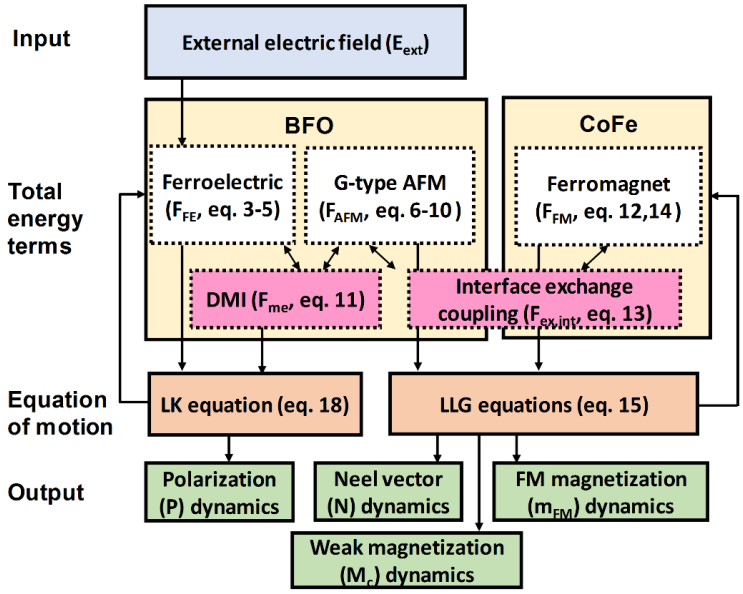

Figure 20 – Modeling approach in unifying the simulations for ferroelectric, antiferromagnetic and ferromagnetic orders

1.10.1 Dynamics of the BFO/CoFe heterojunction

1.10.1.1 Interface characteristics of the BFO/CoFe heterojunction

The interface exchange interaction and the interface properties between BFO and CoFe thin films are investigated by the micromagnetic simulations using OOMMF. The magnetization of CoFe is expressed as $\boldsymbol{M_{FM}}$. At the initial stage before applying an electric field on the of the BFO/CoFe heterojunction, the weak magnetization in BFO shows a

staggered behavior when averaged in the *z* direction in **Figure 21** (a). The staggered $\boldsymbol{M_c}$ is because of the antiferromagnetic exchange coupling inside BFO. Besides, when $\boldsymbol{M_c}$ is close to the interface of CoFe, the magnitude of $\boldsymbol{M_c}$ is stronger than the bulk region of BFO due to the stronger interface exchange coupling that breaks the symmetry of BFO. Therefore, if we compare the staggered $\boldsymbol{M_c}$ under weak or strong DM field ($\boldsymbol{H_{DM}}$) in the bulk BFO, i.e. $\boldsymbol{H_{DM}} = 0\ Oe$ versus $\boldsymbol{H_{DM}} = 10^4\ Oe$ in **Figure 21** (a) and (b), we find that there exists finite $\boldsymbol{M_c}$ close to the interface of FM in both cases, while $\boldsymbol{M_c}$ in the bulk region of the weak DM field case oscillates at zero magnetization. This proves the dominancy of the interfacial exchange in creating $\boldsymbol{M_c}$ in an AFM/FM heterojunction compared to the bulk FM field.

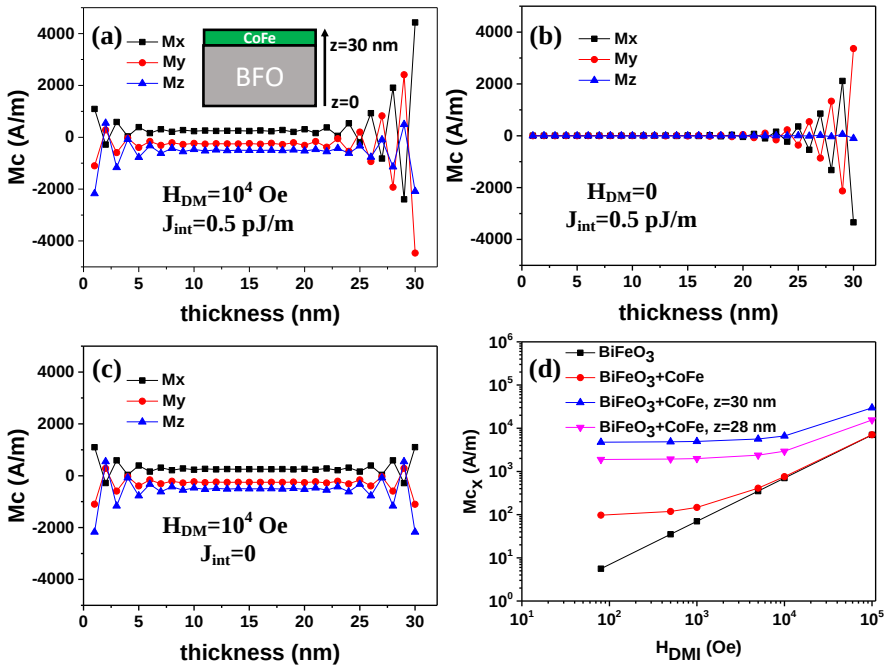

Figure 21 – (a) $\boldsymbol{M_c}$ in 32 nm BFO with $\boldsymbol{H_{DM}}$ = 10^4 Oe, $\boldsymbol{J_{int}}$=0.5 pJ/m. (b) $\boldsymbol{M_c}$ in 32 nm BFO with $\boldsymbol{H_{DM}}$ = 0 Oe, $\boldsymbol{J_{int}}$=0.5 pJ/m. (c) $\boldsymbol{M_c}$ in 32 nm BFO with $\boldsymbol{H_{DM}}$ = 10^4 Oe, $\boldsymbol{J_{int}}$=0 pJ/m. (d) The magnitude of $\boldsymbol{M_c}$ in the BFO(black) or in the BFO/CoFe heterojunction

at the interface (blue), close to the interface(magenta), or the average value(red) when J_{int}=0.5 pJ/m.

Previous studies [53][95] also show that the magnitude of $\boldsymbol{M_c}$ for BFO coupled to the CoFe is strongly enhanced compared to $\boldsymbol{M_c}$ in BFO only case where the magnitude of $\boldsymbol{M_c}$ increases from 1.8×10^3 A/m [113] to 6×10^3 A/m [53]. To evaluate the consistency of our model with the experimental results, we consider two scenarios with various magnitudes of $\boldsymbol{H_{DM}}$ in BFO: a stand-alone 30 nm thick BFO layer versus a 30 nm thick BFO/2 nm thick CoFe heterojunction. **Figure 21**(d) shows that the enhancement of $|\boldsymbol{M_c}|$ is larger at low $\boldsymbol{H_{DM}}$ than at high $\boldsymbol{H_{DM}}$ because the interface exchange coupling field is relatively stronger than the bulk DMI at low $\boldsymbol{H_{DM}}$. Furthermore, we observe that under high $\boldsymbol{H_{DM}}$, $|\boldsymbol{M_c}|$ of a stand-alone BFO coincides with the case of BFO/CoFe, which indicates that $|\boldsymbol{M_c}|$ becomes dominated by the bulk DMI rather than the interface exchange field. **Figure 21**(d) also shows that $|\boldsymbol{M_c}|$ at z = 30 nm is stronger than $|\boldsymbol{M_c}|$ at z=28 nm, and these interfacial $|\boldsymbol{M_c}|$ values are insensitive to the magnitude of $\boldsymbol{H_{DM}}$ when $\boldsymbol{H_{DM}}$ is smaller than 10^4 Oe. Therefore, the behavior of the interface properties, the interface exchange coupling, and $|\boldsymbol{M_c}|$ all depend on the value of J_{int}. On one hand, J_{int} is desired to be large enough to provide strong coupling between the antiferromagnet and ferromagnet. On the other hand, J_{int} needs to be smaller than the intrinsic exchange coupling inside BFO and CoFe.

1.10.1.2 Experimental verification of interface properties

To extract the simulation parameter J_{int} from experiments, we consider a stack of a 30 nm thick BFO thin film, a 2 nm thick CoFe thin film (free layer ferromagnet, or free

layer FM), a 2 nm thick Cu layer, and a 2 nm thick top layer CoFe (reference layer ferromagnet, or reference layer FM). The stack is 2 μm long and 200 nm wide. The thickness of the BFO layer is chosen to be thinner than the actual thickness in the experiment (~100 nm) to save the computation time as we observed negligible changes when the thickness of BFO layer was varied from 30nm to 100nm as shown in **Figure 22**. Note that the BFO thin film has a stripe domain pattern with domain width of 200 nm as observed in the experiments [114]. Next, to compare against the GMR measurements [114], we sweep the external magnetic field from -300 Oe to 300 Oe with varying magnitude of J_{int}. The resistance of the spin-valve during the GMR measurement is determined by

$$R = R_0 + \Delta R sin^2 \frac{\theta}{2}, \tag{41}$$

where R_0 is the resistance of the ferromagnet sublattices, and θ is the angle between the magnetization of two CoFe layers. The GMR ratio is then calculated by

$$GMR = (R - R_P)/R_P = \Delta R sin^2(\theta/2)/R_0, \tag{42}$$

where R_P is the resistance when the bottom layer CoFe and the top layer CoFe are parallel. It is noticed that the curve of GMR ratio is highly dependent on the magnitude of J_{int} as shown in Figure 23. This is because when J_{int} increases, the magnetic coercive field (H_c) of the free layer FM increase due to the strong interface exchange coupling between BFO and free layer FM as seen in

Figure **24** (c), so the curve of GMR ratio is broadened. Similarly, when J_{int} is small, the free layer FM becomes decoupled from BFO; therefore, H_c decreases and the GMR curve becomes narrowly peaked. By varying the magnitude of J_{int}, we find that when J_{int} is equal to 0.32 pJ/m, our model fits well with the experimental data [114] without

considering any non-ideality effects such as nucleation of defects. Next, we also compare the curve of the GMR ratio when the aspect ratio of the BFO spin-valve structure changes from 100 to 2 in reference [114].

Figure **24** (b) presents results similar to the experimental results that the distance between the two peaks in the GMR curve decreases because of a smaller H_c in the reference layer FM. There is also no obvious exchange bias in the hysteresis loop of the free layer FM due to the larger width of the BFO, so the exchange bias of different domains will be compensated as seen in

Figure **24** (d). To validate the magnitude of J_{int} again, we simulate a stripe-domain 30 nm thick BFO and 2 nm thick CoFe bilayer thin films with 5 μm long and 2 μm wide similar to the experiment[53]. We sweep the external magnetic field from -300 to 300 Oe and check the M-H loop of the BFO/CoFe heterojunction.

Figure **24** (e) shows that our simulation results using J_{int}= 0.32 pJ/m are in a good agreement with the experimental data. This result further confirms the magnitude of J_{int} is 0.32 pJ/m when the mesh size is 20×20×2 nm^3.

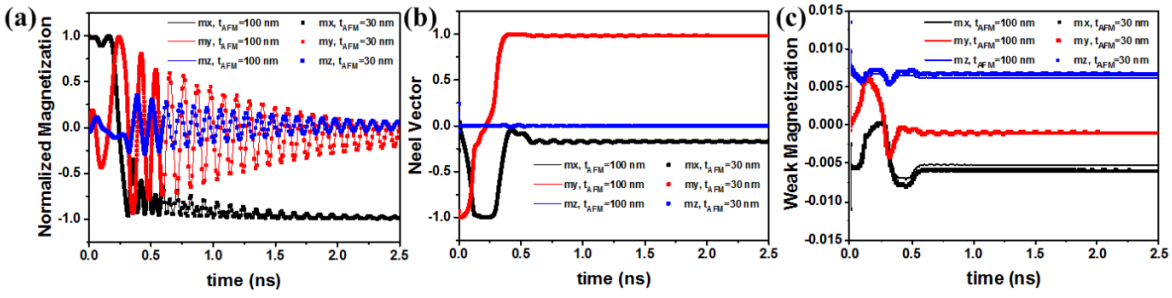

Figure 22 – Comparison of the switching dynamics of magnetization when the thickness of BFO is 100 nm versus 30 nm.

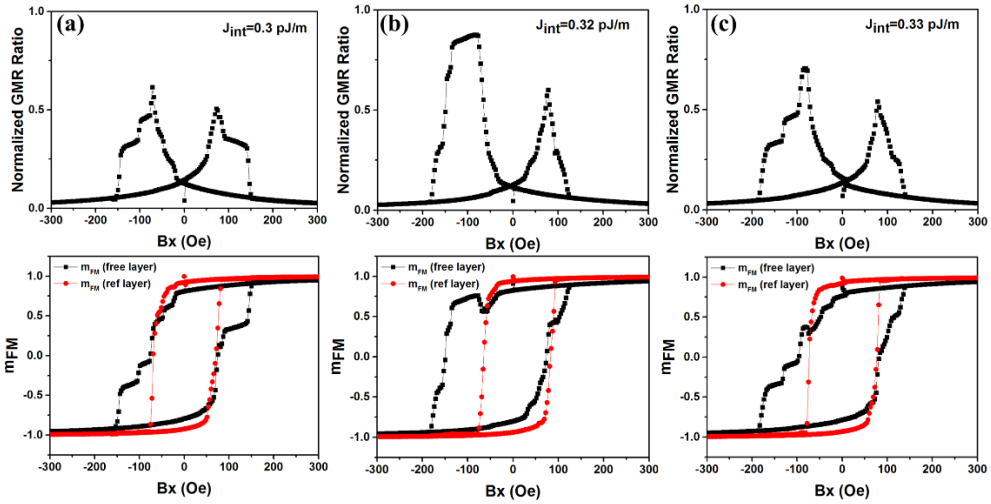

Figure 23 – The normalized GMR ratio and the magnetic hysteresis loop of the free layer and reference layer FM when (a) J_{int} = 0.3 pJ/m, (b) J_{int} = 0.32 pJ/m, and (c) J_{int} = 0.33 pJ/m.

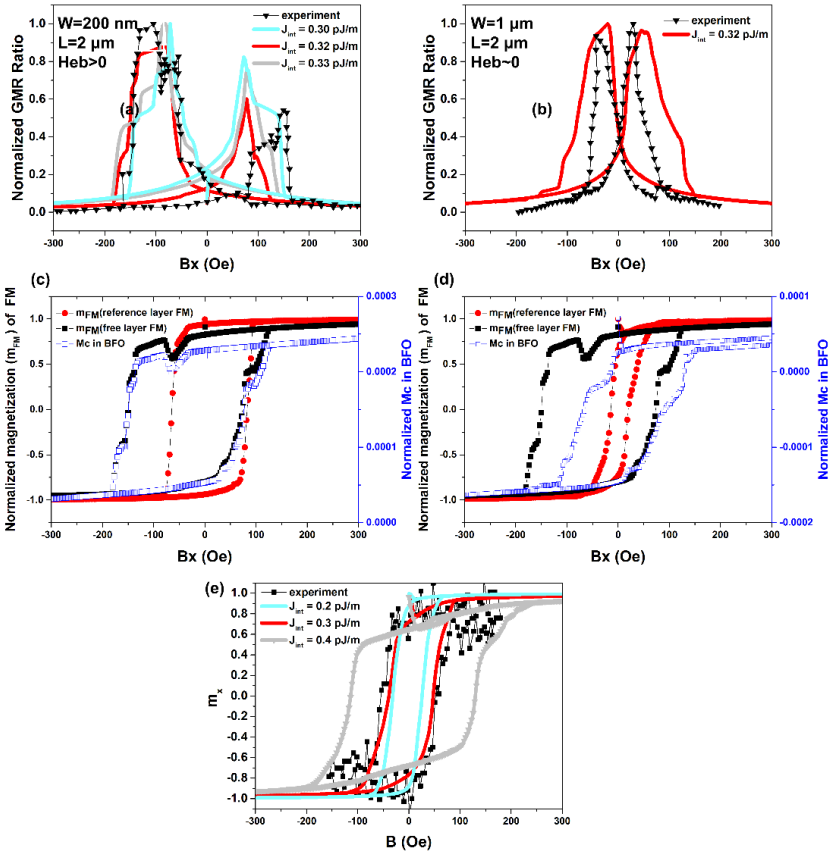

Figure 24 – Comparison between fitted GMR curve when (a) width = 200 nm, length = 2 μm and (b) width = 1 μm, length = 2 μm and experiment [114] for J_{int} extraction. The magnetic hysteresis loops of BFO, free layer ferromagnet, and reference layer ferromagnet when J_{int} = 0.32 pJ/m and width = 200 nm (c) or width = 1 μm (d). (e) Comparison between fitted magnetic hysteresis loop (M-H loop) and experiment [53].

1.10.1.3 Switching dynamics of BFO/CoFe bilayer thin film

Next, we investigate the dynamics of a 20 × 20 nm^2 single-domain 30 nm thick BFO and 2 nm thick CoFe bilayer. We renormalize the magnetic parameters of BFO and J_{int} with smaller mesh size 5×5×1 nm^3 to simulate a scaled device. The details of the renormalization approach are presented in **Appendix A**. Theoretically, the dynamics of CoFe is determined by the magnetization rotation in BFO because of the interface exchange coupling between $\boldsymbol{M_c}$ and $\boldsymbol{M_{FM}}$. To simulate the dynamics of both BFO and CoFe, we implement the model of a single-domain BFO from Section 3.1, in which the dynamics of $\boldsymbol{P}$, $\boldsymbol{N}$, and $\boldsymbol{M_c}$ are calculated by considering the rotation of the magnetic easy-plane along with the polarization [107]. Similar to the case of the single-domain BFO, we find that $\boldsymbol{N}$ switches 180^0 while $\boldsymbol{M_c}$ does not as shown in

Figure **25** (a). This means that the two sublattices $\boldsymbol{M_1}$ and $\boldsymbol{M_2}$ in BFO both switch 180° after the polarization switching as shown in **Figure 26**. In addition, the $\boldsymbol{M_{FM}}$ switches 180^0 after the polarization reversal, and there exists an intermediate stage when $\boldsymbol{M_{FM}}$ rotates 90^0 because of the two-step polarization switching [53] characteristics of BFO. This result is interesting since has been argued before that the magnetization reversal in CoFe mainly comes from the exchange coupling field between $\boldsymbol{M_c}$ and $\boldsymbol{M_{FM}}$ [51] However, as it

can be seen in our results, the main driving force is the rotation of $\boldsymbol{N}$ rather than the rotation of $\boldsymbol{M_c}$ since the magnitude of $\boldsymbol{M_c}$ is much smaller than $\boldsymbol{N}$. To verify the statement that the rotation of $\boldsymbol{N}$ governs the switching behavior of $\boldsymbol{M_{FM}}$, we consider two scenarios of the BFO switching: one is considering the rotating magnetic easy-plane perpendicular to $\boldsymbol{P}$, such that $\boldsymbol{N}$ switches 180^0 and $\boldsymbol{M_c}$ does not, and the other is fixing the magnetic easy-axis of BFO, then $\boldsymbol{N}$ remains unchanged but $\boldsymbol{M_c}$ switches 180^0.

Figure **25** (a) shows that when $\boldsymbol{N}$ switches 180^0, $\boldsymbol{M_{FM}}$ successfully rotate 180^0 after polarization reversal while $\boldsymbol{M_c}$ remains unswitched. On the contrary, when $\boldsymbol{N}$ is fixed during polarization reversal,

Figure **25** (b) shows that $\boldsymbol{M_c}$ switches but neither $\boldsymbol{M_{FM}}$ nor $\boldsymbol{N}$ switch. Therefore, we believe that the magnetic switching of $\boldsymbol{M_{FM}}$ is driven by the rotation of $\boldsymbol{N}$ rather than the reversal of $\boldsymbol{M_c}$.

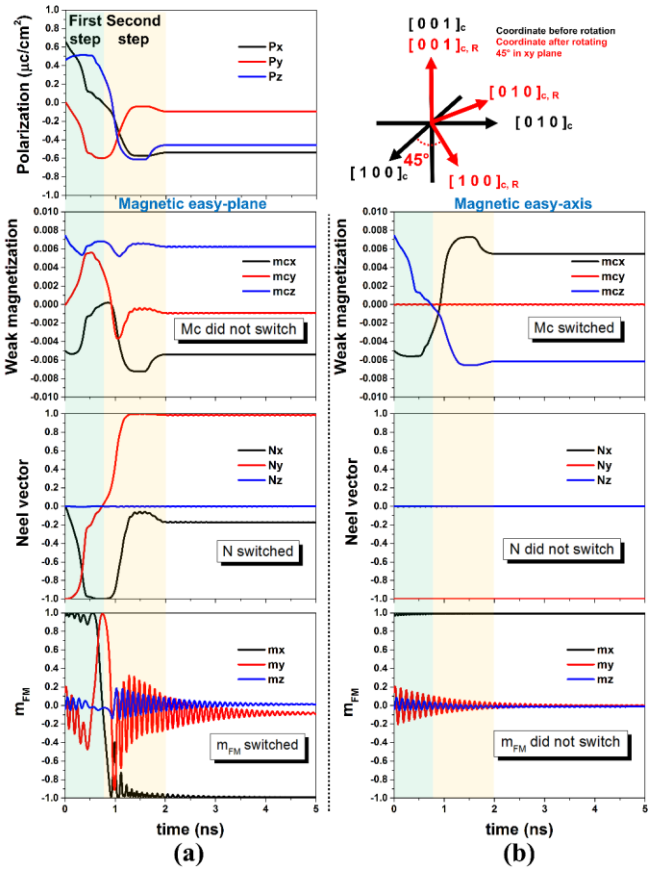

Figure 25 – The dynamics of the polarization (P), the weak magnetization (M_c), the Neel vector (N), and the magnetization of ferromagnet (CoFe) in the BFO/CoFe heterojunction when the magnetic state of BFO is easy-plane state (a) or easy-axis state (b).

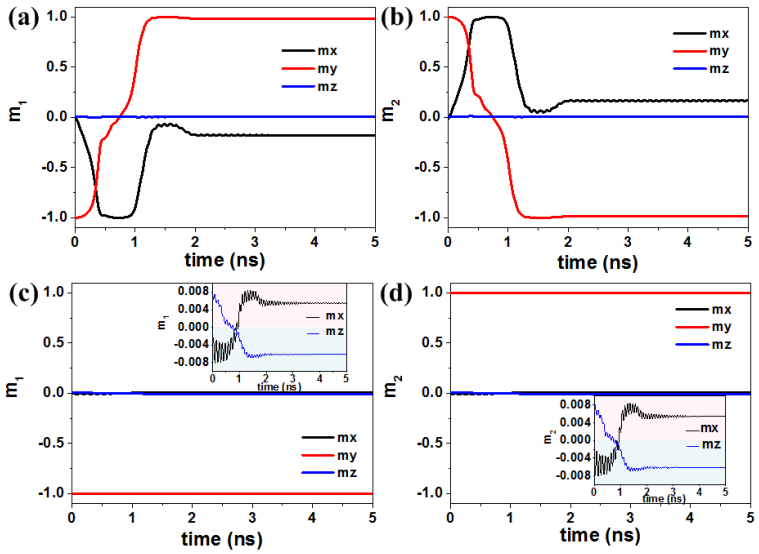

Figure 26 – The switching dynamics of magnetization of sublattice 1 (m_1=M_1/M_s) and sublattice 2 (m_2=M_2/M_s) in BFO during the polarization switching in the case of magnetic easy-plane (a-b) or magnetic easy-axis (c-d). The insets of (c) and (d) show that the *x* and *z* components of m_1 and m_2 switch 180° during polarization switching.

1.10.2 Sensitivity analysis and the switching time limit of the BFO/CoFe heterojunction

To evaluate the potential application of the BFO/CoFe heterojunction in logic/memory operations, we check the sensitivity of BFO polarization switching time (t_{FE}) that may affect the magnetization switching success rate and the magnetization switching time of CoFe. Note that varying t_{FE} of the BFO corresponds to various viscosity coefficients in the LK equation under a fixed electric field, and t_{FE} can be as fast as a few picoseconds as calculated from the theory [115] and projected from the experiment [116].

In Section 3.1, we have shown that the theoretical limit of the switching time of $\boldsymbol{N}$ in BFO is 30 ps. In other words, the antiferromagnetic order of BFO can follow the rotation of the polarization unless polarization switching time is below 30ps. For a BFO/CoFe

heterojunction with L = 40 nm, W = 20 nm, and 30 nm thick BFO and 2 nm thick CoFe, **Figure 27**(a) demonstrates that when t_{FE} is shorter than 1.45 ns, the rotation of $\boldsymbol{N}$ is too fast for $\boldsymbol{M_{FM}}$ to follow; thus, the switching of $\boldsymbol{M_{FM}}$ fails. This is because the switching time of $\boldsymbol{M_{FM}}$ follows the input switching time of $\boldsymbol{N}$; when t_{FE} is shorter than the inverse of the precession frequency of FM, the switching of $\boldsymbol{M_{FM}}$ fails. Similarly, when t_{FE} is larger than the minimum t_{FE} for successful magnet switching ($t_{FE,min}$), increasing t_{FE} increases the switching time of $\boldsymbol{N}$, $\boldsymbol{M_c}$ and thus $\boldsymbol{M_{FM}}$. Therefore, **Figure 27**(a) shows that the theoretical lower bound for $\boldsymbol{M_{FM}}$ switching is 1.45 ns when L = 40 nm, W = 20 nm, and CoFe is 2 nm thick. However, $t_{FE,min}$ of the BFO/CoFe heterojunction may not be a constant value since $t_{FE,min}$ depends on the strength of the interface exchange coupling between BFO and CoFe and the in-plane energy barrier of the device. Furthermore, if the in-plane energy barrier becomes larger than the interface exchange coupling energy, the switching of CoFe fails as shown in **Figure 27**(d). When the length of the 20 nm wide BFO/CoFe heterojunction increases from 40 nm to 45 or 50 nm, the switching of CoFe fails because the average interface exchange coupling field remains unchanged whereas the in-plane energy barrier increases as seen in **Figure 28**.

To examine dependency of the $t_{FE,min}$ on various energy barriers in the BFO/CoFe heterojunction or the strength of the interface exchange coupling in CoFe, we consider two scenarios: (A) varying the aspect ratio of the device and (B) varying the thickness of the CoFe layer under a fixed width (20 nm) of the BFO/CoFe heterojunction and a fixed thickness of BFO (30 nm). For case (A), **Figure 27**(b,c,e) show the relation between $t_{FE,min}$ and the varying aspect ratios of the BFO/CoFe bilayer. The minimum t_{FE} for successful magnet switching increases as the aspect ratio of the device increases because of the larger

energy barrier. In other words, the overdrive field for the CoFe layer decreases if the aspect ratio of the device is increased. However, $t_{FE,min}$ will become less dependent on the aspect ratio when the thickness of the CoFe decreases below 1 nm. This is because the interface exchange coupling field becomes dominant compared to the intrinsic exchange coupling field and the in-plane energy barrier in a thin CoFe layer. Therefore, for case (B), when the thickness of the CoFe is varied from 0.5 nm to 2 nm, $t_{FE,min}$ monotonically increases because of the weaker interface exchange coupling averaged in the CoFe, as shown in **Figure 27**(f). These time-dependent magnetization switching cases show that $t_{FE,min}$ in the BFO/CoFe heterojunction is 90 ps when the CoFe is as thin as 0.5 nm, and the magnitude of the average interface exchange coupling field decreases with increasing CoFe thickness as shown in **Figure 29**. To be more specific, when the thickness of CoFe increases from 1.5 nm to 2 nm, $t_{FE,min}$ drastically increases from 230 ps to 660 ps.

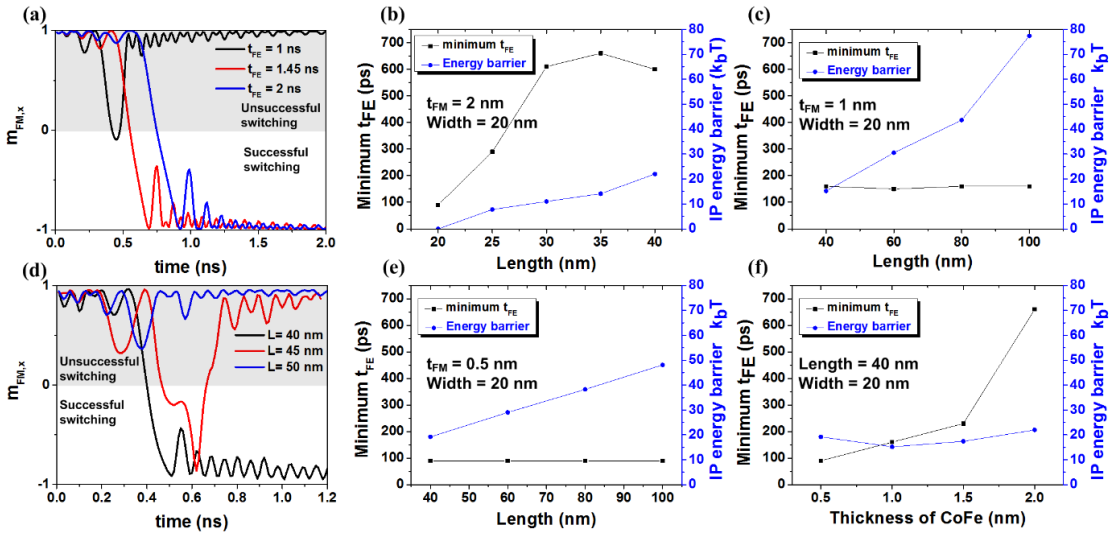

Figure 27 – (a) The minimum ferroelectric switching time (t_{FE}) for successful magnet switching in the BFO/CoFe heterojunction is 1.45 ns when L = 40 nm, W = 20 nm, and the thickness of BFO and CoFe are 30 nm and 2 nm, respectively. The minimum t_{FE}

of CoFe and the in-plane energy barrier of the BFO/CoFe heterojunction with varying lengths of the device when the thickness of CoFe is (b) 2nm, (c) 1 nm, and (e) 0.5 nm. (f) The minimum t_{FE} of CoFe and the in-plane energy barrier of the BFO/CoFe heterojunction with varying thicknesses of CoFe when length is 40 nm and width is 20 nm. (d) The magnetization switching of CoFe in the BFO/CoFe heterojunction fails under longer length (L >= 45 nm) when W = 20 nm.

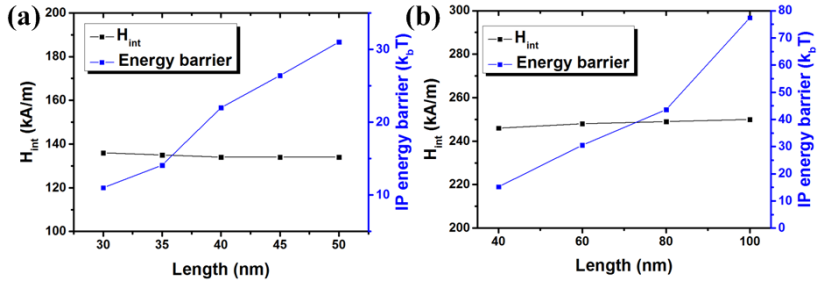

Figure 28 – The averaged interface exchange coupling field (H_{int}) and the in-plane (IP) energy barrier of the BFO/CoFe heterojunction under varying length when (a) W = 20 nm, t_{FM} = 2 nm (b) or W = 20nm, t_{FM} = 1 nm.

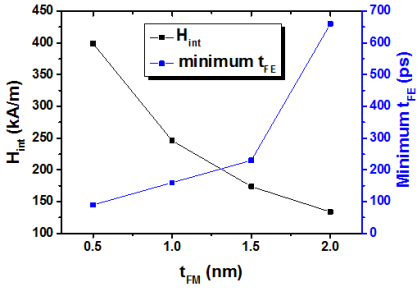

Figure 29 – The averaged interface exchange coupling field in FM and the minimum ferroelectric switching time (t_{FE}) under varying thickness of FM with L = 40 nm and W = 20 nm.

1.10.3 Thermal stability of the BFO/CoFe heterojunction

To study the thermal stability of the device, we check the magnetic energy barrier of the 20 nm wide single-domain BFO/CoFe thin film with varying device length and CoFe layer thickness. Since our calculations show that the out-of-plane (OOP) energy barrier is much larger than the in-plane (IP) energy barrier due to the strong shape anisotropy energy, we will only discuss the IP energy barrier in the following section. When the thickness of the CoFe layer is 2 nm, the IP energy barrier increases from 0 to 23 k_bT when the length increases from 20 nm to 40 nm, as shown in **Figure 27**(b). These energy barriers are too small for memory applications which usually require energy barriers larger than 60 or 70 k_bT for retention times larger than ten years. When the thickness of CoFe is 1 nm, the energy barrier of the BFO/CoFe bilayer is as large as 77.4 k_bT in the 100 nm long BFO/CoFe bilayer, as seen in **Figure 27**(c). However, when the thickness of CoFe is reduced to 0.5 nm in the 100 nm long BFO/CoFe bilayer, the IP energy barrier decreases to 48 k_bT because of the reduced volume of CoFe. Therefore, to ensure a high IP energy barrier, a 1 nm thick FM layer and a high length to width aspect ratio is suitable for the BFO/CoFe heterojunction.

To investigate the thermal stability and switching reliability of the device, we check the probability of successful switching in the BFO/CoFe heterojunction with varying aspect ratios and thicknesses of CoFe. The probability of successful switching (P_{sw}) is obtained by simulating the polarization and the magnetization switching dynamics of the BFO/CoFe heterojunction for 20 tests. Our results show that P_{sw} is only 50 % in the 20 tests when CoFe is 2 nm thick and L = 40 nm, However, for the case of 1 nm thick CoFe

with L = 100 nm, we observe that P_{sw} is 100% in these 20 tests because of the stronger interface exchange coupling effect between the BFO and thin CoFe layers.

From the above analysis of varying $t_{FE,min}$, IP energy barrier and P_{sw}, our results show that the thermal stability and the magnet switching time of the BFO/CoFe heterojunction depend on the proper design of the aspect ratio and the thickness of the CoFe layer. Generally, both a faster magnetization switching (smaller $t_{FE,min}$) and a high switching success rate are obtained from thinner CoFe films. On the other hand, when the aspect ratio is 5, the energy barrier will greatly decrease as the thickness of CoFe reduces from 1 nm to 0.5 nm since the energy barrier depends on the volume of the ferromagnet. Therefore, a BFO/CoFe heterojunction with a 1 nm thick CoFe and a high aspect ratio seems to be the most promising option in terms of thermally stability and error free operation.

1.11 Conclusion

In this chapter, we first analyzed the switching dynamics of a single-domain BFO thin film by solving LK and LLG equations, simultaneously. In comparison to the previous model of LG theory using the Neel vector as the order parameter, our model uses the magnetization as the order parameter and solves the LLG equations in two sublattices thus can model both the Neel vector and the weak magnetization accurately. Our results present that BFO as a G-type antiferromagnet has staggered spin vectors thus staggered DM vectors, which create a weak magnetization by tilting spin vectors unidirectionally. We also show the weak magnetism is strongly enhanced in a thin layer (2-3nm) near the surface of BFO because of the broken inversion symmetry. From the analysis of the energy

landscape, we demonstrate that the preferred-axis of the magnetic moment in BFO is determined by both the bulk DMI energy that couples to polarization, and the epitaxial strain that comes from the substrate. We then show for the first time that $\boldsymbol{N}$ rotates 180^0 while $\boldsymbol{M_c}$ remains unchanged by rotating polarization 180^0. This result is further verified by solving the effective equation of motion for the Neel vector in the LG theory. The driving force of the magnetic switching is due to the magnetoelectric coupling such that the easy-plane state and $\boldsymbol{H_{DMI}}$ rotate along with the polarization. By checking the sensitivity of parameters, we find that the probability of switching of $\boldsymbol{N}$ depends not only on the anisotropy energy barrier but also on the exchange coupling field in BFO. We further calculate the lower limit of the switching time of BFO to be around 30 ps assuming the polarization can be switched as fast. $\boldsymbol{N}$ cannot be switched if the polarization switches faster than 30 ps.

Next, we modelled the magnetic structure and the dynamics of a single domain $BiFeO_3$/CoFe heterojunction. To evaluate the interface properties and determine the value of $\boldsymbol{J_{int}}$, we model the experimentally measured magnetic hysteresis loop and GMR curve traces, and find that $\boldsymbol{J_{int}}$ is approximately 0.32 pJ/m. Using this experimentally extracted $\boldsymbol{J_{int}}$, we further simulate the dynamics of BFO/CoFe heterojunction and prove that the driving force of $\boldsymbol{M_{FM}}$ switching is determined by the rotation of $\boldsymbol{N}$ rather than the of $\boldsymbol{M_c}$ reversal. We also analyse the sensitivity of the switching success rate of the BFO/CoFe heterojunction with varying polarization switching time (t_{FE}). The minimum t_{FE} ($t_{FE,min}$) of a successful switching depends on the aspect ratio of the device and the thickness of the CoFe layer. It is found that a smaller $t_{FE,min}$ can be obtained by a thinner CoFe thin film. Last, we include the thermal noise effect of this BFO/CoFe heterojunction to evaluate the

thermal stability and the probability of successful switching for its application at room temperature. Our simulation results show that for a BFO/CoFe heterojunction with a thinner FM thin film (~1 nm), we can increase the aspect ratio to about 5 to ensure both high thermal stability and switching reliability (P_{sw}~100%). The results of this chapter are important for understanding and designing magnetoelectric devices.

MODELING MAGNETOELECTRIC DEVICE AND ITS APPLICATION

1.12 Modeling magnetoelectric device and its application

So far we have successfully modelled the dynamics of order parameters in the BFO/CoFe heterojunction after applying an electric field as discussed in Chapter 3. Since one can achieve a deterministic 180° magnetization switching at room temperature in BFO/CoFe heterojunction, it is considered promising to implement the BFO/CoFe heterojunction in the magnetoelectric magnetic random-access memory (ME-MRAM) [63] by combining with the MTJ. ME-MRAM is a voltage-controlled device which may have ultra-low write energy and fast write speed compared to other spintronic memory devices such as STT-MRAM and SOT-MRAM since it eliminates the joule heating energy and its write energy is dominated by the coercive voltage of the magnetoelectric material. Recently, experiments [117] have demonstrated that the coercive voltage of the La-doped BFO can be as low as 0.1V by tuning the doping concentration of La and reducing the thickness of the BFO layer which may further reduce the write energy of the ME-MRAM. However, modeling, design, and benchmarking for ME-MRAM is lacking. To conduct rigorous array level modeling, a fast and accurate compact model for BFO/CoFe heterojunction dynamics is needed.

To evaluate the potential of the BFO/CoFe device in the application of ME-MRAM, in this chapter, we first build a compact model of the BFO/CoFe heterojunction based on the experimentally calibrated physical model we have developed in Chapter 3. To the best

of our knowledge, this is the first compact model developed for an antiferromagnet/ferromagnet heterojunction. In addition, our compact model incorporates the magnetoelectric effect by combining the ferroelectric and the magnetic models for the BFO and CoFe layers. Compared to the previous studies which utilize the single-domain or macro-spin approximation for the free layer magnet of the MTJ, our compact model features two sublattices for both the antiferromagnetic and ferromagnetic layers. Therefore, our compact model can capture the exchange coupling field within the antiferromagnetic or ferromagnetic layers, and the interface exchange coupling field between these two layers. With such a model, the dynamics of the order parameters in the antiferromagnet can also be calculated.

1.12.1 Compact model of the magnetoelectric device

In Chapter 3, we have combined the ferroelectric model and the micromagnetic simulations and solve the dynamics of the polarization ($\boldsymbol{P}$), Neel vector ($\boldsymbol{N}$), and weak canted magnetization ($\boldsymbol{M_c}$) in the BFO and the magnetization in CoFe layer ($\boldsymbol{m_{FM}}$). To enable the circuit level simulation of the ME-MRAM, in this section we build a physics-based compact model that can simulate the dynamics of order parameters in the BFO/CoFe heterojunction.

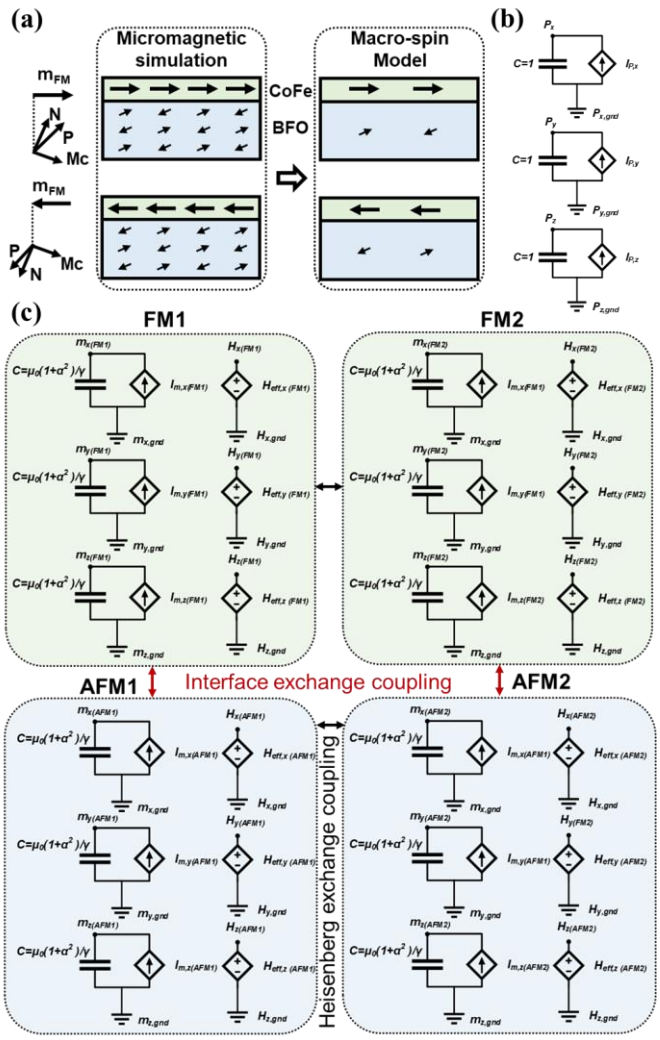

Figure 30 – (a) Schematics of the change of order parameters in the BFO/CoFe heterojunction. In the micromagnetic simulation, there are multiple cells and the interaction between the cells are accounted for. For the macro-spin model, the BFO and CoFe layers are each represented by two cells. (b) Equivalent SPICE model of the LK equation for BFO. (c) Equivalent SPICE model of the LLG equations for BFO and CoFe layers.

1.12.1.1 Ferroelectric model of the BFO layer[1]

[1] The model in this subsection is developed by Chia-Sheng Hsu.

For the ferroelectricity of BFO, the polarization dynamics is solved by the three-dimensional time-dependent Landau-Khalatnikov (LK) equation:

$$\frac{dP_x}{dt} = -L\left[\frac{\partial(f_L+f_{elas}+f_{ep})}{\partial P_x} - (sign)E_{dw}\right], \tag{43}$$

$$\frac{dP_y}{dt} = -L\left[\frac{\partial(f_L+f_{elas}+f_{ep})}{\partial P_y}\right], \tag{44}$$

$$\frac{dP_z}{dt} = -L\left[\frac{\partial(f_L+f_{elas}+f_{ep})}{\partial P_z} - E_z + 2KP_z\right], \tag{45}$$

where $\boldsymbol{P_x}$, $\boldsymbol{P_y}$, and $\boldsymbol{P_z}$ are the components of $\boldsymbol{P}$, L is the domain kinetic coefficient, and K is the depolarization factor defined in eq. (6) in [118]. The electric energy contribution is incorporated as the electric field inside the film. $\boldsymbol{E_z}$ is the externally applied field in the out-of-plane direction and $\boldsymbol{E_{dw}}$ is the domain wall induced internal field, which accounts for the in-plane polarization switching with plus-minus signs for two different domain configurations. The other empirical ferroelectric energy components of BFO include the Landau bulk free energy (f_L), elastic free energy (f_{elas}), and easy-plane strain energy (f_{ep}) which are given as [53], [101], [119]

$$\begin{aligned} f_L(\vec{P}) = \alpha_1\left(P_x^2 + \eta_1 P_y^2 + \eta_1 P_z^2\right) + \alpha_{11}\left(P_x^4 + \eta_{11} P_y^4 + \eta_{11} P_z^4\right) + \\ \alpha_{12}\left(P_x^2 P_y^2 + P_y^2 P_z^2 + P_x^2 P_z^2\right) + \alpha_{111}\left(P_x^6 + P_y^6 + P_z^6\right) + \alpha_{112}[P_x^4\left(P_y^2 + \right. \\ \left. P_z^2\right) + P_y^4(P_x^2 + P_z^2) + P_z^4\left(P_x^2 + P_y^2\right)] + \alpha_{123}\left(P_x^2 + P_y^2 + P_z^2\right), \end{aligned} \tag{46}$$

$$f_{elas}(\vec{P}) = \frac{1}{2}c_{11}(e_{11}^2 + e_{22}^2 + e_{33}^2) + c_{12}(e_{11}e_{22} + e_{11}e_{33} + e_{22}e_{33}) + 2c_{44}(e_{13}^2 + e_{23}^2 + e_{12}^2), \tag{47}$$

$$f_{ep}(\vec{P}) = K_s(P \cdot u)^2 = K_s(\frac{1}{\sqrt{2}}P_y + \frac{1}{\sqrt{2}}P_z)^2, \tag{48}$$

where $e_{ij} = \epsilon_{ij} - \epsilon_{ij}^0$,

$$\epsilon_{11}^0 = Q_{11}P_x^2 + Q_{12}\left(P_y^2 + P_z^2\right), \epsilon_{13}^0 = Q_{44}P_xP_z$$
$$\epsilon_{22}^0 = Q_{11}P_y^2 + Q_{12}(P_x^2 + P_z^2), \epsilon_{23}^0 = Q_{44}P_yP_z$$
$$\epsilon_{33}^0 = Q_{11}P_z^2 + Q_{12}\left(P_x^2 + P_y^2\right), \epsilon_{12}^0 = Q_{44}P_xP_y$$

$$\epsilon_{11} = \epsilon_{22} = \mu_m,\ \epsilon_{11} = 0,$$

$$e_{13} = e_{23} = 0, e_{33} = -c_{12}(e_{11} + e_{22})/c_{11},$$

and α_1, α_{11}, α_{12}, α_{111}, α_{112}, α_{123} are the dielectric stiffnesses and higher order stiffness under stress-free condition, η_1 and η_{11} are scaling factors of the bulk free energy, e_{ij} is the elastic strain, ϵ_{ij} is the strain state of the crystal compared to the parent paraelectric phase, ϵ_{ij}^0 is the stress-free strain, c_{ij} is the elastic stiffness tensor, Q_{ij} is electrostrictive coefficient, and μ_m is the strain that comes from the lattice mismatch between BFO and the substrate. K_s in f_{ep} is the easy-plane strain coefficient and $\boldsymbol{u}$ = $(0,\frac{1}{\sqrt{2}},\frac{1}{\sqrt{2}})$ is the unit normal to the easy-plane. Note that eq (43-45) are in the form of $C\frac{dV(t)}{dt} = I(t)$, therefore, the SPICE equivalent LK equation can be expressed analogously, as show in **Figure 30**(b).

1.12.1.2 Antiferromagnetic/ferromagnetic model of the BFO/CoFe layers

The magnetization dynamics of the magnetic cell *i* can be solved by the Landau–Lifshitz–Gilbert (LLG) equation which is given by

$$\frac{d\vec{\boldsymbol{m}}_i}{dt} = -\frac{\gamma}{1+\alpha^2}\left(\vec{\boldsymbol{m}}_i \times \vec{\boldsymbol{H}}_{eff}\right) - \frac{\alpha\gamma}{1+\alpha^2}\left[\vec{\boldsymbol{m}}_i \times \left(\vec{\boldsymbol{m}}_i \times \vec{\boldsymbol{H}}_{eff}\right)\right]. \quad (49)$$

Previous studies [120] have simulated the magnetization dynamics of the ferromagnetic layer in SPICE. The SPICE equivalent LLG equation can be expressed as

$$\frac{\mu_0(1+\alpha^2)}{\gamma}\frac{d\boldsymbol{m_x}}{dt} = F\left(\boldsymbol{m_x}, \boldsymbol{m_y}, \boldsymbol{m_z}, \boldsymbol{H_{eff,x}}, \boldsymbol{H_{eff,y}}, \boldsymbol{H_{eff,z}}\right), \quad (50)$$

	$\frac{\mu_0(1+\alpha^2)}{\gamma}\frac{d\boldsymbol{m_y}}{dt} = G\left(\boldsymbol{m_x}, \boldsymbol{m_y}, \boldsymbol{m_z}, \boldsymbol{H_{eff,x}}, \boldsymbol{H_{eff,y}}, \boldsymbol{H_{eff,z}}\right),$	(51)
	$\frac{\mu_0(1+\alpha^2)}{\gamma}\frac{d\boldsymbol{m_z}}{dt} = H\left(\boldsymbol{m_x}, \boldsymbol{m_y}, \boldsymbol{m_z}, \boldsymbol{H_{eff,x}}, \boldsymbol{H_{eff,y}}, \boldsymbol{H_{eff,z}}\right).$	(52)

The above equations are again in the form of $C\frac{dV(t)}{dt} = I(t)$. The SPICE equivalent model of the LLG equations for the BFO and CoFe layers are shown in **Figure 30**(c). The micromagnetic simulations are also implemented in SPICE in the dimensions to model the magnetization dynamics accurately [121]. However, to simulate the magnetization dynamics of the BFO/CoFe heterojunction, a three-dimensional model is essential to account for the interface effect between BFO and CoFe layers. Also, the computation time becomes $O(n^3)$ when we implement the micromagnetic simulations of the BFO/CoFe device in SPICE. To facilitate the modeling of the switching dynamics of the BFO/CoFe heterojunction, the BFO and CoFe cells are represented by two sublattices in our compact model as shown in **Figure 30**(a). The polarity of the exchange coupling field between the two sublattices then determines the antiferromagnetic or ferromagnetic coupling inside BFO and CoFe layers, respectively.

Compared to the micromagnetic simulations, our macro-spin model simplifies the exchange coupling energy and the demagnetization energy within the cells. The demagnetization field acting on the magnetic cells is usually expressed as

$$\vec{H}_{demag,i} = -\sum_j N_{i-j} M_s \vec{m}_j, \quad (53)$$

where N_{i-j} is the demagnetization tensor in cell i due to cell j, and $\vec{m}_j$ is the normalized magnetization of cell j. The demagnetization tensor $N = \begin{bmatrix} N_{xx} & N_{xy} & N_{xz} \\ N_{xy} & N_{yy} & N_{yz} \\ N_{xz} & N_{yz} & N_{zz} \end{bmatrix}$ is calculated based on the distance between cells i and j. Since we are considering only two sublattices for either BFO or CoFe in our compact model, the demagnetization tensor is calculated by the simplified model [122] which varies as the size of the BFO and CoFe layers change.

The exchange coupling field is normally expressed as $\vec{H}_{exch,i} = \frac{2A}{\mu_0 M_s} \nabla^2 \vec{m}$ in the micromagnetic simulations where A is the exchange coupling coefficient. To maintain the exchange coupling energy densities corresponding to BFO, CoFe, and their interface within the compact model, the coupling coefficient between the two sublattices in BFO (J_{AFM}), CoFe (J_{FM}) or between BFO and CoFe (J_{int}) need to be renormalized such that $E_i/V = \sum_{j \in N_i} A_{ij} \frac{\boldsymbol{m_i} \cdot (\boldsymbol{m_i} - \boldsymbol{m_j})}{\Delta_{ij}^2} / V$ remain the same. By calculating the exchange energy in BFO and CoFe for various lengths and widths, we find that $-J_{AFM} \approx 2.97 \times 10^{-11} l^2 + 3.88 \times 10^{-10}\ J/m$ and $J_{FM} \approx (l/5 \times 10^{-9})^2 J/m$ where l is the length of the BFO/CoFe bilayers. Note that the renormalized J_{AFM} and J_{FM} are independent of the width and thickness of the BFO and CoFe layers since each layer is represented by only two cells. Similarly, the interface exchange coupling coefficient $J_{int} \approx 0.3\ pJ/m$ when the mesh size in the thickness (z) direction is fixed at 1nm.

The switching paths of the order parameters in BFO and CoFe calculated by the macro-spin simulations in SPICE are plotted in **Figure 31** and are compared with those obtained by micromagnetic simulations. It can be seen that the compact model accurately

describes the dynamics of Neel vector in the BFO layer and the magnetic order in the CoFe layer **Figure 31**(a) and (b). Note that the compact model cannot accurately capture the dynamics of $\boldsymbol{M_c}$ (**Figure 31**(c)). This is because $\boldsymbol{M_c}$ is defined as the summation of two anti-parallel vectors $\boldsymbol{M_1}$ and $\boldsymbol{M_2}$, therefore, a small deviation on either $\boldsymbol{M_1}$ or $\boldsymbol{M_2}$ causes large deviations on the magnitude of $\boldsymbol{M_c}$. However, as shown in Section 3.2.1, the dynamics of $\boldsymbol{m_{FM}}$ is dominated by the rotation of $\boldsymbol{N}$ rather than the rotation of $\boldsymbol{M_c}$, therefore, the inaccuracy in $\boldsymbol{M_c}$ would not affect the accuracy of the compact model.

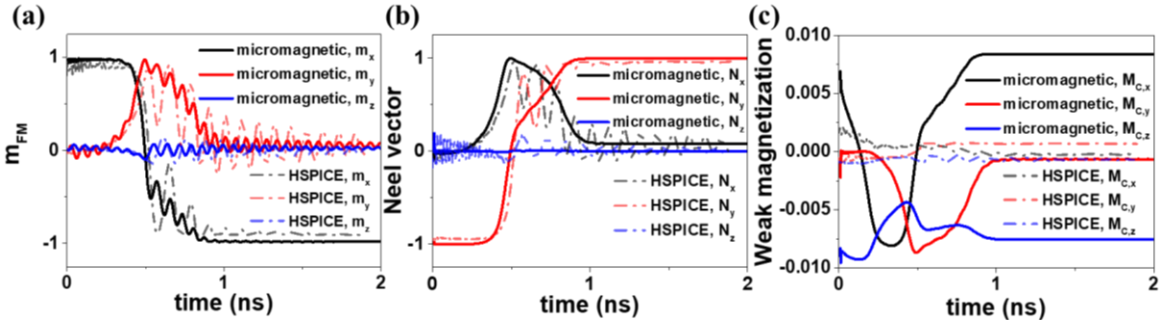

Figure 31 – Comparison of the magnetization dynamics of ferromagnet ($\boldsymbol{m_{FM}}$), dynamics of the Neel vector, and weak magnetization of antiferromagnet layer in SPICE (dashed lines) and micromagnetic simulations (solid lines).

1.13 Write and Read Performances of ME-MRAM using the $BiFeO_3$/CoFe Heterojunction

1.13.1 Memory cell design of ME-MRAM

The ME-MRAM made up of the BFO/CoFe heterojunction may have ultra-low write energy depending on the coercive voltage of the BFO layer. The coercive voltage (V_C) of the BFO depends on the thickness of the BFO layer and the doping concentration

of La [117]. **Figure 32** shows the layout and schematics of ME-MRAM using one select transistor (1T1MTJ) or two select transistors (2T1MTJ). When the V_C of the BFO is smaller than 0.3V, two transistors are needed to separate the read and write operation. If V_C of the BFO is larger than 0.3V, then one access transistor is used to further reduce the layout area. Note that the ferromagnetic layer needs to be long enough to act as a contact for the source line (SL).

To simulate the read and write performances of the ME-MRAM under varying V_C, we use HPSICE and the compact model we developed for the BFO/CoFe heterojunction, and the 16nm Predictive Technology Model (PTM) [74] for CMOS transistors. We consider the ME-MRAM in a 256×128 bits array and include the parasitic capacitances and resistances from the interconnects, transistors, the BFO capacitors, and the peripheral circuits which are referred to [68]. The read operation of the ME-MRAM is referred to the tunneling magnetoresistance (TMR) effect. The resistance area (RA) product of the MTJ under varying oxide thickness is obtained by the experimental results [35].

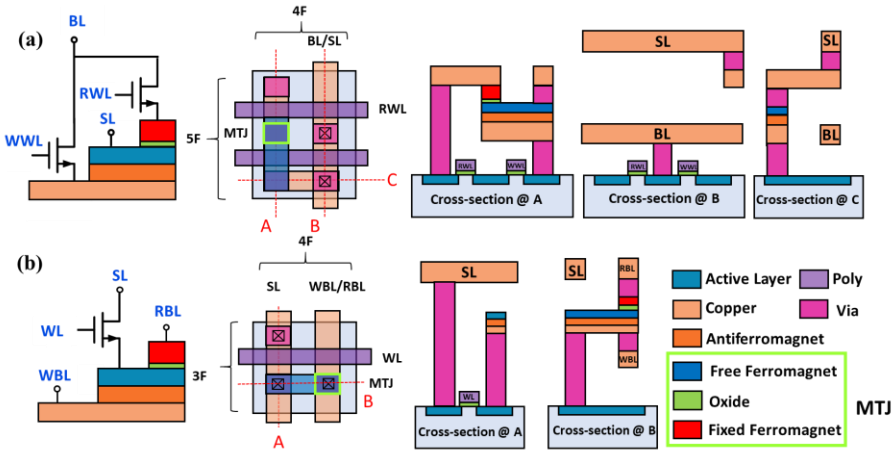

Figure 32 – Schematics and layout of the ME-MRAM using (a) two transistor scheme when coercive voltage (V_C) <0.3V or (b) one transistor scheme when V_C >0.3V.

1.13.2 2T1MTJ (V_c<0.3V)

The read and write circuits of the two transistors are shown in **Figure 33**(a). The write driver circuits supply write voltages to either bit line (BL) or source line (SL) during the write operation to write '0' and '1' states. The read circuit, we adopt the circuit similar to the STT-MRAM [79]. Before the read operation, the clock signal is on to ensure the voltages on BL+ and BL- are pre-charged to the same level. During the read operation, we apply a charge current flowing through the MTJ. The read current flowing through the ME-MTJ cell is then compared to the reference MTJ. The output voltages (V_{out+}, V_{out-}) from the read circuit are connected to the comparator and then latch-up to the final output signal 0 or 1.

The simulated waveforms of the ME-MRAM during read and write operations considering V_C = 0.2V and V_{write} = 0.3V are shown in **Figure 33** (b). The pulse width for the read and write operations are 5ns. During the read operation, the gate of the read word

line (RWL) turns on, the output voltage (V_{out} =V_{out+} - V_{out-}) changes its polarity when $\boldsymbol{m_{FM}}$ switches from +x to -x. The read delay time ~ 0.22 ns and the read energy ~ 2.79 fJ where most of the read energy is dissipated in the form of Joule heating due to the current flowing through the MTJ, BL and SL. During the write operation, as the voltage drop (V_{FE} - V_{FM}) across the BFO layer is larger than V_C, the polarization switching happens and the magnetization of FM also switches. The write energy of the 2T1MTJ scheme when the array size is 256×128 is ~7 fJ per cell which is dominated by the write driver circuits and the dynamic energy to charge BL or SL.

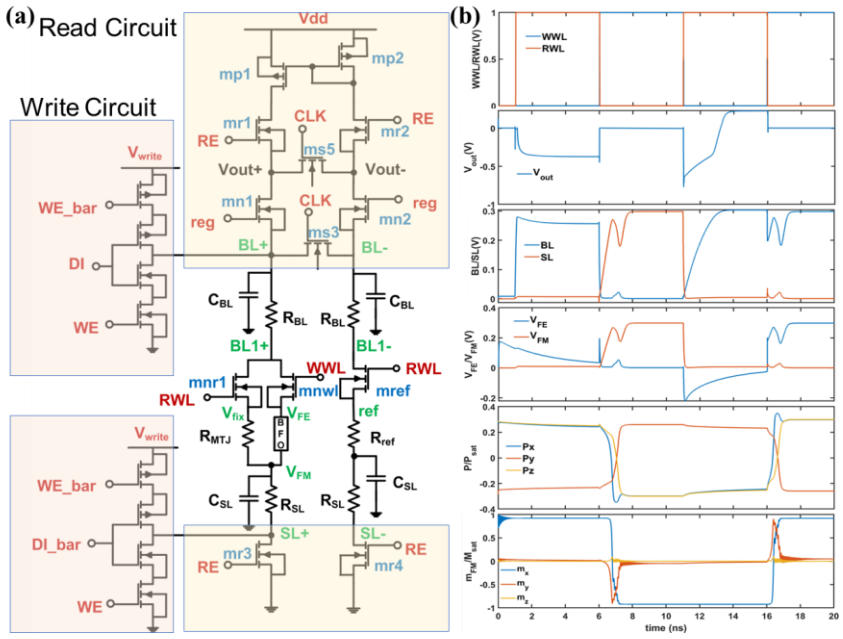

Figure 33 – (a) The read and write circuits of the ME-MRAM using 2T1MTJ. (b) The simulated waveform of the ME-MRAM using 2T1MTJ during read (1-6ns) and write (6-11ns) operations.

1.13.3 1T1MTJ (V_c>0.3V)

When the coercive voltage of the BFO layer is larger than 0.3V, 1T1MTJ scheme is used and the read and write circuits are shown in **Figure 34**(a). The read operation of the 1T1MTJ scheme is similar to the case of 2T1MTJ scheme except that during the write operation, there is a shunt current flowing through the MTJ and thus the static leakage current increases. **Figure 34**(b) shows the simulated waveform of the ME-MRAM when the thickness of the BFO layer is 30nm and V_C = 0.3V. Note that there is a voltage drop of ~0.27V across the BFO layer during the read operation due to the read current flowing through the MTJ. However, since V_C of the BFO layer >0.3V, no read disturb problem happens. During the write operation, a larger V_{write} = 0.5V is applied to switch the polarization of the BFO. Using the one transistor 1T1MTJ scheme, the read delay time and energy are similar to the 2T1MTJ scheme since they use the same read circuits as seen in **Figure 35**(b). For the write performance, the write energy ~41 fJ where most of the energy is due to the leakage current passing through the MTJ.

To summarize, the 1T1MTJ scheme has the advantage of being smaller in cell area (~$12F^2$ versus $20F^2$) but it suffers from a larger write energy compared to the 2T1MTJ scheme. The write and read energy for both schemes and two coercive voltages are plotted versus array size in **Figure 35**. Note that the write energy for the 1T1MTJ is almost constant (~35fJ) even for small arrays because the write energy is dominated by the static leakage current. Whereas for the 2T1MTJ scheme, the write energy decreases as the array

size decreases since parasitic capacitance on the BL and the corresponding dynamic energy dissipation decrease.

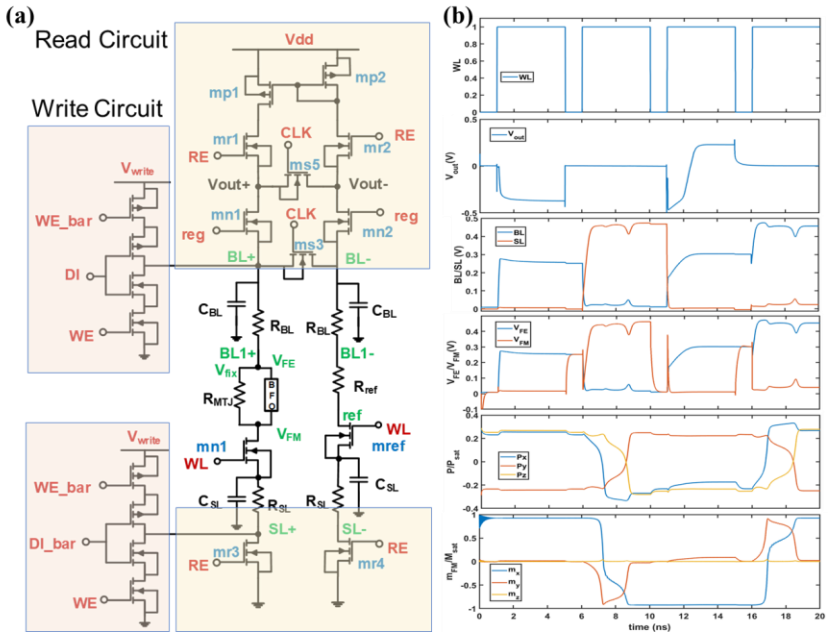

Figure 34 – (a) The read and write circuits of the ME-MRAM using 1T1MTJ scheme. Both read and write operations share the same access transistor. (b) The simulated waveform of the ME-MRAM using one transistor scheme during read (1-5ns) and write (6-11ns) operations.

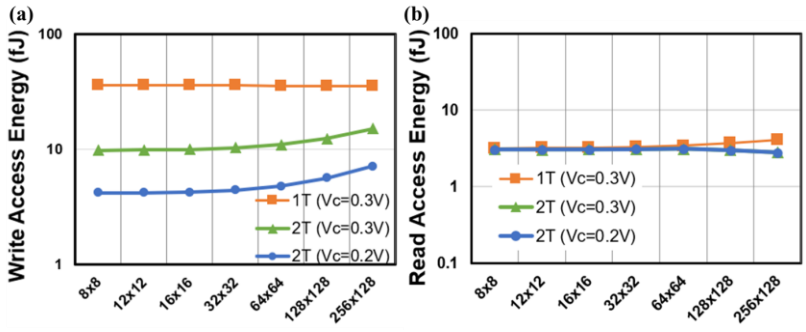

Figure 35 – Comparison of the (a) write and (b) read performances of the ME-MRAM using 1T1MTJ or 2T1MTJ schemes under varying array size.

1.13.4 Ultra-low Coercive Voltage of BFO (V_C ~ 20mV)

To further decrease the energy dissipation, researchers aim to achieve ever smaller coercive fields. The potential energy savings offered by such devices at the array level; however, are not clear as the gates of CMOS transistors must still need to be driven by substantially larger voltages. Using such sensitive devices may also pose other challenges for the circuit designers such as read disturb or vulnerability to crosstalk and other kinds of noise. To answer these questions, in this section we consider V_C = 20 mV of the BFO layer by reducing the ferroelectric energy barrier of the BFO with the scaling factors η_1 and η_{11} in the bulk free energy. The tuned Landau coefficients as shown in **Table 7**.

The 2T1MTJ scheme is used to separate the read and write paths for BFO with ultra-low coercive voltage. Since the write voltage becomes 20mV, we use NMOS only for the write driver circuit such that V_{write} supplies BL or SL whenever write enable (WE) signal is on as shown in **Figure 36**(a). Next, the simulated waveform during the read and write operation is shown in **Figure 36**(b). For the selected cell (row=4, column=6), we see that the read and write operation are successful. However, there are voltage overshoot/undershoot~50mV that happens when either write or read access transistor turns on. The voltage overshoot comes from the capacitive couplings between gate and source/drain (C_{GS} and C_{GD}). When the overshoot voltage is higher than V_C of the BFO as seen from **Figure 36**(c), both read and write disturb problems happen for the neighboring cells that is on the selected row but unselected column (row = 4, column = 5). Note that this kind of voltage overshoot also happens for the ME-MRAM with V_C >0.1V, however, the magnitude of V_C is much larger than the overshoot voltages such that there is no read or write disturb instances. To suppress the voltage overshoot that comes from these

capacitive couplings, one should choose the access transistors with minimum sizes (fin number = 1) or smaller parasitic capacitances. **Figure 36**(d) shows that when we change the fin number from 2 to 1 or changing the access transistor from 16nm to 7nm node, no read or write disturb incidences exist. Next, the read energy is ~1fJ and write energy is ~0.45 fJ considering a 8×8 bits array. Compared to the case when V_C = 0.2V using the 2T1MTJ scheme, the BFO with ultra-low coercive voltage (V_C = 0.02V) can significantly reduce the write energy from 2.2 fJ to 0.45 fJ. However, using low write voltages also means that the read and write circuits are going to be quite sensitive to the noise and the voltage overshoot/undershoot, and the write energy does not decrease quadratically since the write energy becomes dominated by the write driver rather than the dynamic energy to charge BL or SL.

Table 7 – Parameters used for the BFO layers under varying coercive voltage

V_C (V)	t_{BFO} (nm)	Saturation polarization (P_{sat})	α_1	α_{11}
0.02	10	0.07	$4.9\times(T-1103K)\times10^5\times0.07$	70.3×10^8
0.2	10	0.5	$4.9\times(T-1103K)\times10^5\times0.2$	2.3×10^8
0.3	30	0.5	$4.9\times(T-1103K)\times10^5\times0.2$	2.3×10^8

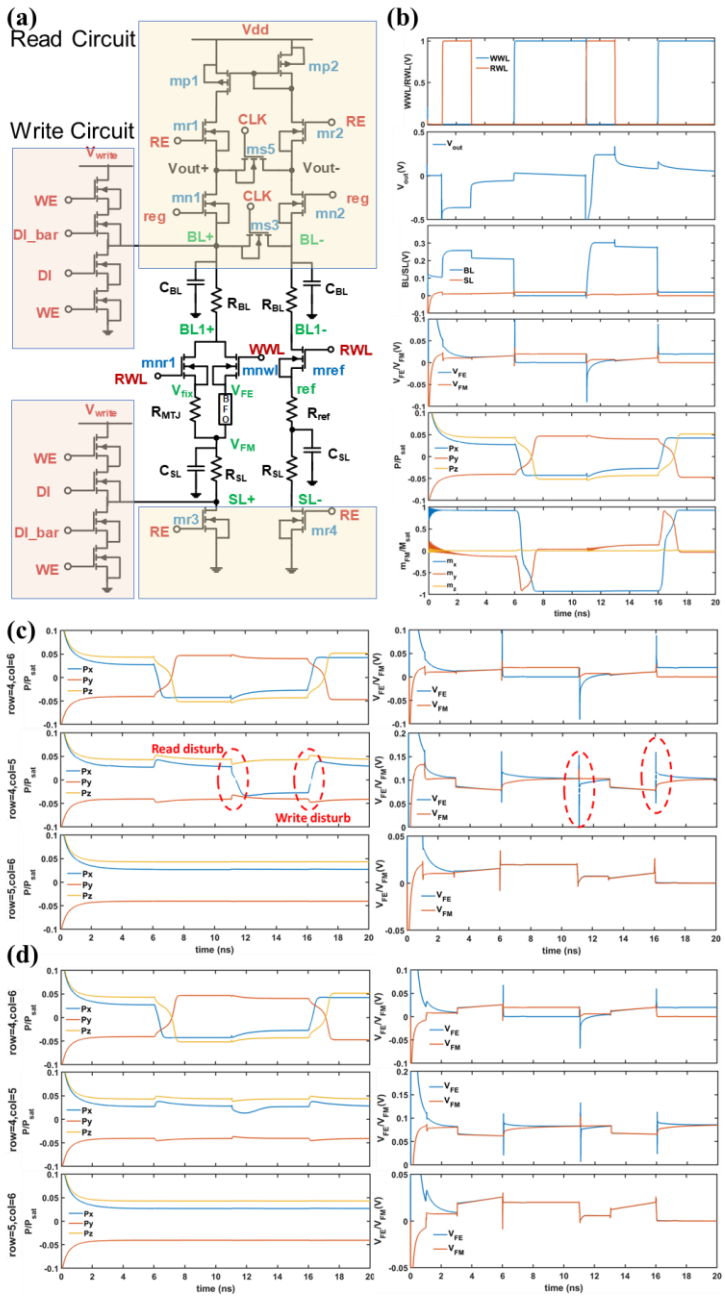

Figure 36 – (a) The read and write circuits of the ME-MRAM with ultra-low coercive voltage of BFO. The write driver circuits are composed of NMOS only due to the low write voltages. (b) The simulated waveform of the ME-MRAM during read (1-2ns) and write (6-11ns) operations. (c) The read and write disturb check for the selected cell (row = 4, col = 6) and neighboring cells (row = 4, col = 5 and row = 5, col = 6). The

read/write disturb happens when there is a voltage overshoot/undershoot in V_{FE}. (d) The read and write disturb check for the selected cell (row = 4, col = 6) and neighboring cells (row = 4, col = 5 and row = 5, col = 6) when using transistor in the 7nm technology node.

1.14 Benchmarking for the write operation

To evaluate the write performance of ME-MRAM compared to other spintronic memory devices for possible use in the embedded memory application, we plot the write energy versus delay for the SRAM, ME-MRAM, STT-MRAM, and SOT-MRAM in **Figure 37**. The datapoints for the SRAM, STT-MRAM, and SOT-MRAM are obtained from Chapters 2 and 5. **Figure 37** shows that ME-MRAM can potentially have even lower write energy than SRAM and all the other spintronic memory devices. For the write delay time, ME-MRAM shows similar delay time as SOT-MRAM. Therefore, ME-MRAM which is a voltage-controlled nonvolatile device is useful in the low power application. We also observe that when V_C=0.3V, using the 2T1MTJ scheme shows lower write energy but larger cell layout area compared to the case of 1T1MTJ scheme. Reducing the coercive voltage of the BFO layer can further decrease the write energy of the ME-MRAM. While ME-MRAM looks most promising compared to other spintronic device candidates, the current challenges of the ME-MRAM are the rather immature technology, compatibility to the current process, and the reliability issues. Moreover, if the leakage current through the ferroelectric layer (BFO) is high, it will degrade the voltage drop across the ferroelectric layer, a higher write voltage is needed and the power dissipation will increase. Therefore, further studies and research are essential for realizing such a low-power device in the near future.

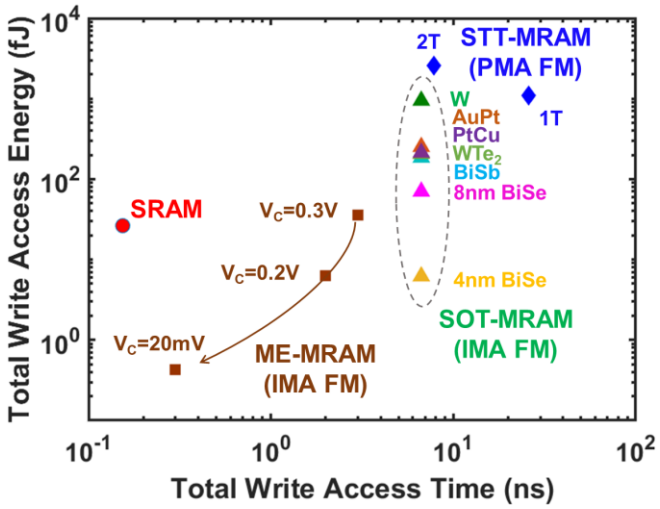

Figure 37 – The array-level write performances of SRAM, STT-MRAM using one or two access transistors, SOT-MRAM using various channel materials (W, AuPt, PtCu, WTe_2, BiSb, 4nm BiSe, and 8nm BiSe), and ME-MRAM with various coercive voltages (V_C=20mV, 0.2V, 0.3V) of BFO.

1.15 Conclusion

In this chapter a physics-based compact model of the magnetoelectric device made up of the BFO/CoFe heterojunction is presented. For the ferroelectric switching of BFO, our model captures the two-step polarization switching as observed in the experiment. For the magnetization switching in BFO and CoFe layers, our macro-spin model closely matches the simulation results from the micromagnetic simulations while taking much shorter computation time. Next, we use our compact model of the BFO/CoFe heterojunction to quantify the potential performance of ME-MRAM at the array level. Depending on the coercive voltages of the BFO layer, we can adopt one transistor (1T1MTJ) scheme when V_C >0.3 V or two transistors (2T1MTJ) scheme for other cases. By evaluating the read and write performances of ME-MRAM, our results show that the

write energy can be as low as a few fJ when using the 2T1MTJ scheme. However, the write energy increases to a few tens of fJ when using 1T1MTJ scheme due to the leakage current flowing through the MTJ. If we further scale down the coercive voltage of BFO to sub-100mV range, the write energy is further reduced but the cells become highly sensitive to the voltage overshoot/undershoot when the transistors turn on. Last, our benchmarking results show that ME-MRAM has the lowest write energy compared to SRAM and all other spintronic memory devices. Thereby, ME-MRAM is a promising option for the low power memory applications.

MODELING AND BENCHMARKING OF SPIN-ORBIT TORQUE MAGNETORESTRICTIVE RANDOM-ACCESS MEMORY[2]

1.16 Overview of spin-orbit torque magnetorestrictive random-access memory (SOT-MRAM)

Spin-orbit torque (SOT) MRAM with an inherently high charge-to-spin conversion efficiency is potentially far more energy efficient compared to spin-transfer-torque (STT) MRAM. From the material perspective, various SOT materials such as heavy metals [80], alloys [75], [123], semi-metals [76], and topological insulators [78], [124] offer vastly different values for anti-damping torque efficiency (ξ_{DL}) and SOT channel conductivity (σ_{SOT}). In some cases, σ_{SOT} and ξ_{DL} are strong functions of the SOT layer thickness which makes a fair and simple comparison of the results from different experiments/materials more challenging. For the structures of the SOT-MRAM, there are four types of structures including *Z* type, *Y* type, *X* type, and *XY* type depending on the direction of the magnetic easy-axis and the applied current direction as shown in **Figure 38**. For the *Y* type SOT-MRAM, the charge current flowing through the *x* direction would generate spin current with the polarization in the *y* direction, therefore one can deterministically switch the magnetization of the in-plane FM with easy-axis in the *y* direction. However, for the *X* type SOT-MRAM, the charge current flowing in the *x* direction cannot deterministically switch the in-plane FM with easy-axis in the *x* direction, thus an external magnetic field in the *z* direction is needed. Alternatively, one can use the *XY* type SOT-MRAM such that the tilting of the easy-axis of the in-plane FM from the *x* and *y* axis enable a deterministic

[2] This work is done in collaboration with Piyush Kumar.

switching of the FM. For the *Z* type SOT-MRAM, the magnetic easy-axis is in the out-of-plane (*z*) direction, and the current flowing through the *x* direction can only generate spin current with the polarization in the *y* direction. Therefore, an external magnetic field along the *x* direction is needed to deterministically switch this PMA FM. Since the *Z* type SOT-MRAM has the benefits of small cell layout area, it is considered more promising compared to other types of SOT-MRAM for the memory application as device scaling down. However, as device scaling, the required external magnetic field increases, and the power dissipation greatly increases. Therefore, in addition to applying an external magnetic field, spin-transfer- and spin-orbit toques can be combined to achieve efficient switching the PMA FM. Alternatively, materials with low crystalline symmetry may provide a path to generate out-of-plane anti-damping torque [125] to switch PMA FM. Besides, important effects such as current crowding at nanoscale and Joule heating have been mostly ignored for the SOT-MRAM, and the choice of SOT material can greatly affect the read performance of SOT-MRAM in addition to the write operation which has been mostly overlooked so far.

To address all these gaps and guide material development, we develop a comprehensive modeling framework for array-level read and write performance. We will discuss the write performances of SOT-MRAM as functions of two major material parameters: σ_{SOT} and ξ_{DL} and the read performances that includes the process and device variations. To address the variation in SOT channel thickness in various experiments, 4nm equivalent σ_{SOT} and ξ_{DL} are defined (**Figure 39**) which allow simple comparison of SOT materials regardless of their thickness as listed in **Table 8**. We show simple models that have been widely used [126] to calculate current shunting between SOT and FM layers can

result in up to 10 times underestimation of the generated spin torque when nanoscale magnets are used. For the first time, we also show that a very efficient SOT material may result in a high read disturb rate. The results provide important guidelines regarding the material development for SOT-MRAM devices.

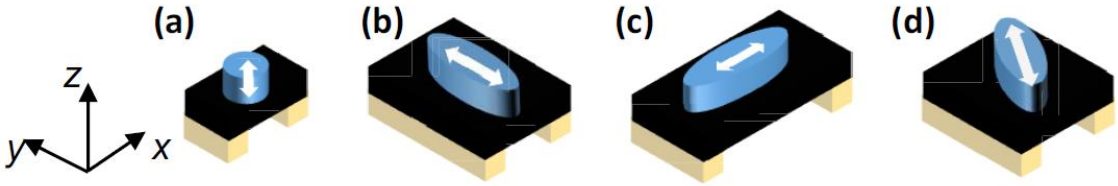

Figure 38 – Four types of structure of the SOT-MRAM including (a) *Z* type with an out-of-plane easy-axis, (b) *Y* type with an in-plane easy-axis in the y direction, (c) *X* type with an in-plane easy-axis in the x direction, and (d) *XY* type with an in-plane easy-axis tilted from the *x* and *y* axis. [127] Reprinted from "Roadmap of Spin–Orbit Torques," Q. Shao et al., IEEE Trans. Magn., vol. 57, no. 7, pp. 1–39, Jul. 2021. Copyright 2021 IEEE.

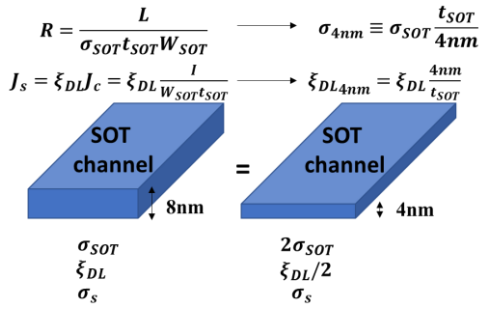

Figure 39 – The equivalent 4nm model of the conductivity ($\sigma_{4\,nm}$) and spin Hall angle ($\xi_{DL,4\,nm}$) of SOT channel under varying thickness. As an example, when the SOT channel is 8 nm thick, the equivalent 4 nm conductivity ($\sigma_{4\,nm}$) will be two times larger to achieve the same resistance. The equivalent 4 nm spin Hall angle ($\xi_{DL,4\,nm}$) will be

half of ξ_{DL} because current density is artificially doubled when thickness is assumed to be 4nm.

Table 8 – Measured data and the equivalent 4nm model for various SOT materials under varying thickness.

	t_{SOT} (nm)	DLT ratio (ξ_{DL})	DLT ratio ($\xi_{DL,4nm}$)	σ_{SOT} ($\Omega^{-1}\cdot m^{-1}$)	$\sigma_{SOT,4nm}$ ($\Omega^{-1}\cdot m^{-1}$)	σ_s	Ref.
W	4	-0.2+-0.03	-0.2+-0.03	3.85×10^5	3.85×10^5	7.7×10^4	[80]
$Au_{0.75}Pt_{0.25}$	4	0.35	0.35	1.2×10^6	1.2×10^6	4.22×10^5	[75]
$Pt_{0.57}Cu_{0.43}$	5	0.44	0.352	1.21×10^6	1.52×10^6	5.33×10^5	[123]
WTe_2	5	0.43	0.341	6.21×10^5	7.76×10^5	2.65×10^5	[76]
	4	18.62	18.62	7.8×10^3	7.8×10^3	1.45×10^5	
Bi_xSe_{1-x}	8	2.88	1.44	4.65×10^4	9.29×10^4	1.34×10^5	[78]
	16	1.5	0.39	6.13×10^4	2.45×10^5	9.56×10^4	
$Bi_{1-x}Sb_x$	4	0.65	0.65	1.7×10^5	1.7×10^5	1.11×10^5	[124]

1.17 Device-level modeling

We consider three options of SOT-MRAM including: 1) SOT-switched in-plane (IMA) FM, or called the *Y* type SOT-MRAM, 2) SOT-switched PMA FM (*Z* type SOT-MRAM) with STT assist, 3) SOT-switched PMA FM (*Z* type SOT-MRAM) with OOP spin Hall angle ($\xi_{DL,z}$) as shown in **Figure 40**. Both SOT-switched IMA FM and STT-assisted SOT-switched PMA FM show larger layout area compared to SOT-switched PMA FM with OOP spin Hall angle. This is because the IMA FM needs higher aspect ratio in length/width to maintain sufficient energy barrier. The SOT-switched PMA FM needs separated active region to turn on the read and the write access transistors simultaneously during the write operation.

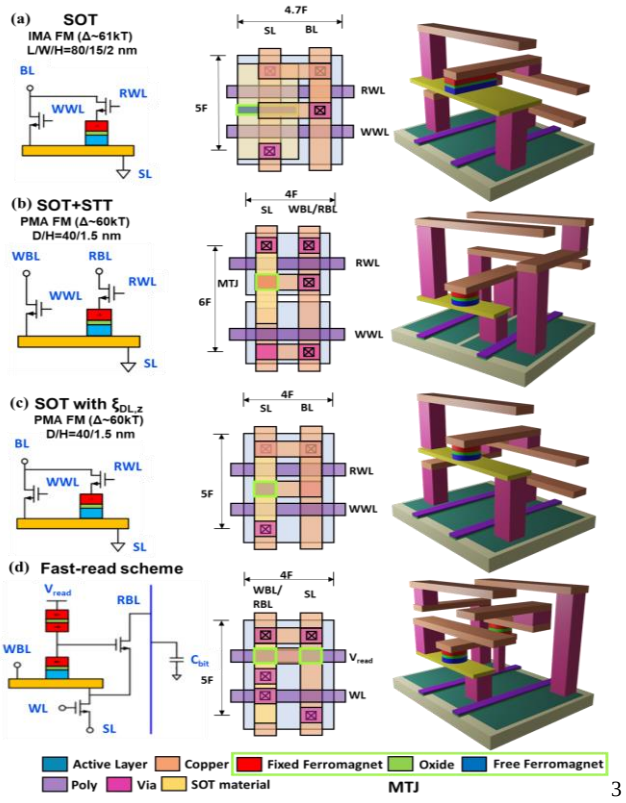

[3]

Figure 40 – Schematics and layouts of SOT-MRAM with (a) in-plane ferromagnets, (b) ferromagnets with perpendicular magnetic anisotropy (PMA) combining with STT, and (c) PMA FM with $\xi_{DL,z}$, (d) PMA FM with $\xi_{DL,z}$ with fast-read scheme. Here F = 30nm is the half-metal pitch.

1.17.1 Write operation

1.17.1.1 Current shunting effect

During the write operation, the write access transistor turns on, and the charge current flows through the SOT channel thus generating spin current flowing in the OOP direction. The vector of the spin polarization is orthogonal to the vectors of charge current

[3] Figure curtesy of Piyush Kumar for the 3D structure.

and the spin current. When the resistivity of the SOT channel is comparable to the FM, the current shunting effect happens, and the efficiency of the SOT degrades. To accurately estimate the current distribution in SOT channel and FM, we use COMSOL [128] simulations rather than the commonly used lumped model (**Figure 41**(a))[4]. We observe that the current shunting is not as severe as predicted with the lumped model, especially at the two ends of the channel underneath the magnet as shown in **Figure 41**(b). We further compare the average charge current (I_c), by integrating the current distribution from the COMSOL simulations, divided by the average I_c calculated by the lumped model. **Figure 41**(c) shows that the lumped model works well when σ_{SOT} is high, but the ratio can be large as 80 when σ_{SOT} is as low as 10^3 ($\Omega^{-1}m^{-1}$).

1.17.1.2 Micromagnetic simulations

Next, we perform micromagnetic simulations by OOMMF [89] to account for the domain nucleation and domain wall propagation during magnet switching. In OOMMF, the magnetization dynamics are calculated by the stochastic LLG equations for each cell. The thermal noise effects during magnet switching cause sharper probability density function when I_s is large. Here we consider magnet switching time of $\mu+5\sigma$ to achieve a write error rate of less than 10^{-6}. Also, large current densities in the SOT channel can cause significant Joule heating especially for high resistivity SOT materials. As temperature increases, the critical current for magnet switching decreases but the thermal noise increases. We use COMSOL to calculate the temperature evolution during switching for

[4] The COMSOL simulations were set up, run, and analyzed by Piyush Kumar.

varying SOT resistivities[5]. Our simulations reproduce experiential results [129] once the Joule heating effect is accounted for.

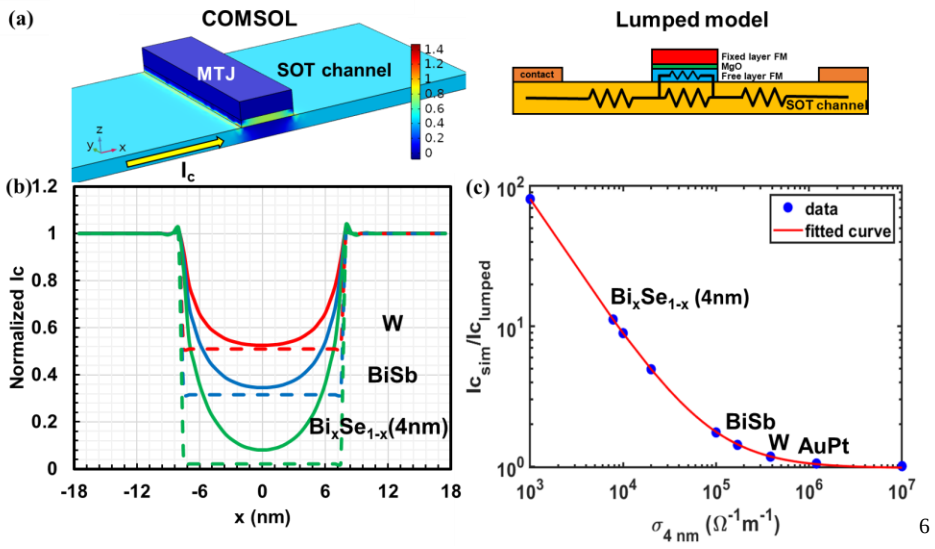

6

Figure 41 – (a) Schematics of the current shunting effects simulated in COMSOL and the simple lumped circuit model. (b)The normalized charge current flowing through the SOT channel versus position for W (red), BiSb (blue), and Bi_xSe_{1-x} (green). The solid (dashed) lines refer to the COMOSL simulations (lumped model). (c) The average charge current flowing through the SOT channel normalized to the results from the lumped model versus 4nm equivalent conductivity. The red line is the fitted curve using power series.

1.17.2 Read operation

1.17.2.1 Read disturb

[5] These COMSOL simulations were also conducted by Piyush Kumar.
[6] Figure curtesy of Piyush Kumar.

During the read operation, the current flowing through the SOT channel generates spin currents that may flip the magnetization state if it is large as shown in **Figure 42**(a). This read disturb issue will be less pronounced in resistive SOT channels, as currents tend to crowd towards the edge of MTJ thus contributing little to the spin current generation. We use COMSOL simulations to account for the current crowding effect. When σ_{SOT} is low, the current crowding at the edge of the FM/SOT channel interface is stronger; therefore, a smaller I_s is generated, and the RDR may be lower as seen in **Figure 42**(b). The spin current generated during read operation for an in-plane MTJ is plotted in **Figure 43**.

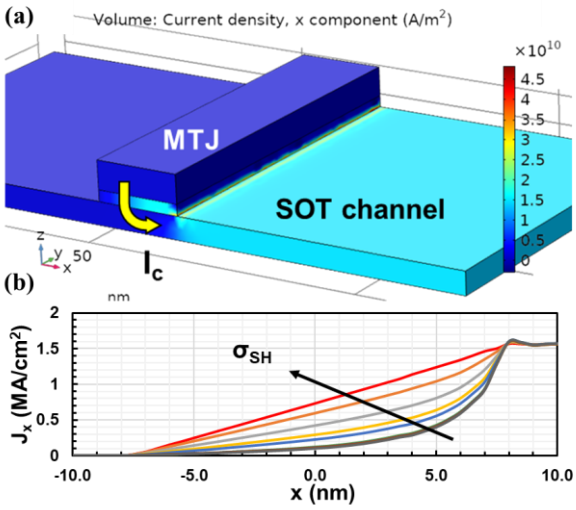

Figure 42 – (a) Current crowding during read operation. (b)The distribution of current density flowing through the SOT channel under constant read current (I_{read} = 5μA)[7].

[7] Figure curtesy of Piyush Kumar.

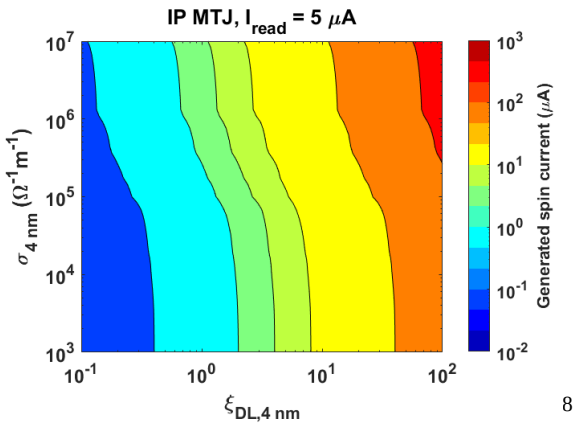

[8]

Figure 43 – Spin current generated during the read operation under constant read current (I_{read} = 5 μA) with varying spin Hall angles (ξ_{DL}) and channel conductivities (σ_{SOT}) of SOT materials.

1.17.2.2 Monte Carlo simulations

The read delay and the read energy are simulated using HSPICE with the read circuit adapted from [79]. To simulate the process and device variations that affect the read margin and the read error rate (RER) of the SOT-MRAM, we consider 10% variation for V_{dd} and the temperature, 3σ/μ <=5% for the critical dimension of the MTJ, 3σ/μ<=6% for the MgO layer thickness (t_{ox}) of the MTJ, and σ <=11% for the angle between free layer and reference layer FM due to thermal noise effect. The relation between the resistance-area product (RA) of the MTJ and t_{ox} is extracted from [35], and the degradation of the TMR ratio under higher temperature is obtained from [130]. The read delay time (t_{read}) is then calculated as μ+5σ to achieve RER<10^{-6} after running the Monte Carlo simulations.

1.18 Array-level performances

[8] [8] Figure curtesy of Piyush Kumar.

We then consider the write and read performances of SOT-MRAM in a 256×128 bit array with the parasitic resistances and capacitances calculated by the cell layout as shown in **Figure 40**.

1.18.1 Write performance

1.18.1.1 SOT-MRAM with in-plane ferromagnets

To compare the array-level write energy (E_{write}) of SOT-MRAM under varying σ_{SOT} and ξ_{DL} of the SOT channel, we fix I_s flowing through the 2 nm thick CoFe layer as shown in **Figure 44**(a). It is seen that E_{write} decreases under larger σ_{SOT} and ξ_{DL}, but the improvement of the E_{write} becomes almost independent of σ_{SOT} when σ_{SOT} >10^6 ($\Omega^{-1}m^{-1}$). This is because the current shunting effect is negligible when σ_{SOT} is comparable or larger than that of σ_{CoFe}. When σ_{SOT} is smaller than σ_{CoFe}, the contours of the write energy in **Figure 44**(a) correspond to $\sigma_{SOT}^{0.65}\xi_{DL}$, which means that while both σ_{SOT} and ξ_{DL} are important, one should put more emphasis on ξ_{DL} in the search for better SOT materials. Also, the spin Hall conductivity (σ_S), which is the product of σ_{SOT} and ξ_{DL}, might be an oversimplified optimization parameter for SOT materials. Next, we benchmark the performances of various existing SOT materials with possibly different thicknesses by using their 4nm equivalent σ_{SOT} and ξ_{DL} values on the 2D color coded plot in **Figure 44**(a). **Figure 44**(a) further shows that the 4nm thick Bi_xSe_{1-x} thin film has the lowest E_{write} compared to other candidates due to the high $\xi_{DL,4nm}$. Also, we calculate the temperature in the SOT and ferromagnetic layers due to the joule heating effect and plot the contours when T=425K and T=600K as shown in **Figure 44**(a). The high heating temperature pose challenges on the thermal stability of the FM and the compatibility of the backend process

of the Si technology. Therefore, having an SOT material with high σ_{SOT} and ξ_{DL} is critical since it not only reduces the write current but also reduces the heating problem as device scales down.

1.18.1.2 STT-assisted SOT-MRAM with PMA ferromagnets

For the SOT-MRAM with PMA FM, **Figure 44** (c,d) show the ratio of the write energy using the STT-assisted SOT-MRAM to that of the STT-MRAM. We apply $I_{s,SOT}$ = 640μA at the SOT channel for 1 ns, and pass $I_{c,STT}$ = 15μA through the MTJ for 12 ns for the STT-assisted SOT-MRAM. For the case of STT-MRAM, $I_{c,STT}$ = 40 μA is applied. It is seen that the write energy of STT-assisted SOT-MRAM can be 70% lower compared to STT-MRAM when PtCu, AuPt, and Bi_xSe_{1-x} are used as SOT channel materials. Better SOT materials can further lower the write energy. However, there is a diminishing return once $\xi_{DL,4\ nm}$>10 and $\sigma_{4\ nm}$>10^5 $\Omega^{-1}m^{-1}$ since the write energy becomes dominated by the STT component. The high write current in the SOT channel can cause a severe Joule heating and the temperature in the FM can rise to 425K or even larger when $\sigma_{4\ nm}$ and $\xi_{DL,4\ nm}$ are not large enough as seen in **Figure 44**(c,d).

1.18.1.3 SOT-MRAM using low crystalline symmetry materials with PMA ferromagnet

New SOT materials with low symmetry that generate both $\xi_{DL,y}$ and $\xi_{DL,z}$ can lift the necessity of STT current or external magnetic field for PMA FM switching [131]. From our micromagnetic simulations[9], $\xi_{DL,z}/\xi_{DL,y}$ needs to be larger than 0.16 to ensure reliable magnet switching. This is because $I_{sy,SOT}$ helps the magnetization reversal by pushing it

[9] Simulations are conducted by Piuysh Kumar.

towards the *y* direction (in-plane) and reducing the incubation time for magnet switching. However, when $I_{sy,SOT}$ is too large, the in-plane component of the magnetic order stays large while current is flowing and the thermal noise may push the magnet to the wrong direction once the current is turned off. **Figure 44** (b) shows that the write energy is determined by $\xi_{DL,z}$ rather than $\xi_{DL,y}$. The write energy of the SOT-MRAM can become comparable to that of SRAM if one can achieve $\xi_{DL,z} > 0.3$.

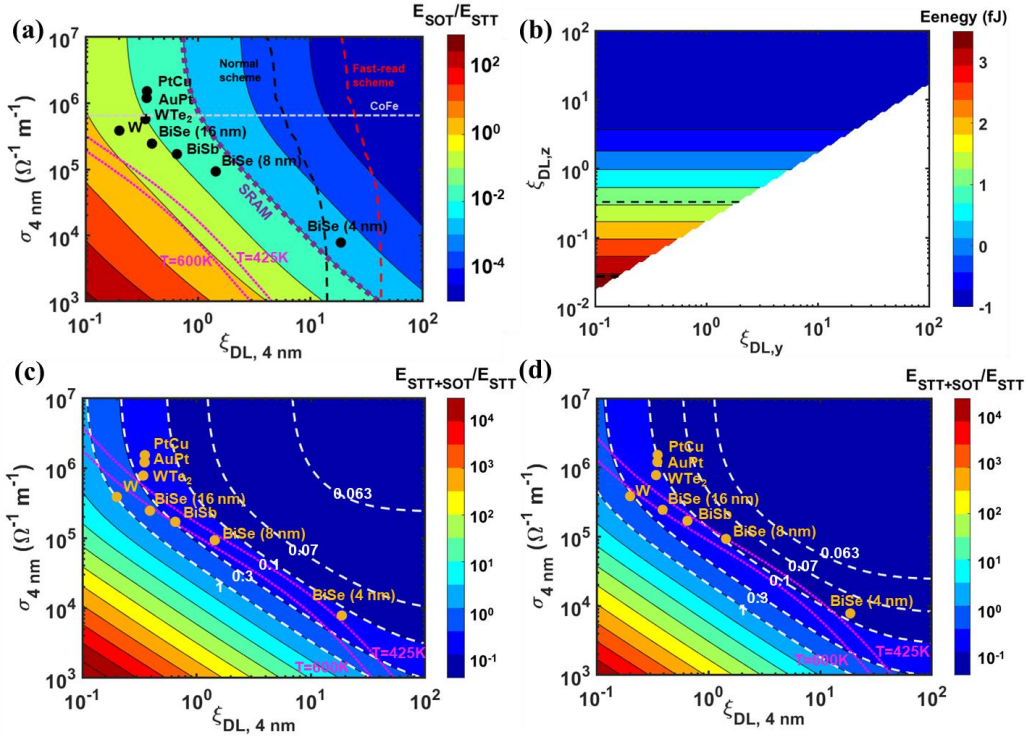

Figure 44 – (a)The switching probability of PMA FM with varying $\xi_{DL,z}$ under fixed $\xi_{DL,y}$ or varying $\xi_{DL,y}$ under fixed $\xi_{DL,z}$. (b)The write energy of SOT-MRAM with in-plane ($\xi_{DL,y}$) and out-of-plane ($\xi_{DL,z}$) spin Hall angles.

1.18.2 Read performance

1.18.2.1 Read performances of SOT-MRAM using various SOT materials

The read delay time (t_{read}) of SOT-MRAM for various SOT materials is shown in **Figure 45** (a). It is seen that SOT materials with small σ_{SOT} such as 8 nm thick Bi_xSe_{1-x} thin film will have longer t_{read} because of the larger channel resistance in series with MTJ. To further reduce the t_{read} and the read disturb rate, we adopt the fast-read scheme in [69]. In this scheme, the read current flows through the read access transistor with the gate voltage controlled by the voltage division between the reference MTJ (the upper MTJ in **Figure 40** (d) where the magnetization of both free and reference layer FM are fixed) and the cell MTJ (the lower MTJ in **Figure 40** (d)). Therefore, the read current is more sensitive to the resistance change from the cell MTJ compared to the normal read scheme. In addition, the read current only flows through the read and the write access transistors such that a resistive SOT channel does not significantly degrade the on/off ratio of the cell. **Figure 45** (c) shows that t_{read} becomes sub-nanosecond, and the read energy (E_{read}) is also reduced compared to the normal read scheme.

The design space of the SOT-MRAM with the read disturb rate=10^{-6} is shown as a black dashed line in **Figure 44** (a). This boundary is calculated when an IMA FM is used, the read current = 5μA, and the spin current is obtained from the COMSOL simulation as seen in **Figure 43**. It is seen that the design space to prevent the read disturb problem can become larger when using the fast-read scheme (**Figure 40** (d)) due to the separated current paths for the MTJ and bitline (BL) discharge and the higher on/off ratio for the resistance of the cell MTJ compared to the SOT channel.

1.18.2.2 Sensitivity analysis of the read operation

The variation in the read time can be caused by the variability in supply voltage (V_{dd}), MTJ resistance, TMR ratio, and the thermal noise effect. The MTJ resistance depends on t_{ox}, the area of the MTJ, and the angle between the magnetization of the free layer and the reference layer FM (θ). To evaluate the critical parameters that may affect the read performance of the SOT-MRAM, we do the Monte Carlo simulations on each parameter and calculate the mean values of the total read energy and delay time as shown in **Figure 45**(b). The results show that the read energy and delay are dominated by the MTJ resistance which is affected by θ and the oxide thickness. Therefore, the energy barrier of FM should be kept larger than 60 k_BT not only for the better retention but also for the smaller variability during the read operation.

1.18.3 Benchmarking the Read and Write performances of SOT-MRAM

Overall, t_{read} and E_{read} of the SOT-MRAM are still larger than SRAM because of the small TMR ratio~120% as seen in **Figure 45**(c). Using the separated BL (2BL) scheme can reduce the parasitic resistances and capacitances thus reduce t_{read} and E_{read} compared to 1BL with the disadvantage of a larger cell area. Moreover, using the fast-read scheme shows a smaller t_{read} and E_{read} with t_{read} almost comparable to SRAM.

For the write performances, we found that the SOT-MRAM using IMA FM has smaller write access time (t_{write}) and E_{write} compared to the STT-assisted SOT-MRAM and the STT-MRAM. This is because the critical current density of the magnet switching is larger for the PMA FM than the IMA FM. Although the STT-assisted current helps to break the symmetry of FM and lifts the need of an external magnetic field for PMA FM, the STT-assisted current adds extra power consumption due to the joule heating effect. However,

the PMA FM has the advantage of smaller layout area as technology scales down. Therefore, finding efficient SOT materials with a high out-of-plane anti-damping-like torque efficiency may push E_{write} even smaller than that of SRAM. The SOT materials with higher σ_{SOT} and ξ_{DL} also help to alleviate the joule heating effect which becomes more severe when MTJ area is scaled down.

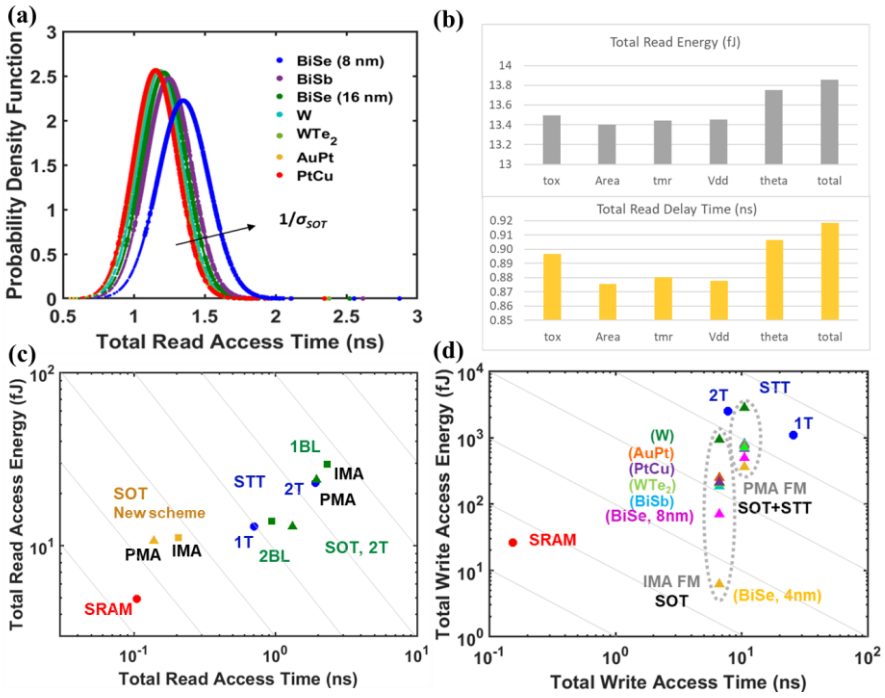

Figure 45 – (a) Probability density functions of the read delay time of SOT-MRAM with in-plane ferromagnet using various SOT materials. (b) The read delay time and energy of SOT-MRAM compared with STT-MRAM (blue), SRAM (red), and SOT-MRAM using fast-read two-transistors scheme (orange). Comparison of the (c) read and (d) write performances of SOT-MRAM, STT-MRAM, and SRAM.

1.19 Conclusion

We have benchmarked and projected the write performance of SOT-MRAM under varying conductivity or spin Hall angle of SOT materials by considering the current shunting effects, read disturb rate and the thermal noise in FM. Our results show that the lumped model underestimates the write current especially for the resistive SOT channel during the write operation. The read disturb incidences happen when the resistivity of the SOT channel is small and the spin Hall angle is large. The array level performance analyses show that SOT-MRAM using IMA FM has smaller write energy and delay values compared to the STT-assisted SOT-MRAM and STT-MRAM. New SOT materials with out-of-plane anti-damping-like torque needs to be explored to achieve higher write efficiency for SOT-MRAM using PMA FM. We also benchmarked the read performances of SOT-MRAM considering the variability from devices, process for various SOT materials. A resistive SOT channel may degrade the read delay time due to the effective smaller on/off ratio of the resistance of the cell MTJ. Using the fast-read scheme not only increase the read speed but also increase the design space for material choices of the SOT channel. Our Monte Carlo simulations also show that the variability of the MTJ resistance that comes from the thermal noise and the oxide thickness are critical on the read performance. Our model provides important guidelines for designing SOT-MRAM from material, device to array level.

FUTURE PROSPECTS AND CHALLENGES OF SPINTRONIC DEVICES

1.20 Technology challenges of spintronic devices

The main challenge for spintronic devices is the scaling of the magnetic tunnel junction as technology advances. To increase the array density and the area efficiency of the spintronic memory, the magnetization of the free layer ferromagnet with PMA is preferred compared to the ferromagnet with IMA. However, as the size of the ferromagnet is scaled down, the magnitude of the thermal field increases thus the thermal stability of the magnet decreases as shown in **Figure 46**. Therefore, the engineering of the free layer ferromagnet becomes critical as discussed later in Chapter 6.1.1.

Reducing the size of the magnet also increases the relative variability in magnet dimensions due to the challenges in patterning MTJ stackes. In contrast to the Si technology which uses reactive ion etching (RIE), the MTJ patterning is often done using ion beam etching because of the low volatility of etching by-products and vulnerability of the magnetic materials to the chemical reaction with etching gases. In addition, the chemical species such as hydrogen, nitrogen, and oxygen that are used during the passivation may react with the surface of the magnetic materials [133]. Therefore, the size variation and the edge roughness after the MTJ patterning may cause variation on the resistance-area (RA) product, the thermal barrier, and the critical current of magnet switching of the MTJ thus reducing the read margin of the MTJ.

Last, as the size of the MTJ decreases, the resistance of the MTJ drastically increases under the same resistance-area (RA) product and the thickness of the MgO layer. The high resistance MTJ poses many challenges on the write operation of the STT-MRAM since a higher write voltage is needed for sufficient write current. To reduce the RA product of the MTJ, one can choose a thinner thickness of MgO. However, reducing the thickness of MgO also reduces the TMR ratio, the breakdown voltage of MgO, and the read disturb rate may be high. Therefore, the engineering of the MTJ to achieve lower RA product while maintaining a high TMR ratio is crucial for the future MRAM technology.

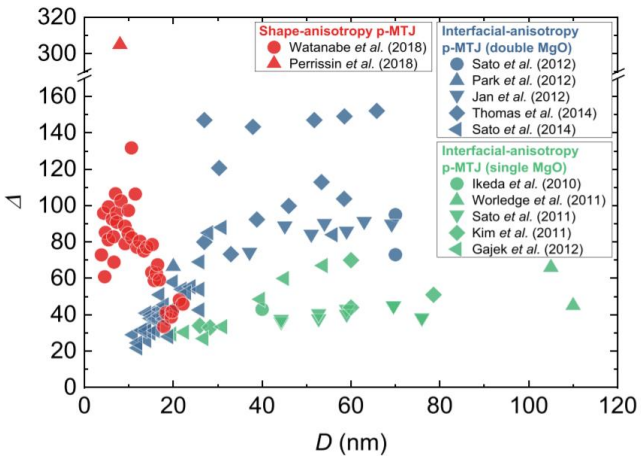

Figure 46 – The energy barrier of the magnetic tunnel junction with perpendicular magnetic anisotropy (PMA) under varying diameter at room temperature. [37] Reprinted from "Scaling magnetic tunnel junction down to single-digit nanometers—Challenges and prospects," B. Jinnai, K. Watanabe, S. Fukami, and H. Ohno, Appl. Phys. Lett., vol. 116, no. 16, p. 160501, Apr. 2021. Copyright 2021 AIP Publishing.

1.20.1 Engineering of the free layer ferromagnet

Currently, there are various ways to enhance the energy barrier of the MTJ including stacking of CoFeB/MgO interfaces or using the inherent shape anisotropy energy of FM as shown in **Figure 47**. By using the multi-layered CoFeB/MgO, the interface anisotropy energy is enhanced. This is because the interface anisotropy energy of the ferromagnet is expressed as $K_u(V) = \frac{K_i(V)}{t_{FM}} = (K_i(0) - \xi \frac{V}{t_{ox}})/t_{FM}$ where $K_i(0)$ is the interface anisotropy energy, ξ is the VCMA coefficient, t_{FM} is the thickness of the ferromagnet, t_{ox} is the oxide thickness of the MTJ, and V is the voltage across the MTJ. Therefore, when the interface area increases, the interface anisotropy energy increases. Recent experiments [132] have also demonstrated that the diameter of the MTJ can be as small as 3.5nm using the multilayered ferromagnet structure and the critical current of magnet switching is as small as 8μA. To further increase the energy barrier of the MTJ as device scaling down, one can combine the out-of-plane shape anisotropy energy and the multi-layered interface anisotropy energy as shown in **Figure 47** (c).

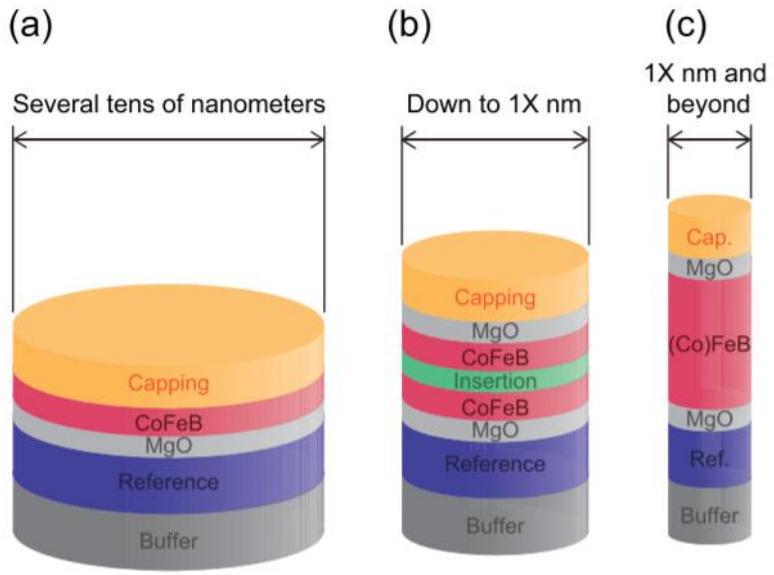

Figure 47 – Schematics of perpendicular MTJ (p-MTJ) for the MTJ scaling. (a) Interfacial p-MTJ with a single CoFeB/MgO interface. (b) Interfacial p-MTJ with double CoFeB/MgO interface and an insertion layer. (c) p-MTJ with shape anisotropy in the out-of-plane direction. [37] Reprinted from "Scaling magnetic tunnel junction down to single-digit nanometers—Challenges and prospects," B. Jinnai, K. Watanabe, S. Fukami, and H. Ohno, Appl. Phys. Lett., vol. 116, no. 16, p. 160501, Apr. 2021. Copyright 2021 AIP Publishing.

1.21 Future prospects

1.21.1 Domain wall nanoelectronics

Ferroic domain walls include ferroelectric, ferroelastic, and ferromagnetic domain walls. As the lateral dimensions of ferroic devices are scaled down, domains are more easily formed due to high surface-to-volume ratios. Among them, devices based on magnetic domain walls have been studied such as the racetrack memory [134] or logic

devices [135]. In addition to the ferromagnetic domain walls, ferroelectric and ferroelastic domain walls may also act as the device itself as demonstrated in [136]. Different from the ferromagnetic domain walls which have fast domain wall velocities, the ferroelectric domain walls usually have slower domain wall velocities [137]. However, ferroelectric domain walls may provide new features such as domain wall interaction or conductive walls. For example, the ferroelectric domain walls can be positively or negatively charged or remain neutral depending on the orientations of the spontaneous polarization in each domain. By controlling the domain wall conductivities, the ferroelectric domain walls can be used as a memory [136], [138] or a memristor [139]. Moreover, multiferroic domain walls are of interest due to the coexistence of ferroelectricity and magnetic order. In our model as discussed in chapter 3, we only consider the single domain BFO/CoFe heterojunction without the domain wall formation and domain interaction for scaled devices. Future studies may explore the ferroelectric domain walls in the BFO layer and the interaction with the ferromagnetic domain walls in the CoFe layer.

1.21.2 Antiferromagnetic memory

Antiferromagnets (AFM) have zero net magnetization with the magnetization in each sublattice being antiparallel to the neighbouring sublattices. Although AFMs have been widely used to pin the reference ferromagnetic layer in the MTJ structure, AFM can also be used as a memory device by storing the information in its AFM axis [140]. The main advantages of the antiferromagnets includes its high oscillation frequency because of the strong exchange coupling within cells, and the insensitivity to the external magnetic field perturbation due to the zero net magnetization. To switch a local magnetic moment in an AFM layer, one can pass electrical current through the non-centrosymmetric unit cell

crystal to generate local non-equilibrium spin polarizations with opposite signs but equal magnitudes on the two inversion-partners of the AFM cells. This staggered spin-orbit torque generated in an AFM is referred to as the Neel spin-orbit-torque [141], [142] which usually happens in a crystal with broken symmetry. For example, AFM materials such as Mn_2Au [143] and CuMnAs are demonstrated to be electrically switched by the applied electrical current. Therefore, antiferromagnets are considered promising magnetic materials for high-speed and high-density memory applications. However, the read signal for such AFM memory devices is currently too small since the anisotropic magnetoresistance (AMR) ratio is as low as few percentage points. The relativistic tunneling AMR (TAMR) where the resistance is dominated by the tunneling probability from one electrode to the other can have magnetoresistances as large as ~160% at 4K [144]; however, further studies are needed to achieve such high TAMR values at the room temperature. To summarize, antiferromagnets shows unique characteristics of insensitivity to external magnetic field, fast switching dynamics, and reduced crosstalk for high density arrays. Research in the AFM materials, TAMR at room temperature, and the spin transport are critical for realizing AFM devices for future applications.

1.21.3 Applications of the ME-devices

Magnetoeletric devices made up of the BFO/CoFe heterojunction and the magnetic tunnel junction can be used as two-state memory cells as discussed in chapter 4. In addition to acting as a two-state device, the ME device can be implemented as a device with multi-resistance state by considering multiple input nodes for the BFO layer as shown in **Figure 48**. If the input voltage of terminal 1 (V_{in1}) is larger than the coercive voltage of the BFO (V_C), i.e., $V_{in1} > V_C$, the polarization switching happens in the BFO1 layer, and the CoFe

layer on top of the BFO1 also switches. By varying the input voltages, we can obtain four different resistance states in the three-inputs MTJ as shown in **Figure 49**. Similarly, when there are five input terminals of BFO, there are six different output resistance states as shown in **Figure 50**. Therefore, there are *n+1* types of output states when we have *n* input terminals. This multi-resistance ME device can be implemented as a majority gate when combining with a reference MTJ and a sense-amplifier (SA) as shown in **Figure 51** (a).

Moreover, this multi-resistance ME device can also be used as a controlled-logic gate by proper design of the input nodes and output states. Taking the three-inputs ME device as an example, there are four resistance states R_1~R_4 from low to high depending on the input voltages of the three terminals V_{in1}, V_{in2}, and V_{in3}. If V_{in2} = 0, the output resistance can only be R_1, R_2, and R_4. By properly choosing the resistance value of the reference MTJ between R_2 and R_4, the output will be a logic AND gate. Similarly, if V_{in2} = 1 ($>V_C$), the output resistance can only be R_1, R_3, and R_4. By choosing the resistance value of the reference MTJ between R_2 and R_4, the output will be a logic OR gate.

In addition to the logic operation, the multi-resistance ME device can also be used as a memory device by combining the multi-resistance ME-MTJ with a reference MTJ and an inverter as shown in **Figure 51** (b). When the resistance state of the ME-MTJ is low, the gate voltage of the read access transistor will be low, and the output current will be low. Similarly, when the resistance state of the ME-MTJ is high, the gate voltage of the read access transistor will be high, and the output current will be high. The magnitude of the output current would then depend on the resistance state of the ME device. The disadvantage of the multi-resistance is the larger cell layout area due to the multiple input terminals.

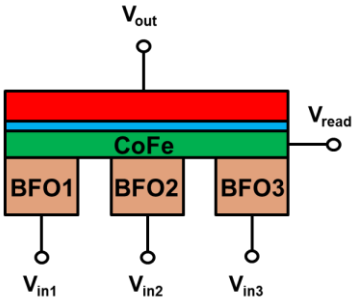

Figure 48 – Schematics of the multi-resistance magnetoelectric device with three input terminals. The free layer ferromagnet (green) is connected with three BFO layers, and the fixed layer ferromagnet (red) is connected with the output node (V_{out}) and read voltage (V_{read}).

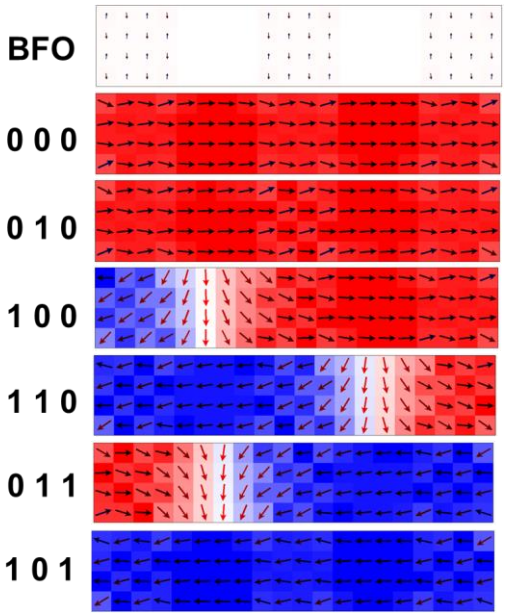

Figure 49 – The magnetic structure of the BFO and CoFe layers with three input terminals in the *x-y* plane. The input voltages of BFO from top to down are: (000), (010), (100), (110), (011), (101).

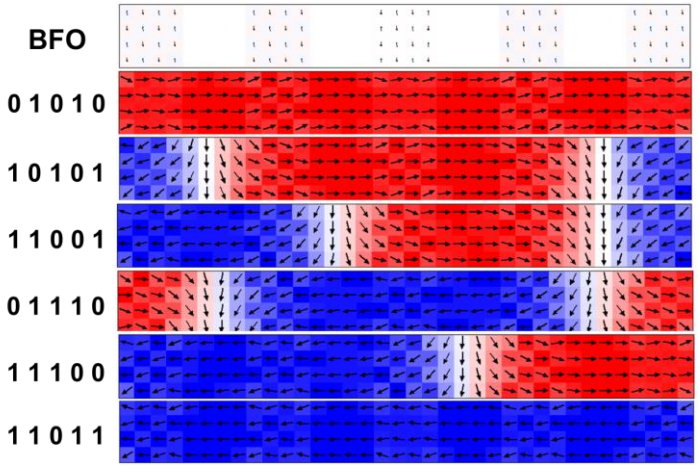

Figure 50 – The magnetic structure of the BFO and CoFe layers with five input terminals in the *x-y* plane. The input voltages of BFO from top to down are: (01010), (10101), (11001), (01110), (11100), (11011).

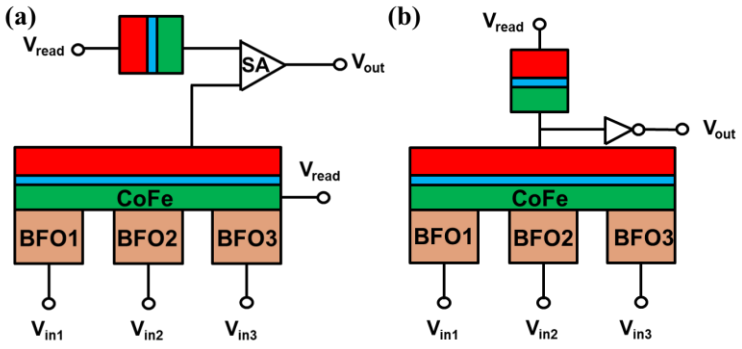

Figure 51 – Schematics of (a) the three-input majority gate and (b) the multi-resistance memory device based on the ME device.

1.21.4 New materials and physical mechanisms associated with spin-orbit torque

In Chapter 5, we have discussed various SOT materials including heavy metals, alloys, Weyl semi-metals, and topological insulators. In addition, there are other SOT materials that are being explored. Antiferromagnets such as PtMn [145] and IrMn [146]

have been demonstrated to achieve field-free PMA magnet switching due to the exchange bias between antiferromagnet and ferromagnets and the strong spin Hall effects of antiferromagnet. The interface of the wide-bandgap oxide materials such as $SrTiO_3$(STO) and $LaAlO_3$(LAO) can form a conductive two-dimensional electron gas (2DEG), thus the strong Rashba spin-orbit coupling at the interface causes strong charge-to-spin conversion efficiency of ~ 6.3 in the STO/LAO/CoFeB structure [147]. To further explore these various SOT materials for SOT-MRAM, it is crucial to study the advantages and disadvantages of these materials in terms of charge-to-spin conversion efficiency, conductivity, and the out-of-plane spin Hall angle.

In theory, the spin-orbit torque originates from the bulk spin Hall effect and the interface Rashba-Edelstein effect as discussed in Chapter 1. Moreover, the spin-orbit torque also couples to the thermal effect, strain effect, and the orbital angular momentum of the lattice. The orbital Hall effect [148]–[150] refers to the orbital momentum currents generated by the electric field in the bilayer system using the transition metals. Usually, the torque generated by the spin injection and the orbital injection compete with each other. However, by identifying systems where the orbital injection and the spin injection torques are in the same direction, one can enhance the SOT efficiency by a factor of 16 as observed in the (TmIG)/Pt/CuO_x interface [151]. The thermal gradient may also generate spin currents that can switch the magnetization of the ferromagnet. The torque generated by the thermal gradient is called thermal spin-orbit torque (TSOT) [152]. Experiments also show that the TSOT can assist the electrical SOT and reduce the critical current of magnet switching as measured in the W/CoFeB/MgO layers [153]. Since there is Joule heating associated with the charge currents that are applied on the SOT channel during the write

operation, studying the interplay between SOT and TSOT is essential to understand the write performance and the thermal stability of the ferromagnet. Last, the coupling between the spin-orbit coupling and the strain may tune the magnitude of the SOT as observed in the Ta/MgO/CoFeB/W on the PMN-PT substrate [154]. This is because the magnitude of the damping-like torque and the field-like torque responds differently to the strain as they originate from different electronic states. Understanding the coupling of the spin-orbit torque to the orbital torque, TSOT and the strain effects can help to improve or tune the SOT efficiency which is useful for the memory application.

To summarize, the study of the spin-orbit torque is an emerging field due to its richness of physics that couples spintronics, electronics, orbitronics and spin caloritronics. In addition to the memory applications such as the SOT-MRAM, spin-orbit torque may be used in devices such as a magnetic synapse or spiking neurons in neuromorphic computing [155], physical unclonable functions (PUF) [156], and multibit adders based on the domain wall magnetic tunnel junction [157]. Therefore, future studies that are holistic and crosscut research in materials, devices, circuits, and systems to best leverage spin-orbit torque are important to achieve fast and low power memory modules.

APPENDIX A. RENORMALIZATION OF MAGNETIC PARAMETERS IN BFO AND THE J_{INT}

To simulate a G-type antiferromagnet (AFM) in OOMMF, the exchange stiffness constant of AFM needs to be normalized with varying mesh sizes and shapes.

The exchange energy in OOMMF is expressed as $E_i = \sum_{j \in N_i} A_{ij} \frac{\boldsymbol{m_i} \cdot (\boldsymbol{m_i} - \boldsymbol{m_j})}{\Delta_{ij}^2}$, where N_i is the set of the 6 nearest cells, A_{ij} is the exchange stiffness constant between cell i and cell j, and Δ_{ij} is the discretization steps between the cell i and the cell j. This exchange energy comes from the approximation of a Heisenberg-type exchange coupling assuming the magnetization m_i is continuous. This means that the total exchange energy $E_{exch} = -2J \sum_{i<j}^{nn} J_{ij} \boldsymbol{S_i} \boldsymbol{S_j} \cong \ -2J \sum_{i<j}^{nn} \boldsymbol{S_i} \boldsymbol{S_j} = -2 \sum_{i<j} J_{ij} S^2 cos\theta_{ij}$ where J_{ij} is the exchange coupling constant, $\boldsymbol{S_i}, \boldsymbol{S_j}$ are the spin vectors of sublattice i and j, and θ_{ij} is the angle between vectors $\boldsymbol{S_i}$ and $\boldsymbol{S_j}$. Here the factor of two denotes that there is exchange coupling energy from cell i and the cell j and vice versa. Suppose θ_{ij} is small, we can approximate $E_{exch} \cong -2 \sum_{i<j} J_{ij} S^2 (1 - \frac{1}{2!} \theta_{ij}^2) = \sum_{i<j} J_{ij} S^2 \theta_{ij}^2 + constant$ by using the Taylor expansion. Since θ_{ij} is a continuous variable, θ_{ij} can be approximated as $\theta_{ij} \cong a \frac{\partial \theta}{\partial x}$ in the numerical simulation where a is the discretization step. However, this assumption that θ_{ij} is small is invalid for an AFM material since the magnetic moment in an AFM is staggered in a positive to negative direction. Therefore, the exchange energy is non-convergent for AFM when using the normal numerical expression of the exchange coupling as used in a FM.

To simulate the exchange coupling field in AFM directly from the spin Hamiltonian, we have done a micromagnetic simulation in MATLAB using $H_{exch}^{ij} = -\frac{1}{\mu_0 M_s a^3}\frac{\partial E_{exch}^{ij}}{\partial \alpha_j} = \frac{JS^2}{\mu_0 M_s a^3}\left(\alpha_i^x, \alpha_i^y, \alpha_i^z\right) = \frac{2A}{\mu_0 M_s a^2}\left(\alpha_i^x, \alpha_i^y, \alpha_i^z\right)$, where α_j is the direction cosines of the cell j, α_i is the direction cosines of the neighboring cell i, a is the lattice constant, $E_{exch}^{ij} = -JS^2(\alpha_j^x\alpha_i^x + \alpha_j^y\alpha_i^y + \alpha_j^z\alpha_i^z)$, and $A = \frac{JS^2}{2a} < 0$. Our results show the same result as done in OOMMF when using the same mesh size, i.e. 1×1×1 nm^3 as shown in **Figure 52**. However, the simulation results will vary when we change the mesh size in OOMMF since the numerical expression of the exchange coupling field is nonconvergent for an AFM. To calculate the exchange coupling field in an AFM layer in OOMMF using larger mesh sizes under the same exchange energy density, the exchange stiffness constant needs to be renormalized. The renormalization of the exchange stiffness constant is done by considering the number of nearest neighbors in each cell with varying mesh sizes. The exchange energy in AFM is expressed numerically as

$$E_{ex,AFM} = J_{AFM}\left(\left[\sum_{i\in 6\ n.n.}\frac{m_i(r_i)\cdot(m_i(r_i)-m_i(r_i\pm\Delta_j))}{\Delta_{ij}^2} + \sum_{i\in 5\ n.n.}\frac{m_i(r_i)\cdot(m_i(r_i)-m_i(r_i\pm\Delta_j))}{\Delta_{ij}^2} + \sum_{i\in 4\ n.n.}\frac{m_i(r_i)\cdot(m_i(r_i)-m_i(r_i\pm\Delta_j))}{\Delta_{ij}^2} + \sum_{i\in 3\ n.n.}\frac{m_i(r_i)\cdot(m_i(r_i)-m_i(r_i\pm\Delta_j))}{\Delta_{ij}^2}\right]\right), \quad (54)$$

where J_{AFM} is the exchange stiffness constant of AFM, $n.n.$ denotes the nearest neighbors of the cell i and Δ_{ij} is the mesh size in *x*, *y* or *z* direction. The renormalized J_{AFM} is then calculated by considering a fixed exchange coupling energy density as the mesh size varies.

The exchange coupling energy in AFM is approximated as the summation of the number of nearest neighbors, which is expressed as

$$J_{AFM}\left\{\frac{[(n_x-2)\cdot(n_y-2)\cdot(n_z-2)]\cdot 2+[(n_x-2)\cdot(n_y-2)\cdot 2\cdot 2+(n_x-2)\cdot(n_z-2)\cdot 2\cdot 2+(n_y-2)\cdot(n_z-2)\cdot 2]+[(n_x-2)\cdot 4\cdot 2+(n_y-2)\cdot 4+(n_z-2)\cdot 4]+8}{\Delta_x^2}\right.$$
$$+\frac{[(n_x-2)\cdot(n_y-2)\cdot(n_z-2)]\cdot 2+[(n_x-2)\cdot(n_y-2)\cdot 2\cdot 2+(n_x-2)\cdot(n_z-2)\cdot 2+(n_y-2)\cdot(n_z-2)\cdot 2\cdot 2]+[(n_x-2)\cdot 4+(n_y-2)\cdot 4\cdot 2+(n_z-2)\cdot 4]+8}{\Delta_y^2} \quad (55)$$
$$\left.+\frac{[(n_x-2)\cdot(n_y-2)\cdot(n_z-2)]\cdot 2+[(n_x-2)\cdot(n_y-2)\cdot 2+(n_x-2)\cdot(n_z-2)\cdot 2\cdot 2+(n_y-2)\cdot(n_z-2)\cdot 2\cdot 2]+[(n_x-2)\cdot 4+(n_y-2)\cdot 4+(n_z-2)\cdot 4\cdot 2]+8}{\Delta_z^2}\right\}$$

where n_x , n_y, and n_z are the number of grid points in *x*, *y* or *z* directions when mesh size varies. The comparison of the switching dynamics of AFM when the mesh size varies from 0.4×0.4×0.4 nm3 to 20×20×2 nm3 is shown in **Figure 53**.

To renormalize the interface exchange coupling coefficient (J_{int}) between BFO and CoFe, we compare the magnitude of the coercive field of the BFO/CoFe heterojunction devices when the length and width of the device are both 100 nm, and the thickness of BFO and CoFe layers are 30 nm and 2 nm, respectively. The comparison of the coercive field under varying mesh sizes is shown in **Figure 54**.

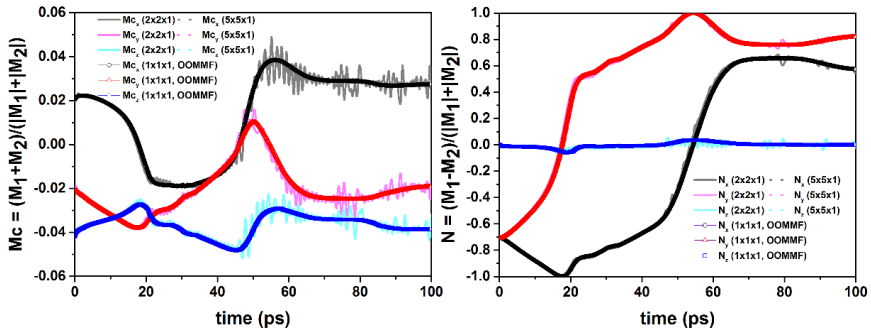

Figure 52 – Comparison of the switching curves of (a) the weak magnetization (M_c) and (b) the Neel vector (N) using OOMMF versus MATLAB. In the MATLAB, the

exchange coupling in the antiferromagnet is expressed as $H_{exch}^{ij} = \frac{2A}{\mu_0 M_s a^2}(\alpha_i^x, \alpha_i^y, \alpha_i^z)$ which is independent of the mesh size.

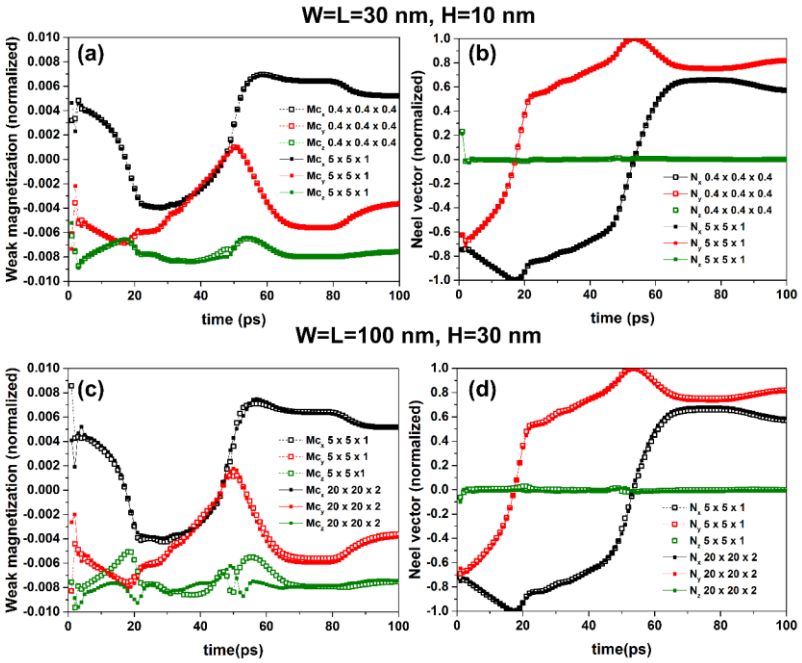

Figure 53 – The switching curves of (a) the weak magnetization (M_c) and (b) the Neel vector (N) of BFO under renormalized exchange stiffness constant (J_{AFM}) from 0.4×0.4×0.4 to 5×5×1 when width and length are equal to 100 nm, and height is 30 nm thick.

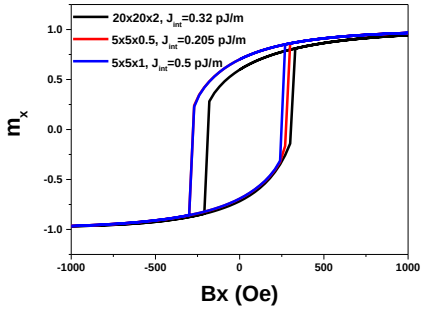

Figure 54 – Comparison of the magnetic hysteresis loop under varying mesh size (20×20×2, 5×5×0.5, 5×5×1) with constant magnetic coercive field.

REFERENCES

[1] M. T. Bohr and I. A. Young, "CMOS Scaling Trends and Beyond," *IEEE Micro*, vol. 37, no. 6, pp. 20–29, Nov. 2017, doi: 10.1109/MM.2017.4241347.

[2] P. A. Gargini, "How to successfully overcome inflection points, or long live Moore's law," *Comput. Sci. Eng.*, vol. 19, no. 2, pp. 51–62, Mar. 2017, doi: 10.1109/MCSE.2017.32.

[3] T. N. Theis and H.-S. P. Wong, "The End of Moore's Law: A New Beginning for Information Technology," *Comput. Sci. Eng.*, vol. 19, no. 2, pp. 41–50, Mar. 2017, doi: 10.1109/MCSE.2017.29.

[4] S. Manipatruni, D. E. Nikonov, and I. A. Young, "Beyond CMOS computing with spin and polarization," *Nat. Phys.*, vol. 14, p. 338, 2018, doi: 10.1038/s41567-018-0101-4.

[5] S. Yu and P.-Y. Chen, "Emerging Memory Technologies: Recent Trends and Prospects," *IEEE Solid-State Circuits Mag.*, vol. 8, no. 2, pp. 43–56, Spring 2016, doi: 10.1109/MSSC.2016.2546199.

[6] D. Fan, S. Angizi, and Z. He, "In-Memory Computing with Spintronic Devices," in *2017 IEEE Computer Society Annual Symposium on VLSI (ISVLSI)*, Jul. 2017, pp. 683–688. doi: 10.1109/ISVLSI.2017.116.

[7] N. K. Upadhyay, H. Jiang, Z. Wang, S. Asapu, Q. Xia, and J. J. Yang, "Emerging Memory Devices for Neuromorphic Computing," *Adv. Mater. Technol.*, vol. 4, no. 4, p. 1800589, 2019, doi: 10.1002/admt.201800589.

[8] A. Danowitz, K. Kelley, J. Mao, J. P. Stevenson, and M. Horowitz, "CPU DB: recording microprocessor history," *Commun. ACM*, vol. 55, no. 4, pp. 55–63, Apr. 2012, doi: 10.1145/2133806.2133822.

[9] M. N. Baibich *et al.*, "Giant magnetoresistance of (001)Fe/(001)Cr magnetic superlattices," *Phys. Rev. Lett.*, vol. 61, no. 21, pp. 2472–2475, 1988, doi: 10.1103/PhysRevLett.61.2472.

[10] G. Binasch, P. Grünberg, F. Saurenbach, and W. Zinn, "Enhanced magnetoresistance in layered magnetic structures with antiferromagnetic interlayer exchange," *Phys. Rev. B*, vol. 39, no. 7, pp. 4828–4830, 1989, doi: 10.1103/PhysRevB.39.4828.

[11] J. S. Moodera, L. R. Kinder, T. M. Wong, and R. Meservey, "Large magnetoresistance at room temperature in ferromagnetic thin film tunnel junctions,"

Phys. Rev. Lett., vol. 74, no. 16, pp. 3273–3276, 1995, doi: 10.1103/PhysRevLett.74.3273.

[12] T. Miyazaki and N. Tezuka, "Giant Magnetic Tunneling Effect in $Fe/Al_2O_3/Fe$ Junction," *J. Magn. Magn. Mater.*, vol. 139, pp. L231–L234, 1995.

[13] J. C. Slonczewski, "Current-driven excitation of magnetic multilayers," *J. Magn. Magn. Mater.*, 1996, doi: 10.1016/0304-8853(96)00062-5.

[14] J. C. Slonczewski, "Excitation of spin waves by an electric current," *J. Magn. Magn. Mater.*, vol. 195, no. 2, pp. 261–268, 1999, doi: 10.1016/S0304-8853(99)00043-8.

[15] L. Berger, "Emission of spin waves by a magnetic multilayer traversed by a current," *Phys. Rev. B*, vol. 54, no. 13, pp. 9353–9358, 1996.

[16] L. Berger, "Effect of interfaces on gilbert damping and ferromagnetic resonance linewidth in magnetic multilayers," *J. Appl. Phys.*, vol. 90, no. 9, pp. 4632–4638, 2001, doi: 10.1063/1.1405824.

[17] I. M. Miron *et al.*, "Current-driven spin torque induced by the Rashba effect in a ferromagnetic metal layer," *Nat. Mater.*, vol. 9, no. 3, pp. 230–234, 2010, doi: 10.1038/nmat2613.

[18] A. Chernyshov, M. Overby, X. Liu, J. K. Furdyna, Y. Lyanda-Geller, and L. P. Rokhinson, "Evidence for reversible control of magnetization in a ferromagnetic material by means of spin-orbit magnetic field," *Nat. Phys.*, vol. 5, no. 9, pp. 656–659, 2009, doi: 10.1038/nphys1362.

[19] I. M. Miron *et al.*, "Perpendicular switching of a single ferromagnetic layer induced by in-plane current injection," *Nature*, vol. 476, no. 7359, pp. 189–193, 2011, doi: 10.1038/nature10309.

[20] L. Liu, C.-F. Pai, Y. Li, H. W. Tseng, D. C. Ralph, and R. A. Buhrman, "Spin-Torque Switching with the Giant Spin Hall Effect of Tantalum," *Science*, vol. 336, no. 6081, pp. 555–558, 2012, doi: 10.1126/science.1218197.

[21] L. Liu, T. Moriyama, D. C. Ralph, and R. A. Buhrman, "Spin-torque ferromagnetic resonance induced by the spin Hall effect," *Phys. Rev. Lett.*, vol. 106, no. 3, pp. 1–4, 2011, doi: 10.1103/PhysRevLett.106.036601.

[22] Y. Shiota *et al.*, "Pulse voltage-induced dynamic magnetization switching in magnetic tunneling junctions with high resistance-area product," *Appl. Phys. Lett.*, vol. 101, no. 10, 2012, doi: 10.1063/1.4751035.

[23] D. Zhang, Z. Zhao, T. Peterson, and J. Wang, "Field-free voltage-controlled magnetization switching in perpendicular MTJs for ultra- low energy spintronic memory and computing applications Key Result slide goes here Summary slide goes here." p. 2018, 2018.

[24] M. Fiebig, “Revival of the magnetoelectric effect,” *Journal of Physics D: Applied Physics*, vol. 38, no. 8. pp. 123–152, 2005. doi: 10.1088/0022-3727/38/8/R01.

[25] S. Fusil, V. Garcia, A. Barthélémy, and M. Bibes, “Magnetoelectric Devices for Spintronics Keynote Topic,” 2014, doi: 10.1146/annurev-matsci-070813-113315.

[26] W. Eerenstein, N. D. Mathur, and J. F. Scott, “Multiferroic and magnetoelectric materials,” *Nature*, vol. 442, no. 7104, pp. 759–765, 2006, doi: 10.1038/nature05023.

[27] D. E. Nikonov and I. A. Young, “Benchmarking spintronic logic devices based on magnetoelectric oxides,” *J. Mater. Res.*, vol. 29, no. 18, pp. 2109–2115, 2014, doi: 10.1557/jmr.2014.243.

[28] D. E. Nikonov and I. A. Young, “Overview of beyond-CMOS devices and a uniform methodology for their benchmarking,” *Proc. IEEE*, vol. 101, no. 12, pp. 2498–2533, 2013, doi: 10.1109/JPROC.2013.2252317.

[29] D. E. Nikonov and I. A. Young, “Benchmarking of Beyond-CMOS Exploratory Devices for Logic Integrated Circuits,” *IEEE J. Explor. Solid-State Comput. Devices Circuits*, vol. 1, no. February, pp. 3–11, 2015, doi: 10.1109/JXCDC.2015.2418033.

[30] J. E. Miltat and M. J. Donahue, “Numerical Micromagnetics: Finite Difference Methods,” in *Handbook of Magnetism and Advanced Magnetic Materials*, 2007, pp. 1–23. doi: 10.1002/9780470022184.

[31] E. Grimaldi *et al.*, “Single-shot dynamics of spin–orbit torque and spin transfer torque switching in three-terminal magnetic tunnel junctions,” *Nat. Nanotechnol.*, vol. 15, no. 2, pp. 111–117, Feb. 2020, doi: 10.1038/s41565-019-0607-7.

[32] W. F. Brown, “Thermal Fluctuations of a Single-Domain Particle,” *Phys. Rev.*, vol. 130, no. 5, pp. 1677–1686, Jun. 1963, doi: 10.1103/PhysRev.130.1677.

[33] R. Kubo and N. Hashitsume, “Brownian Motion of Spins,” *Prog. Theor. Phys. Suppl.*, vol. 46, pp. 210–220, 1970, doi: 10.1143/PTPS.46.210.

[34] S. Ament, N. Rangarajan, and S. Rakheja, “A practical guide to solving the stochastic Landau-Lifshitz-Gilbert-Slonczewski equation for macrospin dynamics,” p. 17.

[35] S. Yuasa, T. Nagahama, A. Fukushima, Y. Suzuki, and K. Ando, “Giant room-temperature magnetoresistance in single-crystal Fe/MgO/Fe magnetic tunnel junctions,” *Nat. Mater.*, vol. 3, no. 12, pp. 868–871, Dec. 2004, doi: 10.1038/nmat1257.

[36] I. Žutić, J. Fabian, and S. Das Sarma, “Spintronics: Fundamentals and applications,” *Rev. Mod. Phys.*, vol. 76, no. 2, pp. 323–410, Apr. 2004, doi: 10.1103/RevModPhys.76.323.

[37] B. Jinnai, K. Watanabe, S. Fukami, and H. Ohno, “Scaling magnetic tunnel junction down to single-digit nanometers—Challenges and prospects,” *Appl. Phys. Lett.*, vol. 116, no. 16, p. 160501, Apr. 2020, doi: 10.1063/5.0004434.

[38] D. C. Ralph and M. D. Stiles, “Spin transfer torques,” *J. Magn. Magn. Mater.*, vol. 320, no. 7, pp. 1190–1216, Apr. 2008, doi: 10.1016/j.jmmm.2007.12.019.

[39] J. Z. Sun, “Spin-current interaction with a monodomain magnetic body: A model study,” *Phys. Rev. B*, vol. 62, no. 1, pp. 570–578, Jul. 2000, doi: 10.1103/PhysRevB.62.570.

[40] S. Mangin, Y. Henry, D. Ravelosona, J. A. Katine, and E. E. Fullerton, “Reducing the critical current for spin-transfer switching of perpendicularly magnetized nanomagnets,” *Appl. Phys. Lett.*, vol. 94, no. 1, p. 012502, Jan. 2009, doi: 10.1063/1.3058680.

[41] J. A. Katine and E. E. Fullerton, “Device implications of spin-transfer torques,” *J. Magn. Magn. Mater.*, vol. 320, no. 7, pp. 1217–1226, Apr. 2008, doi: 10.1016/j.jmmm.2007.12.013.

[42] N. Locatelli, V. Cros, and J. Grollier, “Spin-torque building blocks,” *Nat. Mater.*, vol. 13, no. 1, pp. 11–20, Jan. 2014, doi: 10.1038/nmat3823.

[43] M. Carpentieri and G. Finocchio, “Chapter 7 - Spintronic Oscillators Based on Spin-Transfer Torque and Spin-Orbit Torque,” in *Handbook of Surface Science*, vol. 5, R. E. Camley, Z. Celinski, and R. L. Stamps, Eds. North-Holland, 2015, pp. 297–334. doi: 10.1016/B978-0-444-62634-9.00007-2.

[44] S. Manipatruni *et al.*, “Scalable energy-efficient magnetoelectric spin–orbit logic,” *Nature*, 2018, doi: 10.1038/s41586-018-0770-2.

[45] P. Bruno, “Theory of interlayer magnetic coupling,” *Phys. Rev. B*, vol. 52, no. 1, pp. 411–439, Jul. 1995, doi: 10.1103/PhysRevB.52.411.

[46] M. D. Stiles, “Interlayer exchange coupling,” *J. Magn. Magn. Mater.*, p. 16, 1999.

[47] P. Bruno and C. Chappert, “Ruderman-Kittel theory of oscillatory interlayer exchange coupling,” *Phys. Rev. B*, vol. 46, no. 1, pp. 261–270, Jul. 1992, doi: 10.1103/PhysRevB.46.261.

[48] D. Zhang *et al.*, “Bipolar electric-field switching of perpendicular magnetic tunnel junctions through voltage-controlled exchange coupling,” p. 16, 2019.

[49] H. Schmid, “Multi-ferroic magnetoelectrics,” *Ferroelectrics*, vol. 162, no. 1, pp. 317–338, 1994, doi: 10.1080/00150199408245120.

[50] Y. Yang, I. C. Infante, B. Dkhil, and L. Bellaiche, “Strain effects on multiferroic BiFeO3 films,” *C R Phys*, vol. 16, pp. 193–203, 2015.

[51] J. T. Heron *et al.*, “Electric-field-induced magnetization reversal in a ferromagnet-multiferroic heterostructure,” *Phys. Rev. Lett.*, vol. 107, no. 21, 2011, doi: 10.1103/PhysRevLett.107.217202.

[52] J. T. Heron, D. G. Schlom, and R. Ramesh, “Electric field control of magnetism using BiFeO3-based heterostructures,” *Appl. Phys. Rev.*, vol. 1, no. 2, p. 021303, 2014, doi: 10.1063/1.4870957.

[53] J. T. Heron *et al.*, “Deterministic switching of ferromagnetism at room temperature using an electric field,” *Nature*, vol. 516, no. 7531, pp. 370–373, 2014, doi: 10.1038/nature14004.

[54] I. Dzyaloshinsky, “Thermodynamic Theory of ‘Weak’ Ferromagnetism In Antiferromagnetic Substances,” *Sov. Phys. JETP*, vol. 5, no. 6, pp. 1259–1272, 1957.

[55] T. Moriya, “Anisotropic superexchange interaction and weak ferromagnetism,” *Phys. Rev.*, vol. 120, no. 1, pp. 91–98, 1960, doi: 10.1103/PhysRev.120.91.

[56] A. K. Zvezdin and A. P. Pyatakov, “On the problem of coexistence of the weak ferromagnetism and the spin flexoelectricity in multiferroic bismuth ferrite,” *EPL*, vol. 99, no. 5, 2012, doi: 10.1209/0295-5075/99/57003.

[57] C. Ederer and N. A. Spaldin, “Weak ferromagnetism and magnetoelectric coupling in bismuth ferrite,” *Phys. Rev. B*, vol. 71, no. 6, p. 060401, 2005, doi: 10.1103/PhysRevB.71.060401.

[58] S. Senni, L. Torres, G. Sassatelli, A. Gamatie, and B. Mussard, “Exploring MRAM Technologies for Energy Efficient Systems-On-Chip,” *IEEE J. Emerg. Sel. Top. Circuits Syst.*, vol. 6, no. 3, pp. 279–292, Sep. 2016, doi: 10.1109/JETCAS.2016.2547680.

[59] T. Endoh, H. Koike, S. Ikeda, T. Hanyu, and H. Ohno, “An Overview of Nonvolatile Emerging Memories— Spintronics for Working Memories,” *IEEE J. Emerg. Sel. Top. Circuits Syst.*, vol. 6, no. 2, pp. 109–119, Jun. 2016, doi: 10.1109/JETCAS.2016.2547704.

[60] D. Saida *et al.*, “$1\times$ - to $2\times$ -nm perpendicular MTJ Switching at Sub-3-ns Pulses Below 100μ A for High-Performance Embedded STT-MRAM for Sub-20-nm CMOS,” *IEEE Trans. Electron Devices*, vol. 64, no. 2, pp. 427–431, Feb. 2017, doi: 10.1109/TED.2016.2636326.

[61] G. Panagopoulos, C. Augustine, and K. Roy, “Modeling of dielectric breakdown-induced time-dependent STT-MRAM performance degradation,” in *69th Device Research Conference*, Jun. 2011, pp. 125–126. doi: 10.1109/DRC.2011.5994447.

[62] P. K. AMIRI and K. L. WANG, “VOLTAGE-CONTROLLED MAGNETIC ANISOTROPY IN SPINTRONIC DEVICES,” *SPIN*, vol. 02, no. 03, p. 1240002, Sep. 2012, doi: 10.1142/S2010324712400024.

[63] M. Bibes and A. Barthélémy, “Towards a magnetoelectric memory,” *Nat. Mater.*, vol. 7, no. 6, Art. no. 6, Jun. 2008, doi: 10.1038/nmat2189.

[64] T. Miyazaki and N. Tezuka, “Giant magnetic tunneling effect in Fe/Al2O3/Fe junction,” *J. Magn. Magn. Mater.*, vol. 139, no. 3, pp. L231–L234, Jan. 1995, doi: 10.1016/0304-8853(95)90001-2.

[65] I. Ahmed, Z. Zhao, M. G. Mankalale, S. S. Sapatnekar, J.-P. Wang, and C. H. Kim, “A Comparative Study Between Spin-Transfer-Torque and Spin-Hall-Effect Switching Mechanisms in PMTJ Using SPICE,” *IEEE J. Explor. Solid-State Comput. Devices Circuits*, vol. 3, pp. 74–82, Dec. 2017, doi: 10.1109/JXCDC.2017.2762699.

[66] X. He *et al.*, “Robust isothermal electric control of exchange bias at room temperature,” *Nat. Mater.*, vol. 9, no. 7, pp. 579–585, Jul. 2010, doi: 10.1038/nmat2785.

[67] J. Kim *et al.*, “Spin-Hall effect MRAM based cache memory: A feasibility study,” in *2015 73rd Annual Device Research Conference (DRC)*, Jun. 2015, pp. 117–118. doi: 10.1109/DRC.2015.7175583.

[68] C. Pan and A. Naeemi, “Nonvolatile Spintronic Memory Array Performance Benchmarking Based on Three-Terminal Memory Cell,” *IEEE J. Explor. Solid-State Comput. Devices Circuits*, vol. 3, pp. 10–17, Dec. 2017, doi: 10.1109/JXCDC.2017.2669213.

[69] C. Pan and A. Naeemi, “A Nonvolatile Fast-Read Two-Transistor SRAM Based on Spintronic Devices,” *IEEE J. Explor. Solid-State Comput. Devices Circuits*, vol. 3, pp. 93–100, Dec. 2017, doi: 10.1109/JXCDC.2017.2775518.

[70] W. Kang, Z. Wang, H. Zhang, S. Li, Y. Zhang, and W. Zhao, “Advanced Low Power Spintronic Memories beyond STT-MRAM,” in *Proceedings of the on Great Lakes Symposium on VLSI 2017*, Banff Alberta Canada, May 2017, pp. 299–304. doi: 10.1145/3060403.3060589.

[71] J. Song *et al.*, “Evaluation of Operating Margin and Switching Probability of Voltage-Controlled Magnetic Anisotropy Magnetic Tunnel Junctions,” *IEEE J. Explor. Solid-State Comput. Devices Circuits*, vol. 4, no. 2, pp. 76–84, Dec. 2018, doi: 10.1109/JXCDC.2018.2880205.

[72] W. Kang, Y. Ran, Y. Zhang, W. Lv, and W. Zhao, “Modeling and Exploration of the Voltage-Controlled Magnetic Anisotropy Effect for the Next-Generation Low-Power and High-Speed MRAM Applications,” *IEEE Trans. Nanotechnol.*, vol. 16, no. 3, pp. 387–395, May 2017, doi: 10.1109/TNANO.2017.2660530.

[73] L. Liu, C.-F. Pai, D. C. Ralph, and R. A. Buhrman, “Gate voltage modulation of spin-Hall-torque-driven magnetic switching,” *ArXiv12090962 Cond-Mat*, Sep. 2012, Accessed: Jun. 02, 2021. [Online]. Available: http://arxiv.org/abs/1209.0962

[74] “Predictive Technology Model (PTM).” http://ptm.asu.edu/ (accessed May 27, 2021).

[75] L. Zhu, Daniel. C. Ralph, and R. A. Buhrman, “Highly Efficient Spin-Current Generation by the Spin Hall Effect in Au 1 − x Pt x,” *Phys. Rev. Appl.*, vol. 10, no. 3, p. 031001, Sep. 2018, doi: 10.1103/PhysRevApplied.10.031001.

[76] X. Li *et al.*, “Large and Robust Charge-to-Spin Conversion in Sputtered Weyl Semimetal WTex with Structural Disorder,” p. 22.

[77] N. H. D. Khang, Y. Ueda, and P. N. Hai, “A conductive topological insulator with large spin Hall effect for ultralow power spin–orbit torque switching,” *Nat. Mater.*, vol. 17, no. 9, pp. 808–813, Sep. 2018, doi: 10.1038/s41563-018-0137-y.

[78] M. Dc *et al.*, “Room-temperature high spin–orbit torque due to quantum confinement in sputtered BixSe(1–x) films,” *Nat. Mater.*, vol. 17, no. 9, pp. 800–807, Sep. 2018, doi: 10.1038/s41563-018-0136-z.

[79] M. Jefremow *et al.*, “Time-differential sense amplifier for sub-80mV bitline voltage embedded STT-MRAM in 40nm CMOS,” in *2013 IEEE International Solid-State Circuits Conference Digest of Technical Papers*, Feb. 2013, pp. 216–217. doi: 10.1109/ISSCC.2013.6487706.

[80] S. Shi, Y. Ou, S. V. Aradhya, D. C. Ralph, and R. A. Buhrman, “Fast Low-Current Spin-Orbit-Torque Switching of Magnetic Tunnel Junctions through Atomic Modifications of the Free-Layer Interfaces,” *Phys. Rev. Appl.*, vol. 9, no. 1, p. 011002, Jan. 2018, doi: 10.1103/PhysRevApplied.9.011002.

[81] C.-F. Pai, L. Liu, Y. Li, H. W. Tseng, D. C. Ralph, and R. A. Buhrman, “Spin transfer torque devices utilizing the giant spin Hall effect of tungsten,” *Appl. Phys. Lett.*, vol. 101, no. 12, p. 122404, Sep. 2012, doi: 10.1063/1.4753947.

[82] J. Sinova, S. O. Valenzuela, J. Wunderlich, C. H. Back, and T. Jungwirth, “Spin Hall effects,” *Rev. Mod. Phys.*, vol. 87, no. 4, pp. 1213–1260, Oct. 2015, doi: 10.1103/RevModPhys.87.1213.

[83] K. Xia, P. J. Kelly, G. E. W. Bauer, A. Brataas, and I. Turek, “Spin torques in ferromagnetic/normal-metal structures,” *Phys. Rev. B*, vol. 65, no. 22, p. 220401, May 2002, doi: 10.1103/PhysRevB.65.220401.

[84] K. Carva and I. Turek, “Spin-mixing conductances of thin magnetic films from first principles,” *Phys. Rev. B*, vol. 76, no. 10, p. 104409, Sep. 2007, doi: 10.1103/PhysRevB.76.104409.

[85] M. Zwierzycki, Y. Tserkovnyak, P. J. Kelly, A. Brataas, and G. E. W. Bauer, “First-principles study of magnetization relaxation enhancement and spin transfer in thin magnetic films,” *Phys. Rev. B*, vol. 71, no. 6, p. 064420, Feb. 2005, doi: 10.1103/PhysRevB.71.064420.

[86] S. Fukami, C. Zhang, S. DuttaGupta, A. Kurenkov, and H. Ohno, "Magnetization switching by spin–orbit torque in an antiferromagnet–ferromagnet bilayer system," *Nat. Mater.*, vol. 15, no. 5, pp. 535–541, May 2016, doi: 10.1038/nmat4566.

[87] G. Yu *et al.*, "Switching of perpendicular magnetization by spin–orbit torques in the absence of external magnetic fields," *Nat. Nanotechnol.*, vol. 9, no. 7, pp. 548–554, Jul. 2014, doi: 10.1038/nnano.2014.94.

[88] Y.-C. Lau, D. Betto, K. Rode, J. M. D. Coey, and P. Stamenov, "Spin–orbit torque switching without an external field using interlayer exchange coupling," *Nat. Nanotechnol.*, vol. 11, no. 9, pp. 758–762, Sep. 2016, doi: 10.1038/nnano.2016.84.

[89] M.J. Donahue and D.G. Porter, "OOMMF User's Guide, Version 1.0 Interagency Report NISTIR 6376, National Institute of Standards and Technology, Gaithersburg, MD (Sept 1999)." http://math.nist.gov/oommf/

[90] S. V. Aradhya, G. E. Rowlands, J. Oh, D. C. Ralph, and R. A. Buhrman, "Nanosecond-Timescale Low Energy Switching of In-Plane Magnetic Tunnel Junctions through Dynamic Oersted-Field-Assisted Spin Hall Effect," *Nano Lett.*, vol. 16, no. 10, pp. 5987–5992, Oct. 2016, doi: 10.1021/acs.nanolett.6b01443.

[91] Y.-H. Hsieh *et al.*, "Permanent ferroelectric retention of BiFeO3 mesocrystal," *Nat. Commun.*, vol. 7, no. 1, p. 13199, Dec. 2016, doi: 10.1038/ncomms13199.

[92] N. Sakimura *et al.*, "MRAM Cell Technology for Over 500-MHz SoC," *IEEE J. Solid-State Circuits*, vol. 42, no. 4, pp. 830–838, Apr. 2007, doi: 10.1109/JSSC.2007.891665.

[93] H. Honjo *et al.*, "First demonstration of field-free SOT-MRAM with 0.35 ns write speed and 70 thermal stability under 400°C thermal tolerance by canted SOT structure and its advanced patterning/SOT channel technology," in *2019 IEEE International Electron Devices Meeting (IEDM)*, Dec. 2019, p. 28.5.1-28.5.4. doi: 10.1109/IEDM19573.2019.8993443.

[94] Y.-H. Chu *et al.*, "Electric-field control of local ferromagnetism using a magnetoelectric multiferroic," *Nat. Mater.*, vol. 7, no. 6, pp. 478–482, Jun. 2008, doi: 10.1038/nmat2184.

[95] D. Y. Qiu, K. Ashraf, and S. Salahuddin, "Nature of magnetic domains in an exchange coupled BiFeO3/CoFe heterostructure," *Appl. Phys. Lett.*, vol. 102, no. 11, 2013, doi: 10.1063/1.4795794.

[96] J. J. Wang *et al.*, "Magnetization Reversal by Out-of-plane Voltage in BiFeO3-based Multiferroic Heterostructures," *Sci. Rep.*, vol. 5, no. 1, p. 10459, Sep. 2015, doi: 10.1038/srep10459.

[97] J. J. Wang *et al.*, "Effect of strain on voltage-controlled magnetism in BiFeO3-based heterostructures," *Sci. Rep.*, vol. 4, no. 1, p. 4553, May 2015, doi: 10.1038/srep04553.

[98] M. Trassin *et al.*, “Interfacial coupling in multiferroic/ferromagnet heterostructures,” *Phys. Rev. B*, vol. 87, no. 13, p. 134426, Apr. 2013, doi: 10.1103/PhysRevB.87.134426.

[99] Z. Zhou *et al.*, “Probing electric field control of magnetism using ferromagnetic resonance,” *Nat. Commun.*, vol. 6, no. 1, p. 6082, May 2015, doi: 10.1038/ncomms7082.

[100] S. Dong *et al.*, “Exchange Bias Driven by the Dzyaloshinskii-Moriya Interaction and Ferroelectric Polarization at G -Type Antiferromagnetic Perovskite Interfaces,” *Phys. Rev. Lett.*, vol. 103, no. 12, p. 127201, Sep. 2009, doi: 10.1103/PhysRevLett.103.127201.

[101] J. X. Zhang *et al.*, “Effect of substrate-induced strains on the spontaneous polarization of epitaxial thin films Ferroelectric size effects in multiferroic thin films Phase-field model of domain structures in ferroelectric thin films,” *J. Appl. Phys. Lett.*, vol. 101, no. 78, pp. 114105–51606, 2007, doi: 10.1063/1.2743733.

[102] D. Sando *et al.*, “Crafting the magnonic and spintronic response of BiFeO 3 films by epitaxial strain,” *Nat. Mater.*, vol. 12, p. 641, 2013, doi: 10.1038/NMAT3629.

[103] A. Agbelele *et al.*, “Strain and Magnetic Field Induced Spin-Structure Transitions in Multiferroic BiFeO3,” *Adv. Mater.*, vol. 29, no. 9, pp. 1–8, 2017, doi: 10.1002/adma.201602327.

[104] B. Ruette *et al.*, “Magnetic-field-induced phase transition in BiFeO3 observed by high-field electron spin resonance: Cycloidal to homogeneous spin order,” *Phys. Rev. B - Condens. Matter Mater. Phys.*, vol. 69, no. 6, 2004, doi: 10.1103/PhysRevB.69.064114.

[105] K. M. D. Hals, Y. Tserkovnyak, and A. Brataas, “Phenomenology of current-induced dynamics in antiferromagnets,” *Phys. Rev. Lett.*, vol. 106, no. 10, 2011, doi: 10.1103/PhysRevLett.106.107206.

[106] H. V Gomonay and V. M. Loktev, “Spin transfer and current-induced switching in antiferromagnets,” *Phys. Rev. B*, vol. 81, no. 14, p. 144427, Apr. 2010, doi: 10.1103/PhysRevB.81.144427.

[107] T. Zhao *et al.*, “Electrical control of antiferromagnetic domains in multiferroic BiFeO3 films at room temperature,” *Nat. Mater.*, vol. 5, no. 10, pp. 823–829, 2006, doi: 10.1038/nmat1731.

[108] H. Bé, M. Bibesz, S. Petitx, J. Kreisel{, A. Barthé, and L. Myy, “Structural distortion and magnetism of BiFeO 3 epitaxial thin films: A Raman spectroscopy and neutron diffraction study,” *Philos. Mag. Lett.*, vol. 87, pp. 3–4, doi: 10.1080/09500830701235802.

[109] M. Matsuda *et al.*, "Magnetic dispersion and anisotropy in multiferroic BiFeO 3," *Phys. Rev. Lett.*, vol. 109, no. 6, 2012, doi: 10.1103/PhysRevLett.109.067205.

[110] T. Jungwirth, X. Marti, P. Wadley, and J. Wunderlich, "Antiferromagnetic spintronics," *Nature Nanotechnology*, vol. 11, no. 3. pp. 231–241, 2016. doi: 10.1038/nnano.2016.18.

[111] D. Pantel, Y. H. Chu, L. W. Martin, R. Ramesh, D. Hesse, and M. Alexe, "Switching kinetics in epitaxial BiFeO3thin films," *J. Appl. Phys.*, vol. 107, no. 8, pp. 84111–21303, 2010, doi: 10.1063/1.3392884.

[112] J. Li, B. Nagaraj, H. Liang, W. Cao, C. H. Lee, and R. Ramesh, "Ultrafast polarization switching in thin-film ferroelectrics," *Appl. Phys. Lett.*, vol. 84, no. 7, pp. 1174–1176, 2004, doi: 10.1063/1.1644917.

[113] H. Béa, M. Bibes, S. Petit, J. Kreisel, and A. Barthémév, "Structural distortion and magnetism of BiFeO3 epitaxial thin films: A Raman spectroscopy and neutron diffraction study," *Philos. Mag. Lett.*, vol. 87, no. 3–4, pp. 165–174, 2007, doi: 10.1080/09500830701235802.

[114] S. Manipatruni *et al.*, "Voltage Control of Uni-directional Anisotropy in Ferromagnet-Multiferroic System," 2018, doi: 10.1126/sciadv.aat4229.

[115] S. Bhattacharjee, D. Rahmedov, D. Wang, J. Íñiguez, and L. Bellaiche, "Ultrafast Switching of Electric Polarization," *Phys. Rev. Lett.*, vol. 112, no. 14, p. 147601, Apr. 2014, doi: 10.1103/PhysRevLett.112.147601.

[116] E. Parsonnet *et al.*, "Toward Intrinsic Ferroelectric Switching in Multiferroic BiFeO 3," *Phys. Rev. Lett.*, vol. 125, no. 6, p. 067601, Aug. 2020, doi: 10.1103/PhysRevLett.125.067601.

[117] B. Prasad *et al.*, "Ultralow Voltage Manipulation of Ferromagnetism," *Adv. Mater.*, vol. n/a, no. n/a, p. 2001943, doi: 10.1002/adma.202001943.

[118] S.-C. Chang, A. Naeemi, D. E. Nikonov, and A. Gruverman, "Theoretical Approach to Electroresistance in Ferroelectric Tunnel Junctions," *Phys. Rev. Appl.*, vol. 7, no. 2, p. 024005, Feb. 2017, doi: 10.1103/PhysRevApplied.7.024005.

[119] Y. L. Li, S. Choudhury, Z. K. Liu, and L. Q. Chen, "Effect of external mechanical constraints on the phase diagram of epitaxial PbZr1−xTixO3 thin films—thermodynamic calculations and phase-field simulations," *Appl. Phys. Lett.*, vol. 83, no. 8, pp. 1608–1610, Aug. 2003, doi: 10.1063/1.1600824.

[120] P. Bonhomme *et al.*, "Circuit Simulation of Magnetization Dynamics and Spin Transport," *IEEE Trans. Electron Devices*, vol. 61, no. 5, pp. 1553–1560, May 2014, doi: 10.1109/TED.2014.2305987.

[121] S. Dutta, D. E. Nikonov, S. Manipatruni, I. A. Young, and A. Naeemi, “SPICE Circuit Modeling of PMA Spin Wave Bus Excited Using Magnetoelectric Effect,” *IEEE Trans. Magn.*, vol. 50, no. 9, pp. 1–11, Sep. 2014, doi: 10.1109/TMAG.2014.2320942.

[122] M. Beleggia, M. D. Graef, and Y. T. Millev, “The equivalent ellipsoid of a magnetized body,” *J. Phys. Appl. Phys.*, vol. 39, no. 5, pp. 891–899, Mar. 2006, doi: 10.1088/0022-3727/39/5/001.

[123] C.-Y. Hu and C.-F. Pai, “Benchmarking of Spin–Orbit Torque Switching Efficiency in Pt Alloys,” *Adv. Quantum Technol.*, vol. n/a, no. n/a, p. 2000024, doi: 10.1002/qute.202000024.

[124] Z. Chi, Y.-C. Lau, X. Xu, T. Ohkubo, K. Hono, and M. Hayashi, “The spin Hall effect of Bi-Sb alloys driven by thermally excited Dirac-like electrons,” *ArXiv191012433 Cond-Mat*, Oct. 2019, Accessed: May 02, 2020. [Online]. Available: http://arxiv.org/abs/1910.12433

[125] D. MacNeill, G. M. Stiehl, M. H. D. Guimaraes, R. A. Buhrman, J. Park, and D. C. Ralph, “Control of spin–orbit torques through crystal symmetry in WTe2/ferromagnet bilayers,” *Nat. Phys.*, vol. 13, no. 3, pp. 300–305, Mar. 2017, doi: 10.1038/nphys3933.

[126] L. Zhu, K. Sobotkiewich, X. Ma, X. Li, D. C. Ralph, and R. A. Buhrman, “Strong Damping-Like Spin-Orbit Torque and Tunable Dzyaloshinskii–Moriya Interaction Generated by Low-Resistivity Pd1−xPtx Alloys,” *Adv. Funct. Mater.*, vol. 29, no. 16, p. 1805822, 2019, doi: 10.1002/adfm.201805822.

[127] Q. Shao *et al.*, “Roadmap of Spin–Orbit Torques,” *IEEE Trans. Magn.*, vol. 57, no. 7, pp. 1–39, Jul. 2021, doi: 10.1109/TMAG.2021.3078583.

[128] “COMSOL: Multiphysics Software for Optimizing Designs,” *COMSOL Multiphysics*®. https://www.comsol.com/ (accessed Jul. 10, 2020).

[129] C. Zhang, S. Fukami, H. Sato, F. Matsukura, and H. Ohno, “Spin-orbit torque induced magnetization switching in nano-scale Ta/CoFeB/MgO,” *Appl. Phys. Lett.*, vol. 107, no. 1, p. 012401, Jul. 2015, doi: 10.1063/1.4926371.

[130] X. Liu, D. Mazumdar, W. Shen, B. D. Schrag, and G. Xiao, “Thermal stability of magnetic tunneling junctions with MgO barriers for high temperature spintronics,” *Appl. Phys. Lett.*, vol. 89, no. 2, p. 023504, Jul. 2006, doi: 10.1063/1.2219997.

[131] O. J. Lee *et al.*, “Central role of domain wall depinning for perpendicular magnetization switching driven by spin torque from the spin Hall effect,” *Phys. Rev. B*, vol. 89, no. 2, p. 024418, Jan. 2014, doi: 10.1103/PhysRevB.89.024418.

[132] B. Jinnai *et al.*, "High-Performance Shape-Anisotropy Magnetic Tunnel Junctions down to 2.3 nm," in *2020 IEEE International Electron Devices Meeting (IEDM)*, Dec. 2020, p. 24.6.1-24.6.4. doi: 10.1109/IEDM13553.2020.9371972.

[133] H. Sato *et al.*, "14ns write speed 128Mb density Embedded STT-MRAM with endurance>1010 and 10yrs retention@85°C using novel low damage MTJ integration process," in *2018 IEEE International Electron Devices Meeting (IEDM)*, Dec. 2018, p. 27.2.1-27.2.4. doi: 10.1109/IEDM.2018.8614606.

[134] S. S. P. Parkin, M. Hayashi, and L. Thomas, "Magnetic Domain-Wall Racetrack Memory," *Science*, vol. 320, no. 5873, pp. 190–194, Apr. 2008, doi: 10.1126/science.1145799.

[135] D. A. Allwood, G. Xiong, C. C. Faulkner, D. Atkinson, D. Petit, and R. P. Cowburn, "Magnetic Domain-Wall Logic," vol. 309, p. 6, 2005.

[136] P. Sharma *et al.*, "Nonvolatile ferroelectric domain wall memory," *Sci. Adv.*, vol. 3, no. 6, p. e1700512, Jun. 2017, doi: 10.1126/sciadv.1700512.

[137] G. Catalan, J. Seidel, R. Ramesh, and J. F. Scott, "Domain wall nanoelectronics," *Rev. Mod. Phys.*, vol. 84, no. 1, pp. 119–156, Feb. 2012, doi: 10.1103/RevModPhys.84.119.

[138] A. Q. Jiang and Y. Zhang, "Next-generation ferroelectric domain-wall memories: principle and architecture," *NPG Asia Mater.*, vol. 11, no. 1, p. 2, Dec. 2019, doi: 10.1038/s41427-018-0102-x.

[139] J. P. V. McConville *et al.*, "Ferroelectric Domain Wall Memristor," *Adv. Funct. Mater.*, vol. 30, no. 28, p. 2000109, 2020, doi: 10.1002/adfm.202000109.

[140] P. Wadley *et al.*, "Electrical switching of an antiferromagnet," *Science*, vol. 351, no. 6273, pp. 587–590, Feb. 2016, doi: 10.1126/science.aab1031.

[141] O. Gomonay, T. Jungwirth, and J. Sinova, "High Antiferromagnetic Domain Wall Velocity Induced by Néel Spin-Orbit Torques," *Phys. Rev. Lett.*, vol. 117, no. 1, p. 017202, Jun. 2016, doi: 10.1103/PhysRevLett.117.017202.

[142] X. Chen *et al.*, "Electric field control of Néel spin–orbit torque in an antiferromagnet," *Nat. Mater.*, vol. 18, no. 9, pp. 931–935, Sep. 2019, doi: 10.1038/s41563-019-0424-2.

[143] V. M. T. S. Barthem, C. V. Colin, H. Mayaffre, M.-H. Julien, and D. Givord, "Revealing the properties of Mn2Au for antiferromagnetic spintronics," *Nat. Commun.*, vol. 4, no. 1, p. 2892, Dec. 2013, doi: 10.1038/ncomms3892.

[144] B. G. Park *et al.*, "A spin-valve-like magnetoresistance of an antiferromagnet-based tunnel junction," *Nat. Mater.*, vol. 10, no. 5, pp. 347–351, May 2011, doi: 10.1038/nmat2983.

[145] Y. Ou, S. Shi, D. C. Ralph, and R. A. Buhrman, “Strong spin Hall effect in the antiferromagnet PtMn,” *Phys. Rev. B*, vol. 93, no. 22, p. 220405, Jun. 2016, doi: 10.1103/PhysRevB.93.220405.

[146] V. Tshitoyan *et al.*, “Electrical manipulation of ferromagnetic NiFe by antiferromagnetic IrMn,” *Phys. Rev. B*, vol. 92, no. 21, p. 214406, Dec. 2015, doi: 10.1103/PhysRevB.92.214406.

[147] Y. Wang *et al.*, “Room-Temperature Giant Charge-to-Spin Conversion at the $SrTiO_3$–$LaAlO_3$ Oxide Interface,” *Nano Lett.*, vol. 17, no. 12, pp. 7659–7664, Dec. 2017, doi: 10.1021/acs.nanolett.7b03714.

[148] H. Kontani, T. Tanaka, D. S. Hirashima, K. Yamada, and J. Inoue, “Giant Intrinsic Spin and Orbital Hall Effects in Sr 2 M O 4 (M = Ru , Rh, Mo),” *Phys. Rev. Lett.*, vol. 100, no. 9, p. 096601, Mar. 2008, doi: 10.1103/PhysRevLett.100.096601.

[149] T. Tanaka *et al.*, “Intrinsic spin Hall effect and orbital Hall effect in 4 d and 5 d transition metals,” *Phys. Rev. B*, vol. 77, no. 16, p. 165117, Apr. 2008, doi: 10.1103/PhysRevB.77.165117.

[150] H. Kontani, M. Naito, D. S. Hirashima, K. Yamada, and J. Inoue, “Study of Intrinsic Spin and Orbital Hall Effects in Pt Based on a (6 *s* , 6 *p* , 5 *d*) Tight-Binding Model,” *J. Phys. Soc. Jpn.*, vol. 76, no. 10, p. 103702, Oct. 2007, doi: 10.1143/JPSJ.76.103702.

[151] S. Ding *et al.*, “Harnessing Orbital-to-Spin Conversion of Interfacial Orbital Currents for Efficient Spin-Orbit Torques,” *Phys. Rev. Lett.*, vol. 125, no. 17, p. 177201, Oct. 2020, doi: 10.1103/PhysRevLett.125.177201.

[152] G. Géranton, F. Freimuth, S. Blügel, and Y. Mokrousov, “Spin-orbit torques in L 1 0 − FePt / Pt thin films driven by electrical and thermal currents,” *Phys. Rev. B*, vol. 91, no. 1, p. 014417, Jan. 2015, doi: 10.1103/PhysRevB.91.014417.

[153] J.-M. Kim *et al.*, “Observation of Thermal Spin–Orbit Torque in W/CoFeB/MgO Structures,” *Nano Lett.*, vol. 20, no. 11, pp. 7803–7810, Nov. 2020, doi: 10.1021/acs.nanolett.0c01702.

[154] M. Filianina *et al.*, “Electric-Field Control of Spin-Orbit Torques in Perpendicularly Magnetized W / CoFeB / MgO Films,” *Phys. Rev. Lett.*, vol. 124, no. 21, p. 217701, May 2020, doi: 10.1103/PhysRevLett.124.217701.

[155] A. Sengupta and K. Roy, “Encoding neural and synaptic functionalities in electron spin: A pathway to efficient neuromorphic computing,” *Appl. Phys. Rev.*, vol. 4, no. 4, p. 041105, Dec. 2017, doi: 10.1063/1.5012763.

[156] Z. Cao *et al.*, “Reconfigurable Physical Unclonable Function Based on Spin-Orbit Torque Induced Chiral Domain Wall Motion,” *IEEE Electron Device Lett.*, vol. 42, no. 4, pp. 597–600, Apr. 2021, doi: 10.1109/LED.2021.3057638.

[157] T. P. Xiao *et al.*, “Energy and Performance Benchmarking of a Domain Wall-Magnetic Tunnel Junction Multibit Adder,” *IEEE J. Explor. Solid-State Comput. Devices Circuits*, vol. 5, no. 2, pp. 188–196, Dec. 2019, doi: 10.1109/JXCDC.2019.2955016.